COMPACT STELLAR MERGERS: THE ORIGIN AND ELECTROMAGNETIC COUNTERPARTS OF GRAVITATIONAL WAVES

Joseph John Fernandez

A thesis submitted in partial fulfilment of the requirements of

Liverpool John Moores University

for the degree of

Doctor of Philosophy.

December 2020

Declaration

The work presented in this thesis was carried out at the Astrophysics Research Institute, Liverpool John Moores University. Unless otherwise stated, it is the original work of the author.

While registered as a candidate for the degree of Doctor of Philosophy, for which submission is now made, the author has not been registered as a candidate for any other award. This thesis has not been submitted in whole, or in part, for any other degree.

Joseph John Fernandez
Astrophysics Research Institute
Liverpool John Moores University
IC2, Liverpool Science Park
146 Brownlow Hill
Liverpool
L3 5RF
UK

MAY 4, 2021

Abstract

The detection of gravitational waves (GWs) originating from a black hole (BH) binary merger in 2015 by LIGO marked the beginning of the age of GW astronomy. Another defining moment came in 2017 with the joint detection of GWs and their electromagnetic (EM) counterpart, beginning with a short gamma ray burst (sGRB), from a neutron star merger.

For GW astronomy to reach its scientific potential accurate models of the binary GW inspiral are needed. In addition, an understanding of the possible formation channels of merging compact binaries (including how the formation history is encoded into GW observables) and of the possible EM counterparts to GWs (such as sGRBs, kilonovae and GRB afterglows in the case of NS mergers) is required. This thesis is dedicated to these two aspects of GW astrophysics.

In part I we discuss a new formation channel of compact binaries: tidal encounters with a massive BH at galactic centres or potentially in dense star clusters. First we discuss simple cases where initially circular binaries are injected towards a massive BH. The analysis is later extended to initially eccentric systems (corresponding to different BH binary origins). These tidal encounters can disrupt binaries, but do not always lead their break-up. Since surviving binaries tend to become hard and eccentric, this process can produce BH mergers in principle. For initially circular binaries, we show that the gravitational wave (GW) merger times become shorter by a factor of more than 10^2 (10^5) in 10% (1%) of the surviving cases. This reduction is primarily due to the growth in binary's eccentricity at the tidal encounter. We obtain the effective spin distribution of the survivors. It is found that binary orientations can flip in the opposite direction

at the tidal encounter. For the survivors with large merger time reduction factors, the effective spin distribution is found to be rather flat. The merger rate due to the tidal encounter channel is estimated to be $\sim 0.6\mathrm{Gpc}^{-3}\mathrm{yr}^{-1}$. This estimate is not especially sensitive to whether initially circular or initially eccentric binaries are considered.

In part II we study merger jet radio images. These images recently proved to be essential in breaking the degeneracy between different ejecta models for the afterglow of the neutron star (NS) merger event GW170817. The properties of synthetic radio images are characterized in detail by using semi-analytic models of laterally spreading GRB jets, and compared to the case of collimated jets. The image centroid evolution is obtained, and we find that this feature initially moves away from the explosion point in the sky with apparent superlumianal velocity, following the principal jet. After reaching a maximum displacement its motion is reversed. This behavior is in line with that observed in full hydrodynamics simulations. We then explicitly show images can be used to break intrinsic degeneracies in afterglow light curves, and in particular how they can be used to determine the viewing angle θ_{obs}, or more precisely $\Delta\theta = \theta_{obs} - \theta_c$, where θ_c is the jet core opening-angle. Two methods for determining $\Delta\theta$ are contrasted: the direct comparison of two images and the point emitter approximation for apparent superluminal motion, which states that for the apparent velocity at peak time $\beta_{app} \sim 1/\Delta\theta$. By considering five different jets with identical light curves at their peak time and which roughly agree with GW170817 afterglow radio data ($\nu = 3$ GHz), the viewing angle for this event is estimated to be $\theta_{obs} \sim 0.32$ rad.

Publications

In the course of completing the work presented in this thesis, the following papers have been submitted for publication in a refereed journal or are in preparation:

Fernández J. J. & Kobayashi S., *"Black Hole Mergers Induced by Tidal Encounters with a Galactic Centre Black Hole"*, 2019, Monthly Notices of the Royal Astronomical Society, 487, 12001209

Fernández J. J., Kobayashi S. & Lamb, G. P., *"Determining the viewing angle of neutron star merger jets with VLBI radio images"*, arXiv:2101.05138, 2021 (submitted to Monthly Notices of the Royal Astronomical Society)

JOSEPH JOHN FERNANDEZ MAY 4, 2021

Acknowledgements

I would like to thank my supervisor Shiho Kobayashi for the knowledge he has shared with me, his patience and his guidance. You have helped me grow as a scientist and a person. I will always be grateful for the time you have invested in me. I would like to acknowledge Chris Copperwheat and Iain Steele for their useful comments on this thesis. I would also like to thank Gavin Lamb for his friendship and scientific guidance. I would like extend special thanks to my mentors and supervisors at ULL, Daniel Alonso and Antonia Ruiz, and to Aida, the best maths teacher a young student could ask for.

I would not be at this stage without generous financial support from the Spanish government to pursue undergraduate and master's studies. I am also extremely grateful for the LJMU scholarship which funded my PhD studies.

I have met fantastic people during my time at the ARI. Thank you Danny Horta for being like a brother. Many thanks to my co-students and friends Joaquin, Meghan, Mike, Tom, Charlotte, Alex, Rob, Trisha, Alberto, Sarah, Bethan, Connor, Allister, Alberto, Sam, Shaun, Simon, Andrew, Adrian, Kyle, Fiona and Kirsty, to name a few, for the many tea breaks, meals, beers and rather random conversations over the past few years. I truly enjoyed our time together. I would like to extend special thanks to Maisie, Danielle and Kate for being lovely friends and an amazing support group. I already miss you all very much.

I will always have happy memories of lunch at the ARI. Thank you Chris, Phil, Sue, Ivan and Ricardo for always having a funny story to tell. I would like to extend a special thank you to Marie for being someone students can reach out to, for being

extremely caring and, on a personal note, for having me as a demonstrator for two years in the labs. As grumpy as it made me at times I really enjoyed working with the students, and I learned a lot while working with you. I would like to thank the post-doc community at the ARI for their support, most of all Helen and Claire, who helped me a lot during my first year. Many thanks to Anna, Danielle, Maureen and Caroline for their help with admin, as well as Dan and Ben for helping me reset my password so many times!

There is no way I would have made it this far without my extended family and friends. I am extremely grateful to my Auntie Mo and Uncle Eamonn for being like parents,taking me into their home and offering me counsel; Auntie Una for her guidance and many chats over the years; Sue, Clare and Rich for being like older siblings to me and always making me feel special; my cousins Alice, Oliver, Leon, Sean, James and Maisie who I love with a passion, and Auntie Moira and Uncle Paul for being like grandparents and always making me feel welcome with them. I will always be grateful to my friends at home for the good times, the laughs and the support. Thank you Danny, Aitor, Raquel, Elpidio, Rubén, Yusra, Javi, Paula, Amanda and Moisés for our years of friendship, I have enjoyed growing up with you all and can't imagine things without you. Also thanks to Laura and Majda. Thank you Jesús for your constant support, and Yaiza, Alba, Esteban, Jaime and Marina for the good times we have spent together over the past few years. Even though we don't see each other enough I will always be grateful to count Ruyman, Natalia, Manolo, Ángel and Martín among my friends.

I would like to take this opportunity to thank my best friend Alicia for always being there for me and for helping me be better than I would otherwise be. I would like to express my deepest thanks and love to Mum, Dad, Carla and Tito Chico for the good and the hard times we have had together, for loving me and always having my back; and to Lily and Buddy for teaching me things that humans simply cannot.

This thesis is dedicated to my grandparents. To my Grandad John, who I never had the chance to meet but feel like I have known all my life, and to his brother, my dear Uncle Peter who has cared for Carla and me like grandchildren of his own. To my Abuelo Pepe who would have been so proud to see me finish this PhD, and who I will forever

love and miss. And last but not least my Nanny Pat and Abuela María, who I love so much and am so happy to have. Thank you for always taking care of me.

"You dig deeper and it gets more and more complicated and you get confused and its tricky, its hard right. Its hard. But its beautiful."

- Brian Cox CBE FRS

Contents

List of Tables

List of Figures

Chapter 1

Introduction

1.1 Gravitational waves and multi-messenger astronomy

For centuries astronomy relied solely on electromagnetic (EM) waves to study the cosmos. Advances in detector technology expanded the range of EM frequencies which could be observed. This in turn led to more insight into the physics of the Universe. The wider the range of observable frequencies, the more complete the picture which can be obtained of the emitters. For instance, to determine the composition of a star in detail requires spectra which may cover multiple observational wavebands. In addition, photons of different energies can often be associated with different processes or properties of the emitting systems. For example, high frequency photons such as gamma rays can be associated with energetic events involving shocks (such as gamma ray bursts, e.g. Kumar & Zhang 2015), whereas the emission of protostars peaks in the infrared (e.g. Adams & Shu 1985; Dunham et al. 2014).

Multimessenger astronomy, the study of the Universe by combining EM observations with other sources of information or messengers, aims to expand the observational capacity of traditional astronomy. These new messengers include neutrinos, cosmic rays or gravitational waves (GWs) (Branchesi, 2016). GW astronomy has been especially relevant since the start of LIGO's operating runs in 2015 (Abbott et al., 2016). GWs

are important as they open up the possibility of observing the dark Universe. This includes parts of the Universe where light cannot be emitted (such as in black hole mergers, the detection of which has become routine) or times when it simply cannot propagate (such as in the early Universe, before the cosmic microwave background was emitted) (Colpi & Sesana, 2017).

The merger of compact binaries (whose components are stellar remnants such as white dwarves, neutron stars or black holes) are a prime source for current GW detectors (see e.g. Abbott et al. 2020b). Much like the rest of astrophysics, GW astronomy relies heavily on theoretical models to interpret observations. Interpreting binary mergers requires modelling the GW signal due to the inspiral. To extract as much scientific value as possible is is also necessary to model the pre-merger life of these binaries, before the inspiral phase, and the post-merger evolution of the remnant. The former involves considering what processes can lead to the formation and merger of compact binaries, what rate of mergers each process can produce or how the properties of the GW signals (such as their amplitude and frequency spectrum) depend on their physical state of the binary. The latter depends on the composition of the binary. If it was made up solely of black holes, the ring-down signal of the merger remnant could be used to test predictions of alternative theories of gravity. If at least one of the binary members was a neutron star an electromagnetic counterparts can be expected (depending on the binary mass ratio), which could provide information on the host galaxy of the merger, the properties of the surrounding matter or, for example, provide insight into shock and accretion physics. Multimessenger observations, which combine EM and GW signal, have already been used to place independent constraints on the Hubble constant H_0, related to the rate of expansion of the Universe (Hotokezaka et al., 2019).

1.2 Outline of the thesis

As introduced above, modelling binary inspirals is extremely important to be able to determine the source of GW signals, but so too is understanding the pre- and post-merger physics. The objective of this thesis is to contribute to the understanding of pre-merger

and post-merger physics. Because these two areas of study involve different physical models and methods, this thesis is divided into two parts.

Part I is dedicated to characterizing a specific dynamical process, the tidal encounter channel, which can result in compact stellar binary mergers. While the focus is placed on black hole mergers, the analysis presented in part I is applicable to compact binaries of any flavour. Chapter 2 gives an introduction to GW science, including the detection of GWs and a discussion of the different formation channels for merging binaries. Chapter 3 details the dynamical formalism used to characterize the tidal encounter channel. The process is then analyzed in detail for binaries that are initially circular in chapter 4. The study is extended to binaries that are initially eccentric in chapter 5. Physical quantities which can be inferred from GW observations are characterized, and an estimate of the merger rate density due to this channel is provided.

Part II sees the focus shifted onto the post-merger stage, and in particular to modelling one of the EM counterparts of neutron star mergers, where the standard gamma-ray burst (GRB) model can be applicable. In chapter 6 the different components of the EM counterpart to neutron star mergers such as GW170817 are introduced: short GRBs, kilonova and the merger jet afterglow. The semi-analytic formalism to model jet dynamics and radiation is introduced in chapter 7. In chapter 8 a systematic analysis of synthetic radio images of merger jets is presented. A novel contribution of this section is the calculation of images of laterally spreading jets by means of semi-analytic methods (these images are generally obtained using full hydrodynamical simulations). Different observable quantities which can be extracted from images (such as the image centroid and different aspects of the image structure) are characterized. The results are then used to described how radio imaging can be used to break intrinsic degeneracies in lightcurve parameter estimation, and in particular determine the viewing angle between the jet axis and the observer's line-of-sight.

General conclusions and suggestions for future work are given in chapter 9.

Part I

A dynamical source of merging black holes in the galactic centre

Chapter 2

Gravitational Waves

The LIGO (Laser Interferometer Gravitational wave Observatory) facilities made the first direct detection of GWs in 2015 (Abbott et al., 2016a). Their existence was first predicted by Albert Einstein almost a century earlier (Einstein, 1916). By considering a small perturbation to an otherwise flat spacetime metric, it can be shown that changes in the gravitational field propagate obeying a well understood wave equation. The result can also be generalized to curved spacetimes (Misner et al., 1973).

It can also be shown that the lowest-order source of GWs is the time-varying mass-quadrupole (Flanagan & Hughes, 2005). This result implies that the Universe is full of GW sources: most compact objects in the Universe are part of binary or higher order systems. Not surprisingly, to date all of the direct observations of GWs have originated from binary systems (Abbott et al., 2020b).

This chapter serves as motivation and background for the work to follow in part I. The foundations of General Relativity are briefly reviewed. A sketch of the derivation of the GW equation is given, as well as a discussion of GW physics, sources and detection. In the last section the most relevant theoretical models for the origin of BH binary systems are examined.

2.1 General relativity and gravitational waves

Isaac Newton's law of universal gravitation, first presented in 1686, states that two masses $m_1,\ m_2$ will attract each other with a force proportional to their masses and inversely proportional to the square of the distance between them,

$$\mathbf{F}_{1,2} = \frac{Gm_1(\mathbf{r}_1)m_2(\mathbf{r}_2)}{|\mathbf{r}_2 - \mathbf{r}_1|^2}\hat{r}_{1,2} = -\mathbf{F}_{2,1} \tag{2.1}$$

where the subscript $(1, 2)$ indicates that force is that which mass 1 feels due to mass 2, and $\hat{r}_{1,2}$ is the unit vector directed along the line joining the two masses, oriented from m_1 to m_2 (Landau & Lifshitz, 1980). With this law the motion of celestial bodies and of freely-falling objects on the Earth were given a unified explanation under a single theory. Newton's law prevailed as an adequate description of gravity for over 200 years, but by the end of the nineteenth century observational and theoretical evidence indicated that it was an incomplete description. In particular, the theory is explicitly non-local: as described by equation 2.1, changes in m_1 will be immediately felt by m_2, as the mass contributions to the force depend only on the instantaneous position of each particle (Misner et al. 1973; Landau & Lifshitz 1980).

The non-locality of Newtonian gravity makes it incompatible with special relativity (SR). This theory describes motion in inertial reference frames and is built upon two postulates: that physical laws are invariant under changes of inertial frame, and that the speed of light in vacuum is the same for all inertial observers. Among the consequences of these are that space and time are unified into a single physical object known as space-time, and that physical information cannot propagate faster than the speed of light in vacuum (Misner et al., 1973). This meant that a new description of gravity was needed, built to be compatible with SR so that the non-local features described above were removed, but that would also reduce to Newton's law in the appropriate limit.

The key to solving this problem was found to lie in a centuries-old experimental result. To a great degree of accuracy, the *inertial mass* (a measure of the opposition of a body to change its state of motion) and *gravitational mass* (a measure of how much a particle

is affected by a gravitational field) are equal. This leads to the universality of free-fall, also known as the *weak equivalence principle*, or the *WEP* (Haugan & Lämmerzahl, 2001):

"All bodies, independently of mass or composition, accelerate equally under the influence of a gravitational field."

In particular, this result implies that a free-falling observer would not be able to distinguish between being immersed in a constant gravitational field or in a uniformly accelerated reference frame: the dynamics of both situations would be identical (at least locally). While constant gravitational fields do not exist in the Universe, in many situations, such as in the immediate vicinity of the surface of a planet, this treatment is a good approximation. Having recognized this, the WEP can be extended to the *Einstein equivalence principle*, or *EEP* (Haugan & Lämmerzahl, 2001),

"The laws of physics in free-fall are locally equivalent to those in the absence of gravity."

As the motion of a free-falling body is locally equivalent to uniformly accelerated motion, and acceleration can be removed with an appropriate change of reference frame, then motion in a gravitational field is locally (that is, for a small enough region of spacetime) equivalent to inertial motion. Therefore, gravity can be described by a coordinate transformation. Additionally, special relativity itself and any laws compatible with it will remain valid in the presence of a gravity (Haugan & Lämmerzahl, 2001).

In SR, the fundamental object is the interval, defined as the quadratic form (Landau & Lifshitz, 1980)

$$ds^2 = \eta_{\alpha\beta} dx^\alpha dx^\beta;\ \eta = diag(-c, 1, 1, 1), \tag{2.2}$$

where the Einstein summation convention for repeated indices is used (Misner et al., 1973), $\alpha,\ \beta = 0 - 3$ and η is the Minkowski metric tensor, a 4×4 symmetric tensor (Landau & Lifshitz, 1980). The interval is an invariant, i.e. it remains constant under

transformations between inertial frames (Lorentz boosts and rotations). As the laws of Special Relativity are still valid in the presence of gravity, and gravity is equivalent to a coordinate transformation, then equation 2.2 holds by simply changing the Minkowski metric for a general metric tensor $\eta \rightarrow g$. Therefore, the gravitational field can be understood as a change in the geometry (or the curvature) of spacetime, embodied in the metric tensor (Misner et al. 1973; Flanagan & Hughes 2005),

$$\mathbf{F}_g \rightarrow g_{\alpha\beta};\ ds^2 = g_{\alpha\beta}dx^\alpha dx^\beta \tag{2.3}$$

This is how gravity is understood in the General Theory of Relativity (GR): the presence of mass changes the geometry of spacetime. In that sense, gravity is interpreted as a fictitious force which bodies feel as they free-fall in curved spacetime. Asymptotically far away from masses, spacetime is flat, i.e. the Minkowski metric of SR determines the geometry (Misner et al., 1973; Landau & Lifshitz, 1980).

In the Newtonian picture, a mass distribution $\rho(\mathbf{r})$ is related to the gravitational field, or equivalently the gravitational potential $\phi(\mathbf{r})$ by Poisson's equation,

$$\nabla^2\phi = 4\pi G\rho(\mathbf{r}). \tag{2.4}$$

Without entering into detail, it can be stated that in GR the corresponding description is given by Einstein's field equations (Le Tiec & Novak, 2017),

$$G_{\mu\nu} + \Lambda g_{\mu\nu} = \frac{8\pi G}{c^4}T_{\mu\nu} \tag{2.5}$$

where $G_{\mu\nu}$ is the Einstein tensor, a combination of the Ricci curvature tensor $R_{\mu\nu}$[1] and its contraction, Λ the cosmological constant, which accounts for the accelerated expansion of the Universe and $T_{\mu\nu}$ is the energy-momentum tensor, which gives the distribution of mass-energy and takes on the role of $\rho(\mathbf{r})$. The Einstein equations are a set of 10 non-linear, partial differential equations which account for the interaction of mass-energy with spacetime: mass distributions determine the geometry of spacetime,

[1]The Ricci tensor is obtained by contracting the curvature tensor $R_{\alpha\beta\gamma\sigma}$, and this tensor from the second derivatives of the metric tensor $g_{\alpha\beta}$.

which itself determines the motion of massive bodies.

2.2 The weak field limit

The non-linearity of the equations means that they are extremely difficult to solve. However, several exact solutions have been found since their formulation. These include the Schwarzschild metric (which describes the spacetime around a spherically symmetric object) or the Kerr metric (for the spacetime of a rotating black hole) (Misner et al., 1973), among others. Interestingly, the equations can be linearized, not unlike the equations of fluid dynamics. While a full derivation is beyond the scope of this work it can be shown that in a flat, background spacetime, for a small metric perturbation $h_{\alpha,\beta}$ such that to first order[2]

$$\eta_{\alpha\beta} \rightarrow g_{\alpha\beta} = \eta_{\alpha\beta} + h_{\alpha\beta}, \;\; |h_{\alpha\beta}| \ll |\eta_{\alpha\beta}|. \tag{2.6}$$

Selecting appropriate coordinates (by setting what is known as the Lorentz gauge), the Einstein equations 2.5 reduce to

$$\Box \bar{h}_{\alpha\beta} = -16\pi T_{\alpha\beta}, \tag{2.7}$$

where $\bar{h}_{\alpha\beta} = h_{\alpha\beta} - h$ is the trace reversed metric perturbation, h the trace of $h_{\alpha\beta}$, and $\Box$ is the D'Alembert operator, defined as

$$\Box = -\frac{1}{c^2}\frac{\partial^2}{\partial t^2} + \nabla^2 \tag{2.8}$$

(Flanagan & Hughes, 2005; Le Tiec & Novak, 2017). This result is an explicit expression of the locality of gravitation in General Relativity. Changes in mass distributions or the field itself do not propagate instantaneously, as they would in the Newtonian theory. Instead, perturbations to the metric, or equivalently the curvature of spacetime, will propagate through space at a finite speed, the speed of light in vacuum c, and obeying

[2] As only first order terms are kept, this approach is also known as *linearized gravity*.

a wave equation. In the absence of mass-energy, equation 2.7 reduces to

$$\Box \bar{h}_{\alpha\beta} = 0, \tag{2.9}$$

which as in electromagnetism or fluid dynamics admits solutions in the form of a superposition of plane waves, $\bar{h}^{\mathbf{k}}_{\alpha\beta} \propto e^{ik_\alpha x^\alpha}$. Once again, without entering into detail it can be shown with this solution that GW waves are transverse (they propagate in the perpendicular direction to the metric oscillations), have two polarization degrees of freedom (often denoted $h_\times$ and h_+) and that only the spatial components of $\bar{h}_{\alpha\beta}$ correspond to radiative degrees of freedom.

The previous discussion is valid in the non-relativistic limit, i.e. for systems with negligible self gravity and flat spacetime backgrounds. While the linearized treatment is not valid in all cases, other formalisms exist to treat these systems, and it can be shown that GWs are a general feature of GR (Blanchet, 2014).

2.3 Sources of gravitational waves

In the non-relativistic, low velocity limit, the sources of GWs are time-varying mass distributions. Therefore, to identify the lowest order sources of GWs it is convenient to analyze the moments of an isolated mass distribution $\rho(\mathbf{r})$:

- The zeroth-order moment is the total mass $M = \int \rho(\mathbf{r}) d^3\mathbf{r}$. Due to conservation of mass, $\dot{M} = 0$. This excludes the possibility of monopolar GW radiation, similarly to how conservation of charge forbids monopolar electromagnetic (EM) radiation.

- The mass dipole is defined as $\mathbf{d}_M = \int \rho(\mathbf{r}) \mathbf{r} d^3\mathbf{r}$. The time derivative of this moment is simply the total linear momentum of the system, $\mathbf{p} = \dot{\mathbf{d}}_m$. As the total linear momentum of an isolated system is conserved, a frame where $\mathbf{p} = \dot{\mathbf{d}}_m = 0$ can always be found. Therefore, dipolar GW radiation is not a true physical effect, but a result of reference frame selection. While the lowest-order

EM waves originate from time-varying charge dipoles, to generate GW radiation higher-order moments must be considered.

- The second moment of the mass distribution is the moment of inertia, or inertia tensor, a 3×3 tensor with components $I_{ij} = \int \rho(\mathbf{r}) x_i x_j d^3\mathbf{r}$, where i, j represent strictly spatial components. There is no conservation law which forces this quantity to be constant. In particular it can be shown that the second time derivative of the quadrupole moment $\mathcal{I}_{ij}$, derived from the inertia tensor as $\mathcal{I}_{ij} = I_{ij} - \frac{1}{3}\delta_{ij}\mathcal{I}_{ij}$, is the lowest-order source of gravitational waves.

Dimensional analysis shows that the quadrupole moment and gravitational perturbation are related by (Flanagan & Hughes, 2005)

$$h \sim \frac{G}{c^4 r} \frac{d^2\mathcal{I}}{dt^2}, \tag{2.10}$$

where r is the distance from the source. A more rigorous analysis of the solutions of equation 2.7 leads to the Einstein quadrupole formula (Misner et al., 1973), which agrees with the previous equation up to factors of order unity (it must also be noted that the previous formula is missing a time-delay dependence in $\mathcal{I}$, assuming the GWs propagate along the z-direction the full formula contains a term $\mathcal{I}(t - z/c)$).

Objects which present time-varying mass-quadrupoles include more or less exotic systems such as core-collapse supernovae in stars with rotating cores, or rotating neutron stars with a small oblateness (Flanagan & Hughes, 2005; Colpi & Sesana, 2017). However, by far the simplest and most common source is the compact binary. Around half of the stars in the Universe are members of binary (or higher-order degeneracy) systems. While only the most compact binaries are visible to currently available GW detectors (BH-BH, BH-NS and NS-NS systems), these are common enough to constitute prime sources for GW physics and astronomy (Flanagan & Hughes, 2005; Le Tiec & Novak, 2017; Colpi & Sesana, 2017).

The essential aspects of the evolution of a compact binary due to GW radiation were described in Peters & Mathews (1963) and Peters (1964). By considering a binary

made of up two point masses, and the loss of energy and angular momentum due to GW emission, it was shown that the eccentricity and semi-major axis of a binary evolve according to

$$\begin{aligned} \dot{e} &= -\frac{19}{12}\frac{\beta e}{a^4(1-e^2)^{5/2}}\left(1+\frac{121}{304}e^2\right), \\ \dot{a} &= -\frac{\beta}{a^3(1-e^2)^{7/2}}\left(1+\frac{73}{24}e^2+\frac{37}{96}e^4\right), \end{aligned} \tag{2.11}$$

where the constant β is a function of the binary member masses, $\beta = 64G^3 m_1 m_2 m/5c^5$. These are known as Peter's equations. From visual inspection it can be seen that the effect of GW radiation is to shrink the binary, and circularize it if it were initially eccentric. The binary members will inspiral towards each other until they coalesce, leaving a single object in their place. The evolution in the $a-e$ plane of an example binary with varying initial eccentricity is shown in figure 2.1 (note that the figure shows the evolution of the adimensional variable $\tilde{a} = a/a_0$; equations 2.11 can be analytically scaled to dimensionless variables). From these equations it can be shown that the GW merger time, or the time in which $a \to 0$, given an initial semi-major axis a_0 and eccentricity e_0 is

$$\tau_{gw}(a_0, e_0) = \frac{12}{19}\frac{c_0^4}{\beta}\int_0^{e_0} de \frac{e^{29/19}(1+121/304\, e^2)^{1181/2299}}{(1-e^2)^{3/2}}, \tag{2.12}$$

where $c_0 = c_0(a_0, e_0)$ is an integration constant (Peters, 1964). The merger times for a binary with members $m_1 = m_2 = 30M_\odot$ and different (a_0, e_0) values are shown in figure 2.2. It can be seen that even for very massive objects τ_{gw} can be orders of magnitude longer than the age of the Universe. The coalescence time can be decreased by reducing the binary semi-major axis or by increasing the eccentricity. For circular binaries ($e_0 = 0$), the expressions take on a simpler form. The semi-major axis decay is given by $a(t) = (a_0^4 - 4\beta t)^{1/4}$. and the coalescence time becomes $\tau_{gw} = a_0^4/4\beta$.

The GW spectrum of a inspiraling binary depends on whether the orbit is circular or eccentric. In the first case, the system will radiate GW waves at twice its Keplerian orbital frequency (Flanagan & Hughes, 2005). As the orbit becomes tighter, the GW

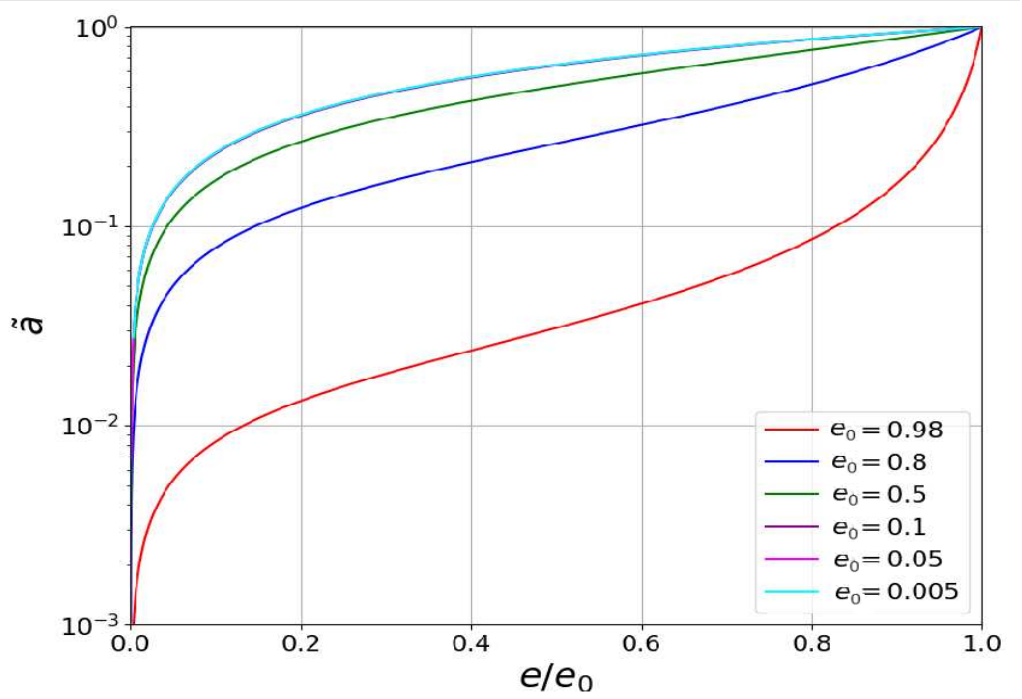

Figure 2.1: The evolution of binaries with various e_0 in the $a/a_0 - e/e_0$ plane (in the figure $\tilde{a} = a/a_0$).

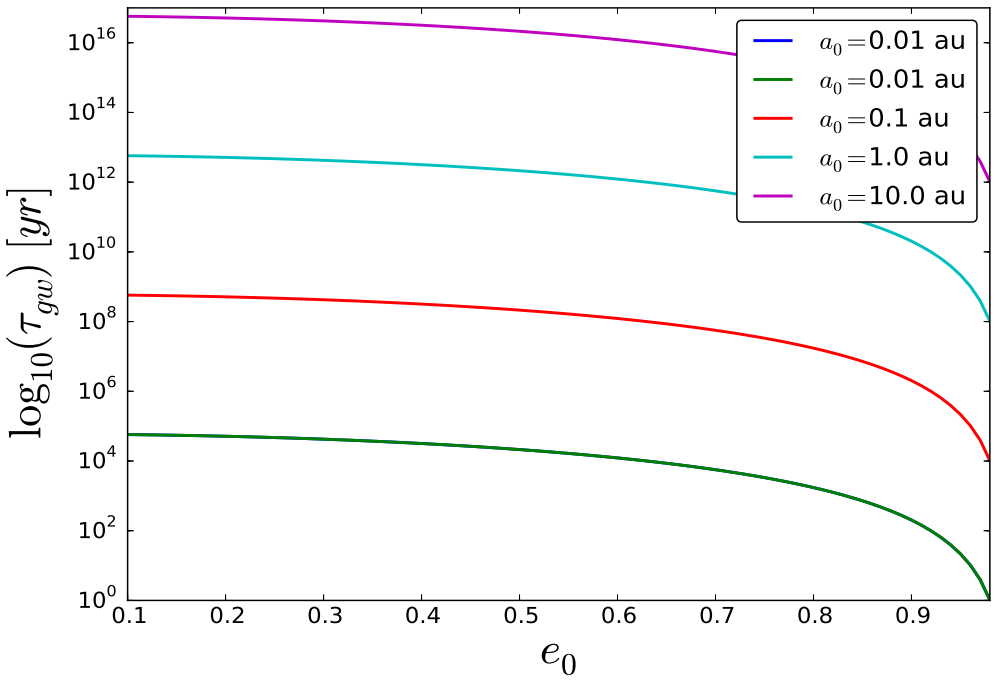

Figure 2.2: Gravitational wave merger times τ_{gw} as a function of eccentricity e, for different initial semi-major axis a_0 values.

frequency will increase, allowing energy and angular momentum to be radiated away at a faster rate, which increases the amplitude of the GWs and accelerates the inspiral. In the case of BHs, this process continues until the innermost-stable circular orbit (ISCO) radius of one of the members is crossed. At this point the GW waves are radiated at the maximum frequency and the BHs plunge into each other, coalescing into a single object. The resulting black hole then emits low-amplitude GWs as it relaxes to its new steady state, in a process known as the ringdown.

Eccentric binaries have a phase-dependent angular velocity and member separation. Therefore, their inspirals are more complicated, radiating GWs over a range of frequencies and amplitudes. In particular, at each periapsis passage the binary emits a burst of large amplitude, high frequency GWs due to the large relative velocity and proximity of its members. In contrast, at apoapsis the radiation is at its weakest. As described by Peter's equations, the eccentricity is quickly radiated away and the inspiral becomes quasi-circular.

2.4 Detection of gravitational waves

Consider two test particles separated by a proper distance L_0 along the x-direction and located at $z = 0$ in a given coordinate frame, and incoming GW radiation which propagates along the z-direction. It can be shown that when the GWs traverse the region of space where the particles are located, the proper distance between them is modified so that (Le Tiec & Novak, 2017)

$$L = L_0 \rightarrow L = L_0 \left[1 + \frac{1}{2} h_{xx}(t, z = 0)\right] \tag{2.13}$$

from where it follows that

$$\frac{\Delta L}{L_0} = \frac{1}{2} h_{xx}(t, z = 0), \tag{2.14}$$

where $\Delta L = L - L_0$. For a pure plane wave solution, the distance between the particles oscillates during the passage of the GW.

This result is key for observational GW physics. While indirect observations of GWs have been available for several decades (GW emission is responsible for the slow inspiral of the Hulse-Taylor binary, e.g. Weisberg et al. 1981; Taylor & Weisberg 1982), direct detection of GWs has become possible in recent years due to the use of GW laser interferometers. These devices use two or more lasers to generate interference patterns. When a GW crosses the path of the lasers, the length of the paths followed by the photons changes. This translates to a modification of the phase of the photons and hence the interference pattern, from which the GW signal can be inferred (Abbott et al., 2009).

A favored design for ground-based interferometers uses a L-configuration, as illustrated in figure 2.3. These devices consist of two laser arms which intersect, forming a 90° angle. Coherent light from a common source is sent down both arms by using a beamsplitter. The light then travels up-arm, At the end of the path, the light is reflected by a mirror, which re-directs the beams down their arms. The reflected beams are then recombined to form the required interference pattern. The detection of GWs is troublesome: they are extremely weak. This can be understood by inspecting equation 2.10: the G/c^4 factor significantly reduces the amplitude of GWs, making it extremely small even for the most massive sources. This effect is counteracted in detectors by using extremely long laser arms. From equation 2.14 it can be read that given a fixed GW amplitude h, the change in the length of the arm ΔL scales with its unperturbed length L_0. Because the phase contribution to the laser phase due to the GW is such that $\Delta\psi \propto \Delta L$, using a longer arm length will lead to a greater modification of the interference pattern.

The currently available network of ground-based GW interferometers consists mainly of L-shaped detectors, including:

- LIGO Hanford and LIGO Livingston, each consisting of two 4 km arms each, and separated by a distance of over 3000 km from each other (Abbott et al.,

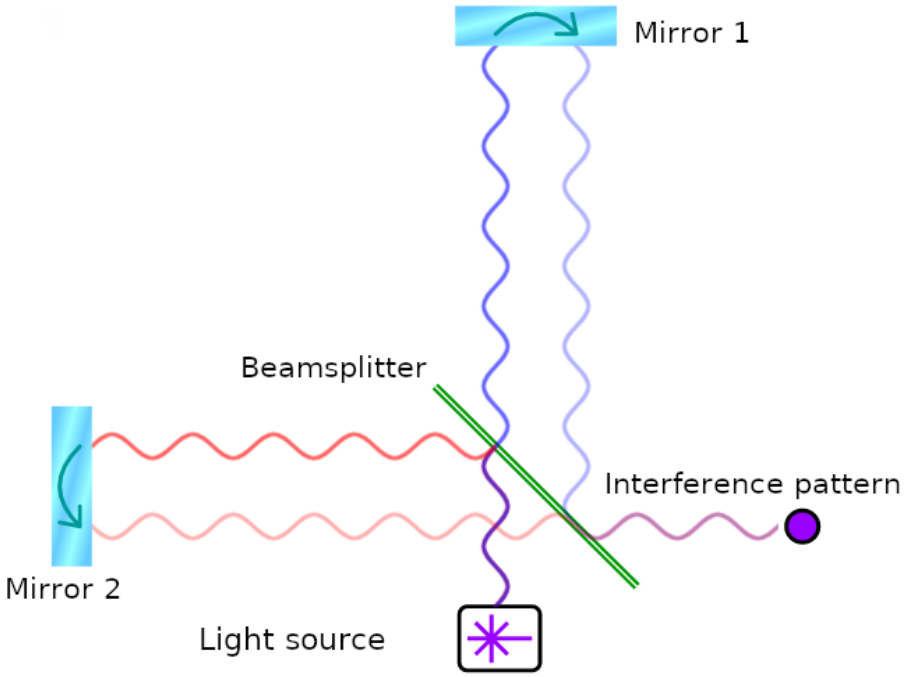

Figure 2.3: Diagram of an L-shaped GW interferometer. A laser source (bottom box) emits a beam which is split by the beamsplitter (green diagonal lines). The beams travel along their respective arms and are reflected off the mirrors. The beams travel back and then recombine. Finally an interference pattern is formed (purple circle). Figure adapted from `https://commons.wikimedia.org/wiki/File:Gravitational_wave_observatory_principle.svg`, supplied under CC BY-SA 3.0 license.

2009).

- The VIRGO interferometer, with 3 km arms, located in Circana, Italy (e.g Riles 2013).
- GEO, with 600 m arms and located in Sarstedt, Germany (Blair et al., 2012).
- Kagra, equipped with with 3 km arms and located in the Kamioka Observatory, Japan (Aso et al., 2013; Abbott et al., 2020).

These facilities will be complimented in coming years with LIGO India (with 4 km arms, and expected completion date around 2025, Unnikrishnan 2013) and the Einstein Telescope (this device is of a different design, made up of three arms in a triangular configuration, Hild et al. 2008), among others.

Ground-based detectors are well suited for the detection of stellar-mass binary inspiral

events. To observe lower frequency events, such as those associated with massive black hole mergers due to galactic interactions or extreme mass-ratio inspirals (eMRIs), much larger detectors are needed. Space based interferometers are expected to be able to probe these low-frequency regions. Proposed instruments include LISA (designed with three 10^6 km laser arms) or DECIGO (designed to have three 1000 km arms).

The first LIGO detection, denoted GW150914, occurred during an engineering run. This event was especially significant, as it constituted the first direct observation of GWs (Abbott et al., 2016a). Additionally, it was also the first direct confirmation of the existence of BH binaries, as well as of BHs of several tens of solar masses (the inferred binary member masses from the GW observation were $35.4^{+5.0}_{-3.4}\ M_\odot$ and $29^{+3.3}_{-4.3}\ M_\odot$, and the merger remnant was estimated to be of $62^{+3.7}_{-3.4}\ M_\odot$, Abbott et al. 2016a). Before GW astronomy there was no observational evidence supporting the existence of BHs of several tens of solar masses. GW detections also allowed for direct confirmation of the existence of Kerr black holes which posses non-zero angular momentum. The effective spin parameter (this parameter is discussed in following sections) of GW151226 is larger than zero. This implies that at least of the binary members had non-zero spin with a component perpendicular to the binary orbital plane (Abbott et al., 2016b).

As of December 2019, the joint LIGO/VIRGO observation efforts have detected 56 compact mergers, 3 NS-NS mergers, 1 BH-NS merger and 3 BH-mass gap objects (mass gap objects cannot be strictly classified as BHs or NSs) (Abbott et al., 2020b; Georgescu, 2020). The merger rate density of BH mergers to be constrained to $23.9^{+14.9}_{-8.6}$ Gpc^{-3}yr^{-1} and the NS merger rate to 320^{+490}_{-240} Gpc^{-3}yr^{-1} (Abbott et al., 2020b).

2.5 The origin of merging compact binaries

The currently available set of BH merger detections are sufficient for it to be stated that these events are commonplace in the Universe. The binary member masses inferred from GW150914, GW170104 and GW170814 were also surprising, as stellar evolution models find difficulty in producing such massive BHs (Abbott et al., 2016a, 2017a,b).

Even when massive enough stars can be formed, the binaries need to be tight or eccentric enough to be able to merge on a time scale which makes observations possible. Additionally, the effective spin parameters inferred from the observations are small, and compatible with zero in all but three of the events.

Much effort has been allocated to describing physical processes which can lead to BH binaries compatible with the LIGO/VIRGO observations. Once a plausible physical mechanism for the formation of these systems is found, its predictions for binary properties which can be inferred from GW observations must be characterized. These include the binary member masses, the chirp mass $\mathcal{M}$ (related to how the frequency increases during the inspiral), orbital eccentricity e, or the effective spin $\chi_{\rm eff}$. The last of these is particularly interesting, as it is very well characterized by LIGO/VIRGO, and is almost constant during the inspiral (Blanchet, 2014). Therefore, it is an excellent tracer of the binary origin. This parameter is the mass-weighed projection of the BH spins onto the binary angular momentum, i.e. a measure of if the black holes are spinning and how large the components are in the direction perpendicular to the orbital plane. Its values range between $\chi_{\rm eff} = 1$ (for perfectly aligned BH spins with the binary angular momentum and maximally spinning BHs) to $\chi_{\rm eff} = -1$ (if the spins are directed in the opposite direction to the angular momentum again with maximally spinning BHS).

A variety of mechanisms have been devised both to form BHs of masses compatible with LIGO/VIRGO observations and to lead them to merge within the age of the Universe. These can generally be split into two broad groups: isolated field binary scenarios, and dynamical formation channels. It is expected, that with aLIGO/VIRGO at design sensitivity, the next observing runs with yield tens to hundreds of detections, which will be sufficient to disentangle the main channels responsible for forming the merging BHs (Farr et al., 2017; Hotokezaka & Piran, 2017; Hotokezaka & Piran, 2017a,b; Farr et al., 2018; Barrett et al., 2018; Gerosa, 2018).

Isolated field binary channels are studied using stellar evolution models to determine what characteristics of massive stellar binaries can eventually lead to merging BHs which are detectable by LIGO/VIRGO. As their name indicates, these models consider

binaries which evolve with little or no interaction with other systems. Therefore the inner-dynamics of the binary must account both for the BH formation and the necessary binary hardening for efficient GW merging. Leading models in this group include common-envelope evolution or chemically homogeneous evolution scenarios.

Common-envelope models (e.g Paczynski 1976; Eggleton 2006; Taam & Sandquist 2000; Belczynski et al. 2016) consider massive binaries which are initially on wide orbits. The more massive member will leave the main sequence sooner than its companion, migrate and swell. If it fills its Roche lobe, the smaller companion will accrete mass from its envelope, this in turn drives the stars closer together due to dynamical friction. The second star grows as it removes mass from the first star, which eventually collapses to a BH. When the second star leaves the main sequence and swells, its envelope will engulf the BH. Further dynamical friction tightens the orbit even more. Eventually, the envelope is lost and the second BH is formed, leaving a tight binary BH. While this model is capable of producing BH mergers within the age of the Universe, it also presents several problems. In particular, features of the stellar evolution, including modeling stellar winds and the common envelope phase introduce uncertainties in the process. Additionally, this particular process faces the problem that the stars can merge before they have collapsed to BHs.

Chemically homogeneous evolution models avoid the need for a common envelope phase by considering similar mass stars which rotate at high velocities. In these stars have thee gas constantly mixed by the rotation, which provides the nucleus with fresh fuel for nuclear reactions. These stars never undergo a swelling phase when their core is depleted of hydrogen, and compactness is conserved. The stars will eventually collapse when they have expanded their fuel, conserving almost all of their mass, and the BH binary is formed (e.g. Mandel & de Mink 2016; Marchant et al. 2016).

From a detection perspective, mergers originating from isolated field binary models are characterized by positive effective spin parameters (close to unity) and circular inspirals. As the stars evolve independently from surrounding objects, tidal torques have sufficient time to align the stellar spins with the orbital angular momentum of the binary (the effective spin can be reduced if for example the BH angular momentum

is tilted by natal kicks due to for example non-isotropic supernovae explosions, e.g. Wysocki et al. 2018).

Dynamical formation processes take place in the densest stellar environments of galaxies, such as globular clusters or the nuclear star cluster (NSC). They depend on the interaction with extra massive objects to remove energy from the binary orbits and facilitate mergers.

As in the previous case, several dynamical formation channels have been proposed. One of the more thoroughly explored models considers BH binaries in globular clusters. Stellar evolution models indicate that these systems should be capable of producing and retaining a population of BH binaries. Mass segregation and dynamical friction will drive these objects towards the centre of the cluster. On its path, a binary will encounter a series of compact objects (e.g. stars or black holes) which it will interact with. The binary will undergo a $(2+1)$-body interaction in which the two most massive of the three objects forming a tighter binary than the previous one, and the third being launched away having removed orbital energy from the binary. Numerical simulations show that a succession of interactions of this kind can result in tight enough binaries for mergers to be observed within the age of the Universe . For this to take place the system must be dense enough to provide new objects for the interactions and retain the binary, as it will receive a kick after each $(2 + 1)$-body event (Rodriguez et al., 2015, 2016).

In most galactic centres, with or without a massive black hole, dense environments known as Nuclear Star Clusters (NSCs) form over time (Arca-Sedda & Capuzzo-Dolcetta, 2019; Arca-Sedda & Gualandris, 2018). This is due to the in-fall of clusters from outer regions of the galaxy towards the centre, as well as field objects being scattered towards the galactic centre due to their interaction with the stochastic stellar potential. When MBHs are present, hierarchical triples can form. These are composed of an inner binary which orbits the MBH at large distance. In this situation, the secular Kozai-Lidov effect becomes relevant. This occurs due to the interaction of the inner binary with the MBH over long times, leading to a periodic exchange of eccentricity and binary inclination around the MBH. The process can lead the binary to phases of

very high eccentricity, during which it releases bursts of GW radiation and tightens its orbit until eventually the BHs merge (VanLandingham et al., 2016; Antonini & Rasio, 2016; Hoang et al., 2018).

Other dynamical processes have been shown to lead to GW mergers with varying rates (e.g. Mandel & Farmer 2018; Arca-Sedda et al. 2018). High-velocity close encounters of initially unbound BHs can lead to the release of GW Bremsstrahlung, which captures the objects in a BH (Gondán et al., 2018). These are very tight and eccentric upon formation, and are expected to quickly merge, giving rise to eccentric inspirals. AGN disks have also been proposed as a site for compact mergers. In these environments viscous and dynamical friction can efficiently remove energy from the binary, facilitating the coalescence (Tagawa et al., 2020; Leigh et al., 2018). In chapters 4-6, the tidal deformation of compact binaries due to close encounters with MBHs is investigated as a potential source of BH mergers.

In contrast to isolated field models, dynamical processes are expected to produce eccentric inspirals with a range of effective spin parameters (in most cases, the models predict uniformly distributed $\chi_{\rm eff}$-models). This is due to the binary orbits being constantly perturbed by external interactions, or binary members being exchanged with other objects with randomly oriented spins.

The possibility of hierarchical mergers has been considered, especially in the context of BHs with masses of the order of several tens of solar masses (Gerosa & Berti, 2017). The remnant object from a compact merger will generally receive a natal kick due to conservation of linear momentum. As was discussed above, if the host system or cluster is dense enough its gravity can retain the remnant. After this it can proceed to form another binary, and merge again, leaving an even larger remnant. While the details of this process are sensitive to the natal kick, which is difficult to constrain, hierarchical mergers are a potentially dominant source of BH-BH coalescence events (Antonini & Rasio, 2016). Kimball et al. (2020) found that several of the mergers reported in the second gravitational wave transient catalogue (Abbott et al., 2020b) are compatible with being the result of a first generation (1G) BH merging with a remnant from a past coalescence (2G), and two events which are candidates for a

2G+2G merger.

Chapter 3

Tidal encounter dynamics and the restricted three-body problem

Tidal forces are a key concept in gravitational physics. It follows from the equivalence principle that these forces are the only expression of the gravitational field which are detectable by a free-falling observer (by means of geodesic deviation) (Misner et al., 1973). Even from the point of view of classical gravity these forces are important: the Universe is made up not of point-like objects, but bodies with spatial extension. Given a large enough system, different parts of it will experience different gravitational fields. In many cases this can lead to tidal disruption or deformation of the system.

Most galaxies harbour a massive black hole (MBH) in their centres which dominates the local gravitational potential (Alexander, 2017). Dense environments known as nuclear star clusters (NSC) form around these objects which can host a great number of single and binary compact objects. In particular, observations of the Milky Way NCS indicate there is a population of up to hundreds of binaries in which at least one member is a compact object (Hailey et al., 2018), and simple analytic estimates yield a total population of ~ 20000 BHs (Miralda-Escudé & Gould, 2000; Morris, 1993; Rasskazov & Kocsis, 2019).

Observations of hypervelocity stars (HVS) and S-stars in the Milky way indicate that

binaries can interact with, and be disrupted by the central MBH. HVSs are stars ejected from the galactic centre at large velocities observed at current times in the halo (Brown, 2008). S-stars are a family of stars which orbit around the MBH on extremely eccentric orbits (e.g. Sabha et al. 2012). The origin of these two separate families of objects is linked by the Hills mechanism. In this picture, a stellar binary approaches the MBH. If the periastron of the orbit is close enough to the MBH the binary can be tidally disrupted (Brown, 2015; Hills, 1988) . One of the members launched away at a high velocity, becoming an HVS. The other is captured and bound to the MBH, adding to the population of S-stars. Whether the binary is disrupted or not depends on the characteristics of the $(2 + 1)$ system, including the inclination of the binary orbit with respect to that of the orbit around the MBH, the eccentricity and radius of the binary, or the periastron distance (Sari et al., 2010; Brown et al., 2018; Fernández & Kobayashi, 2019).

In this chapter the restricted parabolic three-body formalism is derived. This way, a perturbative equation of motion is obtained which greatly simplifies the numerical integration of the otherwise full three-body problem. This approach has been used to study the tidal disruption of compact binaries due to close encounters with MBHs in Sari et al. (2010); Kobayashi et al. (2012); Brown et al. (2018). It is used in chapters 4 and 5 to study the properties of post-encounter BH binaries. Finally, by means of angular momentum considerations, the *tidal torque* equation is derived, which illustrates how the MBH couples the different angular momenta of the system.

3.1 The restricted parabolic three-body problem

In this section the equation of motion describing the dynamics of a close-encounter between a compact binary and MBH is derived. The distance scales considered are much larger than the Schwarzschild radii of the BHs considered. Therefore, Newtonian gravitation can be used accurately. The derivation below follows Sari et al. (2010)

A three-body system, consisting of a compact binary with member masses $m_1,\ m_2$,

such that $m = m_1 + m_2$, and a third more massive object (the MBH) of mass $M \gg m$, is considered. A full description of the time evolution of this system would in principle imply solving 18 first order differential equations. As $M \gg m$, the MBH can be considered stationary at the origin. The equations of motion then read

$$\ddot{\mathbf{r}}_1 = -\frac{GM}{r_1^3}\mathbf{r}_1 + \frac{Gm_2}{|\mathbf{r}_1 - \mathbf{r}_2|^3}(\mathbf{r}_2 - \mathbf{r}_1) \tag{3.1}$$

$$\ddot{\mathbf{r}}_2 = -\frac{GM}{r_2^3}\mathbf{r}_2 - \frac{Gm_1}{|\mathbf{r}_1 - \mathbf{r}_2|^3}(\mathbf{r}_2 - \mathbf{r}_1), \tag{3.2}$$

where $\mathbf{r}_1,\ \mathbf{r}_2$ are the positions of the binary members with respect to the MBH. The tidal encounter can disrupt the binary or modify its orbit. To analyze this it is more interesting to study the evolution of the distance between the binary members $\mathbf{r} = \mathbf{r}_2 - \mathbf{r}_1$. Combining the previous equations,

$$\ddot{\mathbf{r}} = -\frac{GM}{r_2^3}\mathbf{r}_2 + \frac{GM}{r_1^3}\mathbf{r}_1 - \frac{Gm}{r^3}\mathbf{r}. \tag{3.3}$$

If the binary members are much closer to each other and to their centre of mass (COM) trajectory than to the MBH, then the previous equation can be simplified further. Therefore, assuming the COM moves on a trajectory $\mathbf{r}_m$, linearizing the first two terms in the equation 3.3 yields

$$\frac{\mathbf{r}_{1,2}}{r_{1,2}^3} \approx \mathbf{r}_m - 3\frac{\mathbf{r}_m}{r_m^5}\left[\mathbf{r}_m \cdot (\mathbf{r}_{1,2} - \mathbf{r}_m)\right] + \frac{\mathbf{r}_{1,2} - \mathbf{r}_m}{r_m^3}. \tag{3.4}$$

Inserting this result into equation 3.3 yields

$$\ddot{\mathbf{r}} = -\frac{GM}{r_m^3}\mathbf{r} + 3\frac{GM}{r_m^5}(\mathbf{r} \cdot \mathbf{r_m})\mathbf{r}_m - \frac{Gm}{r^3}\mathbf{r}. \tag{3.5}$$

Therefore, the solution the full three-body problem is reduced to specifying a trajectory $\mathbf{r}_m$ and solving equation 3.5. The approach of the binary to the MBH can be conveniently modeled by considering that the COM follows a parabolic path, with analytical form (e.g. Bate et al. 1971; Landau & Lifshitz 1980)

$$\mathbf{r}_m = \frac{2r_p}{1 + \cos f}\hat{\mathbf{r}}_m, \tag{3.6}$$

where r_p is the distance of closest approach (the periastron), $\hat{\mathbf{r}}_m = (\cos f, \sin f, 0)$ is the unit vector in the direction of the COM (assuming the trajectory is contained in the xy-plane) and f the true anomaly of the orbit. The true anomaly depends implicitly on the time coordinate through the relation

$$t = \frac{\sqrt{2}}{3}\sqrt{\frac{r_p^3}{GM}}\tan(f/2)(3 + \tan^2(f/2)). \tag{3.7}$$

Defining the dimensionless quantities

$$\begin{aligned} \tilde{\mathbf{r}} &= (M/m)^{1/3}\,\mathbf{r}/r_p, \\ \tilde{t} &= \sqrt{GM/r_p^3}\,t, \end{aligned} \tag{3.8}$$

the equation of motion 3.5 can be rewritten as (Sari et al., 2010)

$$\ddot{\tilde{\mathbf{r}}} = \left(\frac{r_p}{r_m}\right)^3 [-\tilde{\mathbf{r}} + 3(\tilde{\mathbf{r}} \cdot \hat{\mathbf{r}}_m)\hat{\mathbf{r}}_m] - \frac{\tilde{\mathbf{r}}}{\tilde{r}^3}. \tag{3.9}$$

This way, the full three-body problem is reduced to solving 3.9 which along with the differential form of 3.7,

$$\dot{f} = \sqrt{2}(1 + \cos f)^2/4, \tag{3.10}$$

that is, the original 18-first order differential equation problem is reduced to only 7 (Sari et al., 2010; Kobayashi et al., 2012; Brown et al., 2018).

To study whether the encounter disrupts a binary or not, it is convenient to analyze the energy of the binary members. The energy of a point particle on a parabolic trajectory is null. In the case of the binary, the energy is slightly negative due to its self-energy. However, this is much smaller than the binding energy to the MBH in its vicinity and can be neglected. Therefore, the energy of the i^{th} member reads

$$E_i = -\frac{GMm_i}{r_i} + \frac{1}{2}m_i|\dot{\mathbf{r}}_i^2|\,. \tag{3.11}$$

The terms in r_i can again be linearized around r_m, yielding

$$\frac{1}{r_i} \approx \frac{1}{r_m} - \frac{1}{r_m^2}\hat{\mathbf{r}}_m \cdot (\mathbf{r}_i - \mathbf{r}_m)\,; \quad |\mathbf{r}_i|^2 \approx |\mathbf{r}_m|^2 + 2\mathbf{r}_m \cdot (\mathbf{r}_1 - \mathbf{r}_m).$$

With this, to first order in $\mathbf{r}_m$ the energy reads

$$E_i = \frac{GMm_i}{r_m^2}(\mathbf{r}_i - \mathbf{r}_m) + m_i\dot{\mathbf{r}}_m \cdot (\dot{\mathbf{r}}_1 - \dot{\mathbf{r}}_m), \tag{3.12}$$

as the zeroth order contributions due to the parabolic orbit are null. Noting that in this approximation $E_1 = E_2$, by rearranging the combination $m_2E_1 - m_1E_2$ and rescaling the distance and time variables as before, then

$$E_1 = -\frac{GMm_1m_2}{mr_p}\left(\frac{m}{M}\right)^{1/3}\left[\frac{r_p^2}{r_m^2}\hat{\mathbf{r}}_m \cdot \mathbf{r} + \frac{\dot{\mathbf{r}}_m}{r_p} \cdot \mathbf{r}\right] = -E_2 \tag{3.13}$$

As the binary approaches the MBH, its members energies oscillate between $|E_1|$ and $-|E_1|$. If the tidal encounter disrupts the binary, one of the compact objects remains on a closed orbit around the MBH while the other is launched to infinity. In this case, the bound object has negative post-encounter energy and the other positive post-encounter energy. This makes it computationally simple to check whether a binary is disrupted or not.

3.2 The tidal torque

The angular momentum of the binary members around the MBH is given by

$$\mathbf{L} = m_1\mathbf{r}_1 \times \mathbf{v}_1 + m_2\mathbf{r}_2 \times \mathbf{v}_2, \tag{3.14}$$

where the MBH is at the origin. Using the binary positions relative to the COM $\Delta\mathbf{r}_{1,2} = \mathbf{r}_{1,2} - \mathbf{r}_m$, the angular momentum can be rewritten as the sum of two components

$\mathbf{L} = \mathbf{L}_m + \mathbf{L}_b$ where

$$\begin{aligned} \mathbf{L}_m &= m\mathbf{r}_m \times \dot{\mathbf{r}}_m, \\ \mathbf{L}_b &= m_1 \Delta\mathbf{r}_1 \times \Delta\dot{\mathbf{r}}_1 + m_2 \Delta\mathbf{r}_2 \times \Delta\dot{\mathbf{r}}_2 = \frac{m_1 m_2}{m}\mathbf{r} \times \dot{\mathbf{r}}. \end{aligned} \tag{3.15}$$

The COM angular momentum $\mathbf{L}_m$ and the binary angular momentum $\mathbf{L}_b$ can change at the tidal encounter. However, since the binary system moves in the central force field, the total vector $\mathbf{L}$ should be conserved. Using the equation of motion (3.5), the evolution of $\mathbf{L}_b$ is given by (Fernández & Kobayashi, 2019)

$$\dot{\mathbf{L}}_b = \frac{3GMm_1m_2}{mr_m^3}(\mathbf{r} \cdot \hat{\mathbf{r}}_m)\mathbf{r} \times \hat{\mathbf{r}}_m. \tag{3.16}$$

Expanding this equation out in components shows that the effect of the torque depends on whether the binary orbit is coplanar with the COM trajectory or not:

- **Coplanar binaries** experience a torque which acts along the direction of their initial angular momentum $\mathbf{L}_{b,in}$. Therefore the tidal encounter will not rotate the orbital plane. However, it can spin-up or spin-down the binary. In particular, sufficient spin-down can flip the binary orbital plane so that $\mathbf{L}_{b,out}$ is anti-parallel to $\mathbf{L}_{b,in}$.
- **Tilted binaries** on the other hand experience a torque with components perpendicular to $\mathbf{L}_{b,in}$. Their orbital planes can be rotated by the tidal encounter. They also experience parallel components of torque leading to spin-up or spin-down (this results is important for the numerical experiments described in chapter 4 and onwards).

Chapter 4

Black hole mergers induced by tidal encounters with a MBH

The tidal disruption of stellar binaries by a MBH is a process well known to produce hypervelocity stars (Hills, 1988; Yu & Tremaine, 2003). In this picture, the gravity of the MBH overcomes the self-gravity of the binary. One of the stars becomes bound to the MBH, and conservation of energy leads to the other moving away from the MBH at high speeds. However, such a tidal encounter does not always lead to the break-up of binaries. Previous numerical studies have revealed that about 10% of binaries can survive such an encounter even for deep penetrations (Sari et al., 2010; Brown et al., 2018). Since surviving binaries tend to become hard and eccentric, this process can provide a new formation channel of BH mergers.

In this chapter the properties of stellar mass black hole (BH) mergers induced by tidal encounters with a massive BH at galactic centres, or potentially in dense star clusters, are discussed. The post-encounter orbital parameters of the survivors are characterized. It is shown that the gravitational wave (GW) merger times become shorter by a factor of more than 10^2 (10^5) in 10% (1%) of the surviving cases. The effective spins of the surviving binaries are also obtained, assuming that the spins of BHs in binaries are initially aligned with their binary orbital angular momenta and that they are constant during the encounter. A key result is that the binary orientations can flip in the opposite

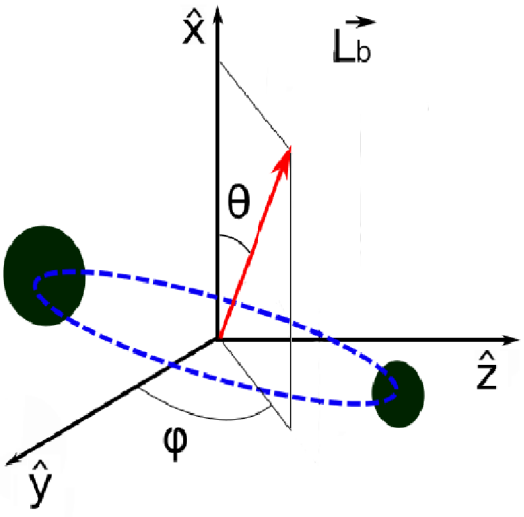

Figure 4.1: The binary angular momentum $\hat{\mathbf{L}}_b$ is defined in the rest frame of the binary's COM. The same set of unit vectors $\hat{\mathbf{x}}$, $\hat{\mathbf{y}}$ and $\hat{\mathbf{z}}$ is used to represent the axes of a Cartesian coordinate system (the coordinate axes in the binary's COM rest frame are parallel to those in the massive BH rest frame). The polar angle θ is defined as the angle between $\mathbf{L}_b$ and $\hat{\mathbf{x}}$. With this parameterisation, the outcome of the tidal encounter does not depend on the azimuth angle φ for $D \ll 1$, because the COM moves along the x axis in the massive BH rest frame (the parabolic orbit becomes radial for $D \ll 1$).

direction at the tidal encounter. For the survivors with large merger time reduction factors of 10^5, the effective spin distribution is asymmetric, but rather flat [1].

4.1 Problem setup

To simplify the analysis, in this chapter the discussion is limited to circular binaries. This reduces the dimension of the system parameter space by two (characterization of non-circular binaries requires the eccentricity and orientation of the semi-major axis to be specified). In the restricted three-body approximation, the system's initial conditions are fully characterized by the orbital plane orientation, given by the unit vector $\hat{\mathbf{L}} = (\cos\theta, \sin\theta\cos\varphi, \sin\theta\sin\varphi)$ (this is illustrated in figure 4.1); the binary phase at periastron ϕ and the penetration factor $D = r_p/r_t$.

The binaries are injected into parabolic orbits far out from the tidal radius. The binary evolution is largely independent of r_m if the simulations start at a large enough radius

[1] The results in this chapter have been published as Fernández & Kobayashi (2019).

$r_{m,0} = r_t$. In this work $r_m = 10r_t$ is set. The initial binary phase (at $t_0 = t(r_0) < 0$), $\phi_0 = \omega t_0 + \phi$ is characterized by using the effective phase at ϕ at $t = 0$ (i.e. at periastron passage), where ω is the constant angular velocity of the binary at $r_m \gg r_t$. The actual phase at $t = 0$ is in general different from ϕ due to the tidal force of the MBH. If the angular momentum $\mathbf{L}_b$ is in the z-direction (a planar, prograde case), the initial binary phase ϕ_0 is the angle between $\mathbf{r}$ and $\hat{\mathbf{y}}$ at $t = t_0$. In the general case, the initial separation vector $\mathbf{r}$ and initial velocity $d\mathbf{r}/dt$ are defined assuming a planar prograde case, and are rotated so that $\mathbf{L}_b$ points in the (θ, φ) direction (see figure 4.1).

The equation of motion 3.9 is integrated together with 3.10 using a fourth-order Runge Kutta scheme (Press et al., 1992). To ensure the accuracy of the dynamical evolution, at each instant the time-step width Δt is chosen to be the smallest between the characteristic orbital time of the binary t_{bin} and the free-fall time of the parabolic orbit t_{par}, multiplied by a normalization factor h. That is, the time-step is set at each instant to be $\Delta t = h \cdot \min\{t_{\text{bin}}, t_{\text{par}}\}$, where t_{bin} is evaluated from the instantaneous orbital parameters of the binary and t_{par} is fixed by the parabolic orbit. The normalization factor is set so that both the inner binary orbit and the COM parabolic orbit are sampled with sufficient resolution while allowing for time-efficient solution of the equations. This is especially important in the case of survivors with significantly reduced semi-major axes. Due to their short orbital periods the time -steps can be extremely small. Therefore, if h is too small these systems can result in a computational bottleneck . For the simulations described in this work the normalization factor is set to $h = 10^{-3}$. It was found that was more than sufficient to adequately sample the dynamics (smaller time-steps showed no appreciable increase in accuracy when compared to the full three-body calculations), while allowing for swift numerical resolution. The accuracy of the restricted three-body formalism and the numerical code are described in detail below, in section 4.2.

As was discussed in chapter 2, a parameter of great interest for aLIGO/VIRGO observations is the effective spin χ_{eff} of the binary, defined as

$$\chi_{\text{eff}} = \frac{1}{m}(m_1\mathbf{S}_1 + m_2\mathbf{S}_2) \cdot \frac{\mathbf{L}_b}{|\mathbf{L}_b|}, \tag{4.1}$$

where $\mathbf{S}_{1,2}$ are the dimensionless spins of the BHs in the binary, bound by $0 \leq S_{1,2} \leq 1$ (Farr et al., 2017). It then follows that $0 \leq \chi_{\text{eff}} \leq 1$. The BH spins do not intervene in the Newtonian treatment of the tidal encounter, as classical point-like objects cannot carry internal angular momentum. Therefore, these vectors are constant in this description. This approximation remains valid as long as the binary separation and the distance to the MBH are much larger than their horizon scales.

As was shown in the previous chapter, the dynamics of the tidal encounter does not directly depend on the masses of the binary members. Restricted three-body results can be simply rescaled in terms of their masses. However, the mass ratio m_1/m_2 is required to evaluate the effective spin. Considering that many of the BH mergers detected by LIGO/Virgo so far are consistent with equal mass members, $m_1 = m_2$ is assumed when the effective spin χ_{eff} is discussed. Unless stated otherwise, the BH spins are taken to be initially parallel to $\mathbf{L}_b$. In this case the effective spin of the survivors indicates whether and to what extent the binary orientation changes at the tidal encounter. For simplicity, it is also assumed that $S = |S_1| = |S_2|$. Then for an equal-mass binary equation 4.1 becomes

$$\chi_{\text{eff,out}} = S\, \hat{\mathbf{L}}_{b,in} \cdot \hat{\mathbf{L}}_{b,out}, \tag{4.2}$$

4.2 Binary hardening and orbital plane-rotation due to tidal encounters

To illustrate the effect of the tidal encounter on the inner-orbits of surviving binaries, a coplanar case for $D = 1$ is considered. The orbit of the secondary component in the primary component comoving frame is shown in figure 4.2. The red line is the orbit as calculated using the restricted three-body approximation. In this case, the initially circular binary emerges from tidal encounter with large eccentricity $e = 0.97$ and the the semi-major axis is reduced by a factor of 2.7. The ratio of in-going-to-outgoing

GW merger times is well approximated by the formula

$$\frac{\tau_{gw,out}}{\tau_{gw,in}} \sim (1-e^2)^{7/2}\left(\frac{a}{a_0}\right)^4, \tag{4.3}$$

where a_0 is the pre-encounter semi-major axis. Using this relation, it is found that in this case τ_{gw} is reduced by a factor of $\sim 10^6$ by the tidal encounter. The black dashed dotted line indicates the orbit obtained with the full three body treatment. The two results are almost identical in the figure, illustrating the accuracy of the restricted three-body approximation.

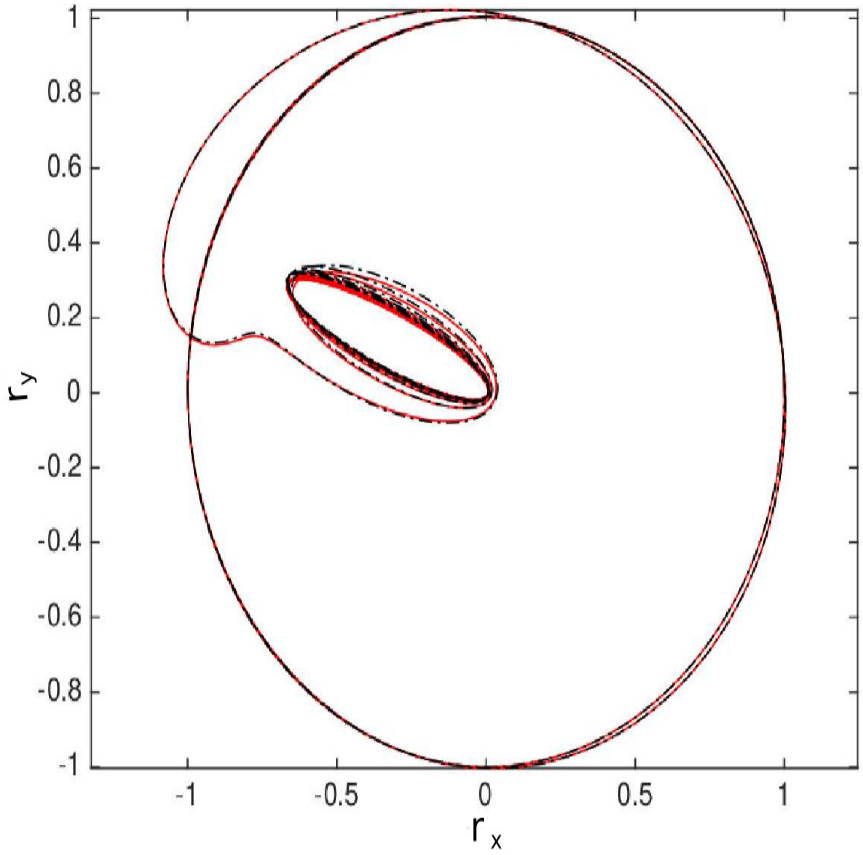

Figure 4.2: The evolution of binary separation vector $\mathbf{r} = \mathbf{r}_2 - \mathbf{r}_1$. This is equivalent to the orbit of the secondary component in the primary component comoving frame. A prograde binary orbit with $D = 1$ is assumed to evaluate the restricted three-body approximation orbit (red solid line). The black dashed-dotted line indicate the full three-body orbit. The binary mass ratios are assumed to be $m_1/m_2 = 3$ and $M/m = 10^5$ for the full three-body calculations. Lengths are in units of the initial binary separation a_0.

The orbital plane of binaries which are initially non-coplanar with the COM motion can

be rotated by the tidal encounter. Even small misalignment can lead to flipping of the orbital plane, i.e $\chi_{\rm eff} \sim -1$. To illustrate this, the almost coplanar case $\theta = 0.5\pi, \varphi = 0.6\pi$ is considered for $D = 0.5$ (left column) and $D = 1.0$ (right column) for a range values of the binary phase at periastron ϕ. Several post-encounter system parameters were obtained as a function of ϕ, including $\chi_{\rm eff},\ e,\ \tau_{gw,out}/\tau_{gw,in}$ and the semi-major axis a. These are shown in figure 4.3. The figure only shows surviving systems. Therefore, for D=0.5 (D=1.0) the gaps between $\phi \sim 0.725\pi$ and 0.81π ($\phi \sim 1.38\pi$ and 1.535π) indicate that all the binaries in this range were disrupted. The binary orientation, given by $\hat{\mathbf{L}}_b$ flips to almost the opposite direction in the border regions. Disrupted binaries have $e > 1$. As expected, the eccentricity and the semi-major axis of the survivors grow at the border regions. The wide separation of binaries near the disruption binaries may help induce a large torque in equation 3.16 (as they would act as long lever arms), resulting in the negative effective spins at the boundaries. It is also found that binaries near the disruption regions and inside the survival regions can emerge with significantly reduced τ_{gw}.

4.2.1 Validity of the restricted three-body formalism

The restricted parabolic three-body formalism is based the assumption that the binary COM approaches the MBH on a parabolic orbit. This places constraints on the energy and angular momentum of the system.

The gravitational field is conservative, implying that the total energy of the system is constant. Binary shrinking (stretching) leads to energy being injected into (removed from) the COM orbit. Therefore, in general the post-encounter COM orbit will be hyperbolic or elliptical. However, the released energy is extremely small compared to the kinetic energy associated with the velocity of the COM at tidal radius (for the trajectory in figure 4.2, the released energy corresponds to $\Delta E \sim 0.16Gm^2/a_0$, a fraction of the binary internal kinetic energy which itself is much smaller than that of the COM). Therefore, the parabolic description is a valid approximation even after the tidal encounter).

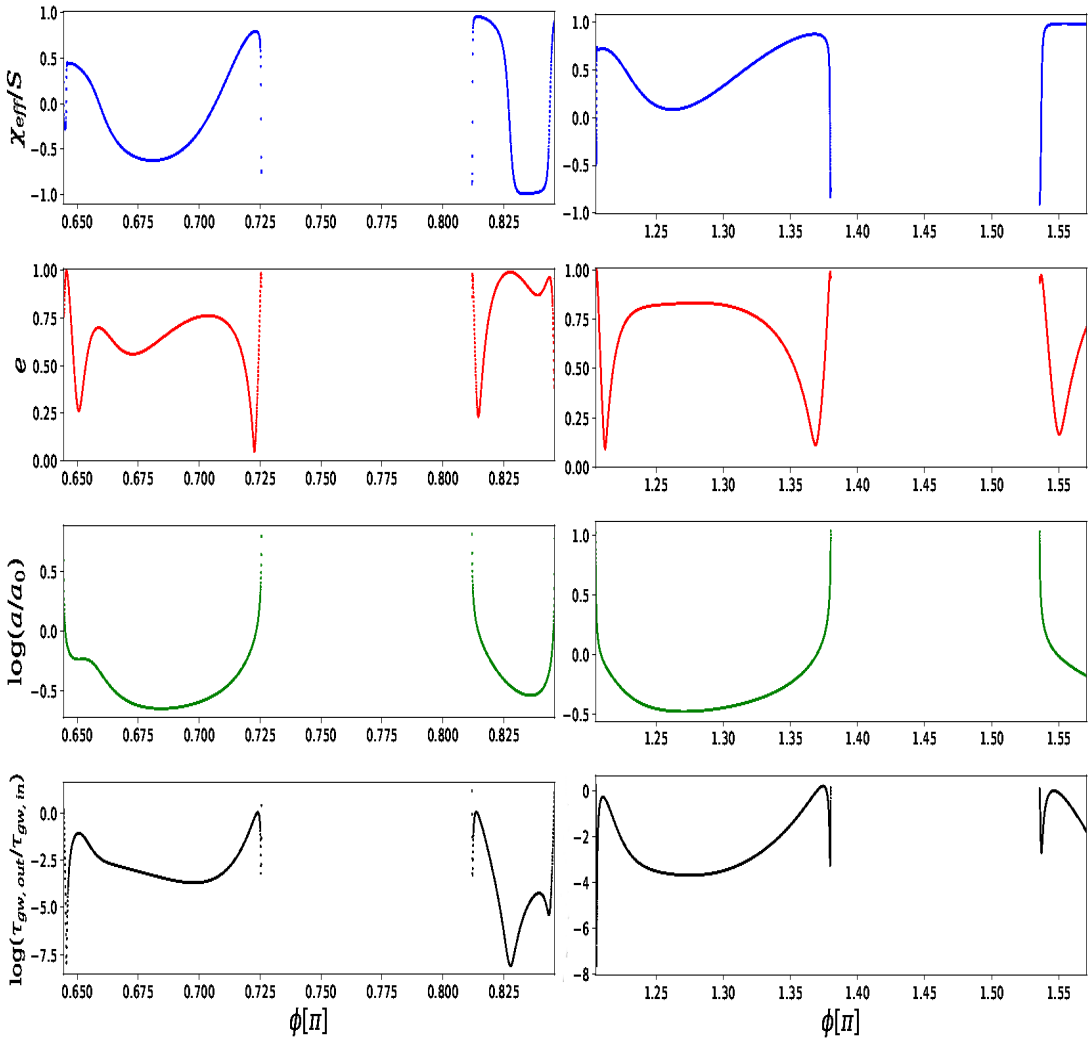

Figure 4.3: Surviving binaries. Left column: $D = 0.5$. Right column: $D = 1.0$. From top to bottom the post-encounter effective spin, eccentricity, semi-major axis and the ratio of the GW merger times before and after the tidal encounter are given as a function of ϕ. The assumed initial orientation is $\theta = 0.5\pi,\ \varphi = 0.6\pi$.

The orbit around the tidal radius is still very close to the initial parabolic orbit. Even if the initial COM orbit is not exactly parabolic, the approximation is still accurate. Assuming an orbit energy of the COM $E_m = \kappa(Gm^2/a_0)$, the full three body evolution is numerically evaluated for a binary with $D = 1, \theta = p0.6\pi, \varphi = 0.5\pi, \phi \sim 0.4\pi$, $M = 4 \times 10^6 M_\odot$ and $m_1 = m_2 = 30 M_\odot$. The results are compared with the restricted parabolic approximation results for the same set of the four parameters D, θ, φ and ϕ. In both calculations, the binary survives the tidal encounter with the massive BH. The differences of the semi-major axis, eccentricity and merger time are $\Delta a/a \sim 0.4\%, 4\%$

and 2%, $\Delta e/e \sim 0.07\%, 0.6\%$ and 1%, and $\Delta\tau_{gw}/\tau_{gw} \sim 3\%, 20\%$ and 20% for $\kappa = 1, 10$ and 100, respectively. Since the merger time is sensitive to a and e, the error in the merger time is rather large for $\kappa \gtrsim 10$. However, for the present discussion, only the order-of-magnitude estimate of τ_{GW} is needed (or a few 10% error in the τ_{GW} estimate does not affect the conclusions). Even for $\kappa = 100$ (for which the COM velocity at large distances from the massive BH is about one order of magnitude larger than the binary rotation velocity), the restricted parabolic approximation gives reasonable results.

Similarly, conservation of the total angular momentum of the three-body system is guaranteed, as only central forces are present in the dynamics. If the binary orbital plane is rotated (or if it becomes eccentric without changing its semi-major axis), angular momentum is exchanged with the COM orbit. Recalling equations 3.15, and considering equal mass binaries, then up to factors of order unity the angular momentum of the binary is $L_b \sim \sqrt{aGm}$ (up to factors of order unity). Similarly, for the parabolic orbit $L_m \sim \sqrt{r_p GM}$. Therefore the ratio of binary to COM angular momentum is roughly given by

$$\frac{L_b}{L_m} \sim \left(\frac{m}{M}\right)^{2/3} D^{-1/2}. \tag{4.4}$$

Assuming a stellar mass binary and a typical central MBH with $M \sim 10^6 M_\odot$, the ratio is of order $10^{-4} D^{-1/2}$. Therefore, even for deep encounters (e.g $D \sim 10^{-3}$), $L_b \ll L_m$. Therefore, even a flip of $\mathbf{L}_b$ would not significantly effect $\mathbf{L}_m$, ensuring the validity of the restricted parabolic approximation.

4.3 Numerical study

This section is dedicated to characterizing the properties of binaries which survive the tidal encounter. Even in the restricted three-body formalism, this system presents a rich parameter space. Therefore, Monte Carlo simulations are used to analyse the dynamics.

In section 4.3.1 the penetration factor dependence is characterized, and in 4.3.2 the full parameter space is explored. As discussed above, the treatment in this chapter is limited to circular binaries. Symmetry considerations are used to reduce the parameter space volume which must be explored. In particular, following the discussions in Brown et al. (2018), the binary orientation is taken to be isotropic on the hemisphere defined by $0 \leq \theta \leq \pi/2$, $0 \leq \varphi \leq 2\pi$. For sampled each binary orientation, the binary phase is drawn from a uniform distribution in the range $0 \leq \phi \leq \pi$.

4.3.1 Penetration factor dependence

The penetration factor D is a key parameter in the description of the tidal encounter dynamics. If the periastron r_p is located well outside the tidal radius r_t, the binaries are not affected by the tidal force of the MBH during a single encounter. Numerical simulations show that all binaries survive for $D > 2.1$. Therefore, the main discussion is limited to penetration factors below this threshold value. For smaller D, the survival probability decreases roughly linearly $P_{sur} \propto D$, leveling off at $P_{sur} \sim 10\%$ around $D = 0.1$. This is shown in figure 4.4. In this figure the separate survival probabilities for prograde (defined as having $L_{b,z} > 0$) and retrograde ($L_{b,z} < 0$) binaries are also given. The survival probability for retrograde binaries is significantly larger, even for deep penetrations. This is in agreement with previous studies of the stability of hierarchical triple systems (Grishin et al., 2017).

Figure 4.5 shows the distributions of the semi-major axis (top panel) and eccentricities (middle panel) of the survivors, obtained by randomly sampling 1000 binary orientations and more than 200 binary phases. The Monte Carlo sampling was carried out for $D = 0.25,\ 0.5,\ 0.75,\ 1.0$, and 2. It is found that the distributions (especially the eccentricity distribution) are insensitive to D. Except in the $D = 2$ case, the distributions are similar to each other. For 3% of the survivors, the semi-major axes are reduced by a factor of > 2 with respect to the pre-encounter separation a_0. The survivors are eccentric in general, and about 10% have very high eccentricity $e > 0.9$.

The GW merger time reduction factors are shown in the bottom panel of figure 4.5.

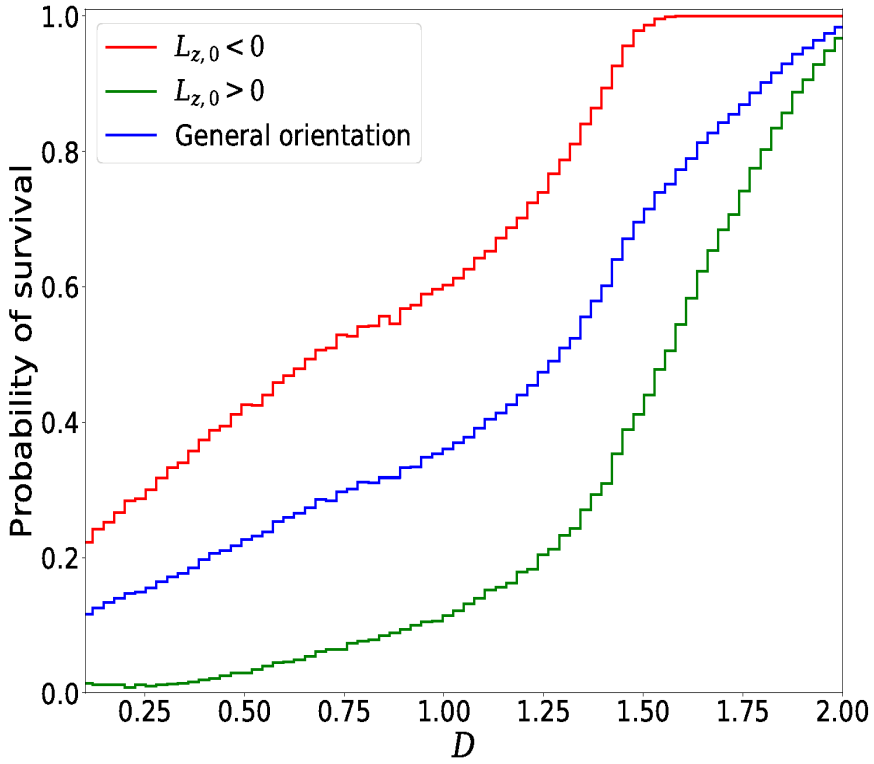

Figure 4.4: Probability of surviving the tidal encounter, as a function of D. The probability is integrated over the other binary parameters θ, φ, ϕ. This is given for general orientation (blue line), initially retrograde binaries (red) initially prograde binaries (green).

From equation 4.3 it is clear that this parameter has a strong dependence on the semi-major axis and eccentricity of the binary. As before, the distributions are very similar to each other, except in the $D = 2$ case. About 10% (1%) of the survivors have GW merger times shorter by a factor of 100 (10^5) or more when compared to the pre-encounter merger times. For $D > 2$ it is found that the merger time reduction achieved decreases rapidly (e.g for $D = 2.5$, GW merger times shorter by a factor > 10 (> 50) in 10% (1%) of cases, while for $D = 3$ practically all of the binaries are unaffected by the encounter).

The orientations of the binaries can also change significantly at the tidal encounter. The blue line in figure 4.6 indicates the probability of getting a survivor with a negative effective spin as a function of D (i.e. the probability that the binary survives the tidal encounter and the surviving binary has a $\chi_{eff} < 0$ when a binary with a random orientation and binary phase is injected with a given D). The distribution is found to be bimodal with peaks around $D = 0.4$ and $D = 1.5$. Since the surviving probability is

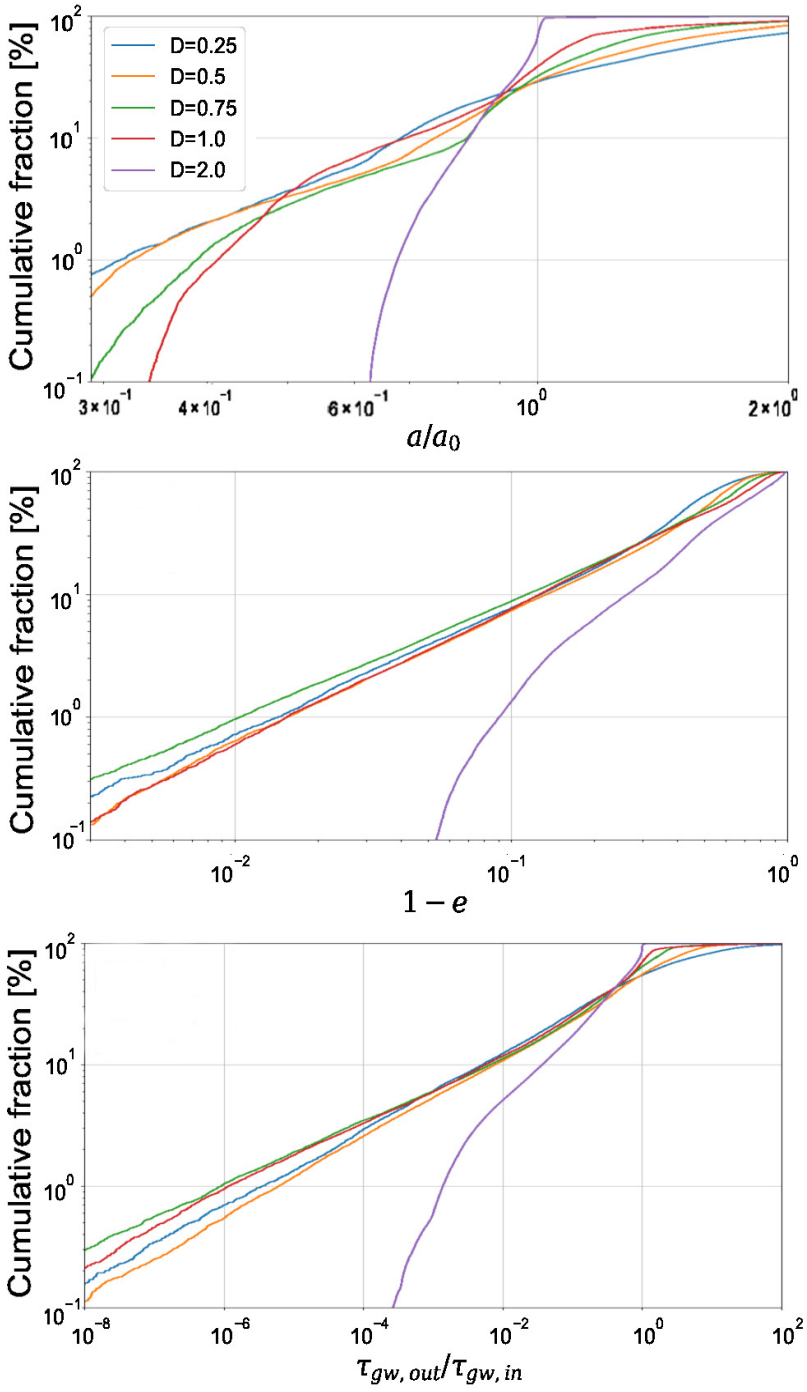

Figure 4.5: Distributions of the semi-major axes a (top panel), eccentricity differences $1-e$ (middle panel) and GW merger times $\tau_{gw,out}$ (bottom panel) of the survivors. The semi-major axis and GW merger times are given in units of the pre-encounter values a_0 and $\tau_{gw,in}$. The distributions are obtained from the Monte Carlo sampling with fixed $D = 0.25,\ 0.5,\ 0.75,\ 1.0$ and 2.

close to linear in D, the peaks indicate that a significant fraction of survivors ($\sim 40\%$) have negative effective spins around $D = 0.4$ (the fraction is around $10-15$ % for

D=1-1.5), and the fraction drops sharply for $D > 1.5$.

To investigate how the results depend on the initial binary orientation, the Monte Carlo sample is split into two groups, one for which binaries are initially prograde ($L_{b,z} > 0$) and one for which they are initially retrograde ($L_{b,z} < 0$) where $L_{b,z}$ is the z-component of the pre-encounter angular momentum $\mathbf{L}_b$. The green and red lines in 4.6 correspond to the prograde and retrograde cases, respectively. The distributions are normalized so the sum of the two gives the total distribution, i.e. they have been multiplied by $1/2$. The peak around $D = 0.4$ is due to retrograde binaries (the red line). Prograde binaries are known to be more vulnerable to tidal disruption. Accordingly, the surviving probability for the prograde group rapidly decreases for deeper encounters $D < 2.1$. Since the surviving probability of the order of a few percent for the prograde group, and around 40% for the retrograde group, the domination of this peak by the latter is not surprising. Since the surviving probability for the retrograde group is roughly linear in D for $D < 1.5$, it indicates that a good fraction ($\sim 40\%$) of retrograde binaries will significantly change their orientations around $D = 0.4$.

4.3.2 The entire population of survivors

The properties of the BH binary populations in the Universe are still highly uncertain. The distribution of penetration factors D is likely to be susceptible to the complicated galactic centre dynamics (Merritt, 2013; Alexander, 2017; Bradnick et al., 2017). The loss cone for tidal breaking of binaries may be empty. However, Weissbein & Sari (2017) have recently shown that rare large scatterings can play a significant role, and the tidal encounter events which occur well inside the cone are almost as common as those with $D = 1$. Here two simple D distributions are assumed: $P(D) \propto D^{\alpha}$ ($\alpha = 0$ or 1) to illustrate the tidal encounter model. These correspond to situations close to the full loss cone regime, i.e. binaries are scattered rather efficiently towards the MBH. If $D \gg 1$ the binary survives the encounter, and its properties do not change. To limit the discussion to strictly tidal encounters (events which can disrupt binaries), the range of $0 < D < 2.1$ is considered to characterize the process. While the encounter can

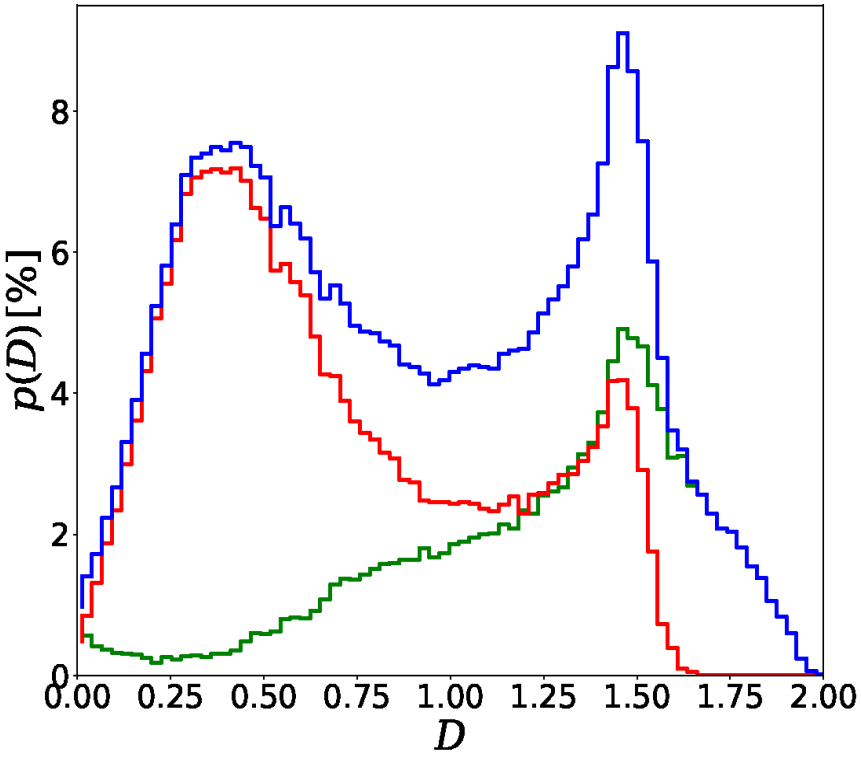

Figure 4.6: Probability of survival with negative $\chi_{\rm eff}$ as a function of D. The initial binary orientations are assumed to be isotropic (blue line), upward ($L_{b,z} > 0$; green line) or downward ($L_{b,z} < 0$; red line)

reduce the merger time for shallower penetrations, this effect is strongly suppressed for $D > 2.1$, and this upper limit does not significantly affect the main results[2].

The binary orientations $\{\theta, \varphi\}$ and the binary phase ϕ are again assumed to be uniformly distributed. For each D-distribution, more than 4×10^5 random realizations $\{D, \theta, \varphi, \phi\}$ are generated. An overall surviving probability of 47% (54%) is found for $\alpha = 0$ ($\alpha = 1$).

In figure 4.7 the distributions of the binary parameters are given. As was discussed above, the survivor properties are rather insensitive to D. Therefore, the two D-distributions yield similar results (the red lines correspond to $\alpha = 0$, the blue solid/dashed lines to $\alpha = 1$. The distribution of semi-major axes peaks sharply at $a/a_0 = 1$ (top left panel), and $\sim 50\%$ of the survivors have semi-major axes smaller than their initial values a_0. It is also found that $a/a_0 < 0.5$ in $\sim 1\%$ of cases. The eccentricities of the surviving

[2]This also ensures consistency with the event rate estimate presented in section 4.5.

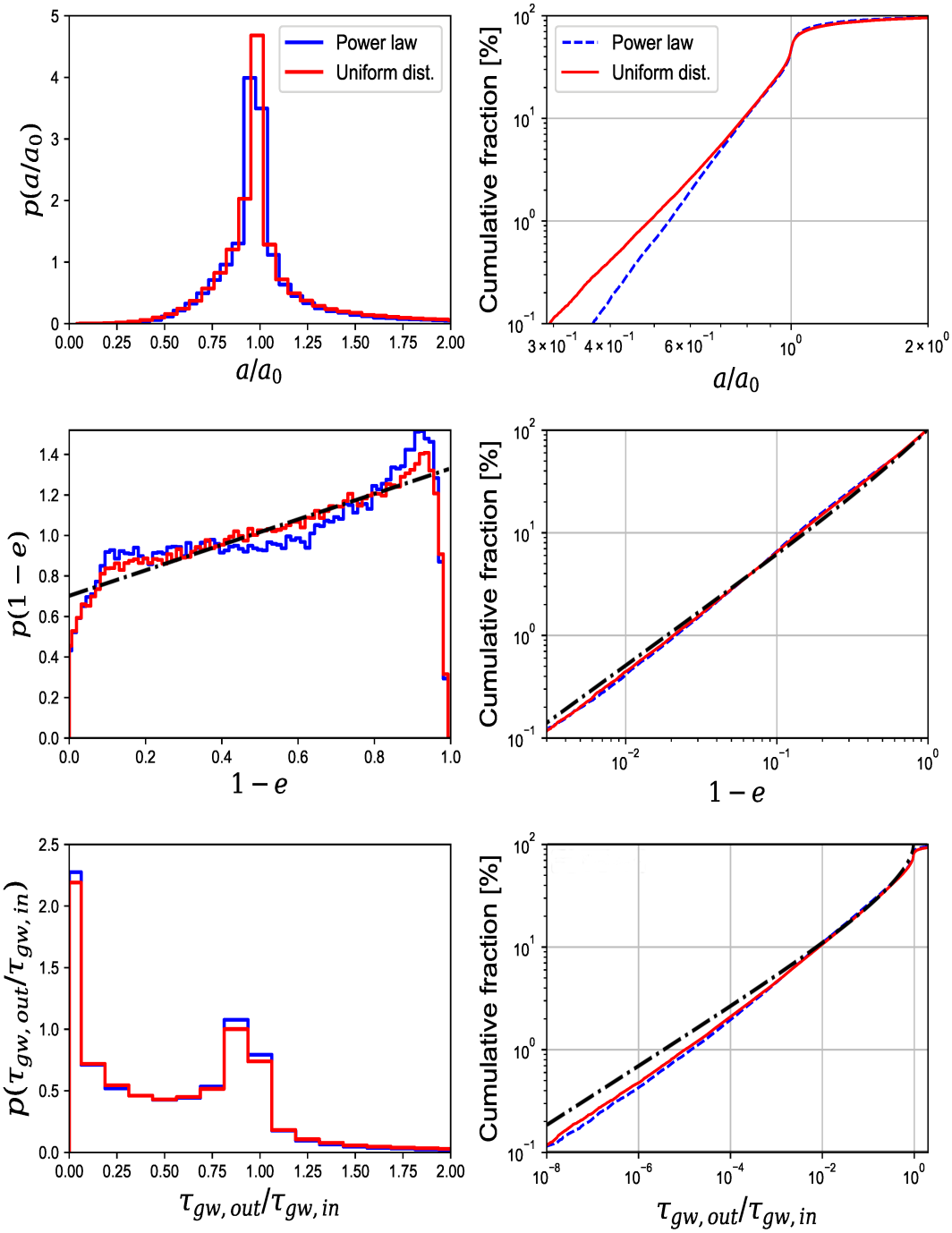

Figure 4.7: Orbital parameters of survivors: a (top panels), $1-e$ (middle panels) and $t_{gw,out}/t_{gw,in}$ (bottom panels). The left panels indicate their probability distribution functions, and the right panels are for the cumulative distributions. The uniform D distribution ($\alpha = 0$) and the power-law distribution ($\alpha = 1$) results are shown by the red solid and blue dashed lines, respectively. a is in units of the initial separation a_0. The black dashed-dotted lines indicate a linear fit to the eccentricity distribution for the $\alpha = 0$ case (middle panels), and the analytic cumulative distribution of merger time reduction factors (bottom right panel).

systems are much more spread out (middle left panel). About 50% of the survivors have $e > 0.5$, and several percent very large eccentricity $e > 0.9$. These orbital changes significantly reduce the GW merger times of the survivors. The distribution of merger time reduction factors (bottom left panel) is found to be bimodal in linear space. A fraction of 10% (1%) of the binaries have their merger times reduced by a factor of 10^2 (10^5) or more.

It is primarily the growth in eccentricity, rather than the hardening of the binaries, that causes the GW-driven merger time-scale to shrink following tidal interactions. To illustrate this, it can be shown that the $\tau_{gw,out}/\tau_{gw,in}$ distribution can be reproduced from the eccentricity distribution. For the $\alpha = 0$ case, the probability distribution function of the eccentricity can be fit with a linear function $P = (1 + s) - 2se$, where $s \sim 0.31$. This linear function satisfies the normalization condition $\int_0^1 P(e)de = 1$. The probability function of $(1 - e)$ is shown as the black dashed-dotted line in the middle left-hand side panel of figure 4.7. It can be seen that the linear approximation describes the numerical results (the red solid line) reasonably well, except for $(1 - e) \sim 0$ or 1. Since the merger time reduction factor $\tau_{gw,out}/\tau_{gw,in}$ is proportional to $\xi \equiv (1 - e^2)^{7/2}$, the distribution of ξ would give that of the reduction factor if the binary hardening is negligible. Using the distribution function of the eccentricity, the cumulative distribution function of ξ is found to be $P(> \xi) = (1+s)\left(1 - \sqrt{1 - \xi^{2/7}}\right) - s\xi^{2/7}$. This analytic function describes the numerical reduction factor distribution (the red solid line) reasonably well. In particular, it gives 1.3% (11%) for $\xi = 10^{-5}$ ($\xi = 10^{-2}$), which closely matches the numerical results. The overestimate at low values $\tau_{gw,out}/\tau_{gw,in} << 1$ originates from the linear fit to the eccentricity distribution $P(1-e)$, which overestimates the fraction of extremely eccentric survivors $e-1 \to 0$. The non-cumulative distribution of ξ can also be analytically evaluated for $0 \leq \xi \leq 1$, giving $P(\xi) \propto \xi^{-5/7}(1 - \xi^{-2/7})^{-1/2}$. This function has a U-shape, with peaks at $\xi = 0, 1$. In the bottom left-hand side panel of 4.7, the high-side tail, corresponding to cases with $\tau_{gw,out}/\tau_{gw,in} > 1$, is due to survivors with $a > a_0$.

In Addison et al. (2019) the properties of survivors are studied using full three-body calculations. Assuming a uniform D-distribution for $0.35 < D < 5$, they found a

semi-major axes distribution very similar to that presented in this chapter. They also find that most of the surviving binaries in their sample are relatively unperturbed in eccentricity, but have shown that a small fraction can become very eccentric after the encounter.

To estimate the effective spin of the surviving systems, three situations are considered. The first is the canonical case, with $\mathbf{S}_{1,2}$ initially parallel to $\mathbf{L}_b$. The other two cases account for possible misalignment mechanisms (e.g BH natal kicks). For these, the BH spin amplitudes are assumed to be the same $S = S_1 = S_2$, but are given random and independent directions: uniformly distributed in the cone with angle $\pi/4$ around $\mathbf{L}_{b,in}$, or sampled from a normal distribution with standard deviation $\pi/4$ and centred on $\mathbf{L}_{b,in}$, where the in subindex indicates the pre-encounter angular momentum. The resulting effective spin distributions are shown in figure 4.8 for the three BH spin models (aligned: blue line, uniform in the cone: green dashed-dotted line, normal: red solid line). It is found that all three distributions are similar to each other for $\chi_{\rm eff} < 0$. About 7% of survivors have negative effective spins.

While the $\chi_{\rm eff}$-distributions were evaluated for the entire population of survivors, only a fraction of them have short GW merger times, or more precisely, significant reduction factors for the merger times. The effective spin distribution based on the aligned spin model was evaluated for survivors with reduction factors $\tau_{gw,out}/\tau_{gw,in} < 10^{-5}$. It is found that this distribution is much flatter (see the left panel of figure 4.8), and that 39% of this population have negative effective spins. It is also found that 19% of survivors with $\tau_{gw,out}/\tau_{gw,in} < 10^{-2}$ have negative effective spins.

4.4 Constraints from the $\chi_{\rm eff}-$measurements

The effective spins of the BH mergers observed by LIGO/Virgo so far are clustered around $\chi_{\rm eff} \sim 0$, they are consistent with low effective spins within $-0.5 < \chi_{\rm eff} < 0.5$ at the 90% credible level (Abbott et al., 2016, 2017a,b,d; Belczynski et al., 2020; Abbott et al., 2020b). The small values of the effective spins can result from either

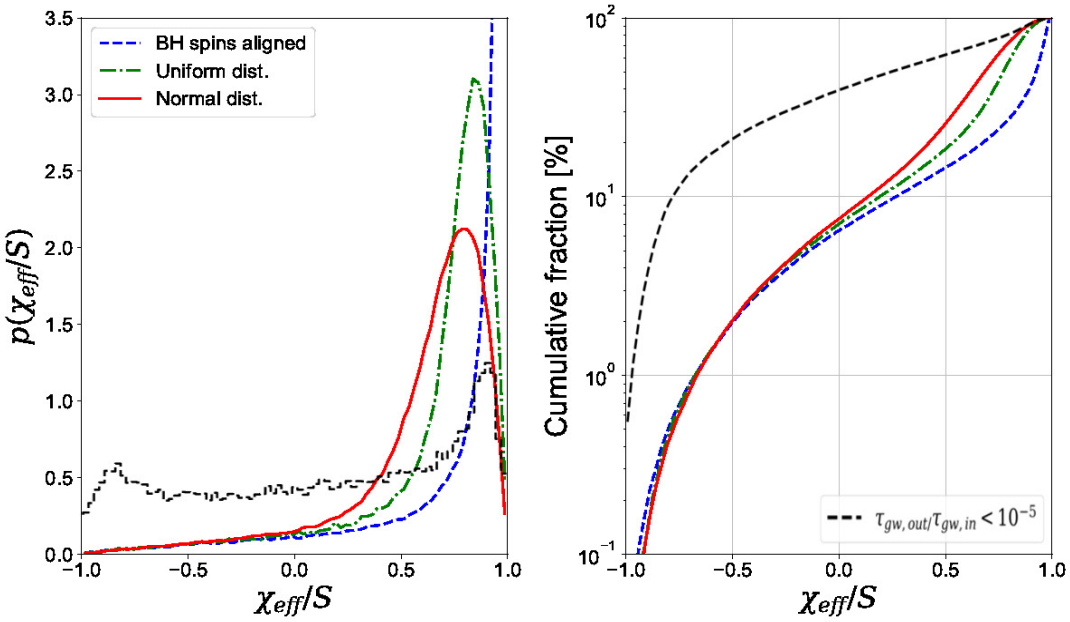

Figure 4.8: Effective spin distributions of survivors (left panel) and their cumulative distributions (right panel). The BH spins are aligned with the $\mathbf{L}_{b,in}$ (blue dashed line), uniformly distributed in the cone with opening angle $\pi/4$ around $\mathbf{L}_{b,in}$, or normally distributed with a standard deviation $\pi/4$ around $\mathbf{L}_{b,in}$. The black dashed line corresponds to survivors with $\tau_{gw,out}/\tau_{gw,in} < 10^{-5}$. The uniform D-distribution is assumed for all cases. The effective spin $\chi_{\rm eff}$ is given in units of the individual BH spin S.

intrinsically small BH spins S or large BH spins whose directions are misaligned with the orbital angular momentum of the binary $\mathbf{L}_b$. Positive effective spins have been detected in three cases: GW151226, GW170729 and GW190412, for which $\chi_{\rm eff} = 0.21^{+0.20}_{-0.10}$, $0.36^{+0.21}_{-0.25}$ and $0.25^{+0.08}_{-0.11}$ respectively (Abbott et al., 2020b). These indicate that at least of the members of each binary was spinning before the merger event and that this member had $\chi_{\rm eff} > 0$. GW170104 has effective spin $\chi_{\rm eff} = -0.12^{+0.21}_{-0.30}$, centered on a negative value, but also compatible with zero within uncertainty. The others are consistent with zero (Abbott et al., 2020b). The small values of $\chi_{\rm eff}$ can result from small BH spins S. If the intrinsic spins are almost zero for most BHs in binaries, the current and future effective spin measurements would not give strong constraints on the formation models of BH binaries. However, if the intrinsic spins are large for a significant fraction of BHs, effective spins could reveal their origins.

BHs in isolated field binaries are expected to be preferentially aligned with the orbital angular momentum. Although natal kicks (e.g. anisotropic SN explosions or neutrino

emission) can induce misalignment (Wysocki et al., 2018), significant misalignment would disrupt the binaries, suppressing GW merger events. It would be difficult for the isolated binary models to produce a significant fraction of mergers with large misalignment $\chi_{\rm eff} < 0$. A non-vanishing fraction of high positive $\chi_{\rm eff}$ is predicted in this class of models. If such events are not detected with the coming LIGO/Virgo observations, it would be unlikely that the observed BH mergers formed via field binaries (Hotokezaka & Piran, 2017b)

BHs in dynamically formed binaries in dense stellar environments are expected to have their spins distributed isotropically. The $\chi_{\rm eff}$ distribution is expected to be symmetric about zero, and it can be extended to high negative (or positive) $\chi_{\rm eff}$ if the intrinsic spin S is large. Considering GW151226, GW170729 and GW190412 with $\chi_{\rm eff} > 0$ and no definitive systems with $\chi_{\rm eff} < 0$, the current sample is very weakly asymmetric. Analysis in (Farr et al., 2018) suggested that around 10 additional detections, in addition to those reported in the first operating run, were expected to be sufficient to distinguish between a pure aligned or isotropic population. Recently Zevin et al. (2020) used the extended catalogue of events GWTC2 (Abbott et al., 2020b) and several different formation channels to attempt to infer the origin of merging BH binaries. A key result in this work was that a combination of channels is preferred by the analysis, and that the detections by LIGO/VIRGO are likely an almost equal mix of isolated field binaries and dynamically formed binaries. It was also found low intrinsic BH-spins are preferred. Similarly, in Garcia-Bellido et al. (2020) it was found that, when considering different spin-orientation scenarios (flat, isotropic, spin-aligned and anti-aligned), which can be associated with different formation channels, the current detection catalogue favours BH spins which are low and isotropically oriented.

In the tidal encounter model described in this chapter, a significant fraction of mergers have large misalignment $\chi_{\rm eff} < 0$ especially if binaries with large reduction factors of the merger time are considered. The $\chi_{\rm eff}$ distribution is slightly asymmetric, but flat with minor enhancement at the high and low ends $\chi_{\rm eff} \sim \pm S$. If the intrinsic BH spins are rather small $S \sim 0.2 - 0.4$, the resultant distribution could be roughly consistent with the current sample.

4.5 Merger rate estimate

It is not trivial to estimate how frequently BH binaries merge due to the tidal encounter mechanism. Several processes are involved in the estimate, most of which are not well constrained by current observations (Miller et al., 2005). A rough estimate of the merger rate due to the tidal encounter channel can be written as

$$\mathcal{R} \approx n_g \cdot \mathcal{N} \cdot P, \tag{4.5}$$

where n_g is the number density of galaxies, $\mathcal{N}$ is the tidal encounter rate of BH binaries with a massive BH (events per yr per galaxy), P is the fraction of tidal encounters that produce survivors with $\tau_{gw} < 10^{10}$ years. It is assumed that the first galaxies formed about 10^{10} years ago, and they have had sufficient time to host and grow massive BHs. This is consistent with recent observations, which indicate quasars are known to exist when the Universe was less than a billion years old (Bañados et al., 2018). Since survivors merge many years after the tidal encounters, this estimate implicitly assumes that the merger rate reaches a steady state.

The fraction P depends on the semi-major axis distribution of the pre-encounter circular binaries. As galactic centres are collisional environments, wide binaries can be disrupted by encounters with other objects. Equalizing the binding energy $Gm_1m_2/2a$ with the kinetic energy of an intruder $m_*\sigma^2/2$, it is found that $a = Gm_1m_2/m_*\sigma^2 \sim 140$ au for $m_1 = m_2 = 30M_\odot$, $m_* = 1M_\odot$ and the Milky-Way velocity dispersion $\sigma \sim 75$ km/s (Gebhardt et al., 2000). This is set as the maximum semi-major axis value. The minimum semi-major axis is set at $a_0 = 0.2$ au for which binaries with $m_1 = m_2 = 30M_\odot$ do not merge within 10^{10} yrs if they are not disturbed by the tidal encounter or other mechanisms. These binaries emit weak GWs at low frequencies $f_{gw} < 5.5 \times 10^{-6} (m/60M_\odot)^{1/2} (a/0.2 \text{ au})^{-3/2}$ Hz. Assuming a uniform a_0 distribution in logarithmic space, and using the a/a_0 and e distribution for $\alpha = 0$ obtained in section 4.3.2, the merger time τ_{gw} distribution of survivors is evaluated (the $\alpha = 1$ case also gives a very similar distribution). It is found that $\sim 50\%$ of BH binaries survive the tidal encounter and $\sim 6\%$ of the survivors have merger times of less than 10^{10}

years, yielding $P \sim 3 \times 10^{-2}$.

Although the tidal encounter rate is highly uncertain, $\mathcal{N} = 10^{-6}$ /yr/galaxy is adopted as a fiducial value. Stars are tidally disrupted by a massive BH with a rate of $10^{-5} - 10^{-4}$/yr/galaxy (Komossa, 2015). In the Milky Way, hypervelocity stars and the S-star cluster imply a similar rate of $10^{-5} - 10^{-3}$/yr/galaxy for the disruption of stellar binaries (Bromley et al., 2012). Simulations of galactic dynamics indicate that a density cusp forms around MBHs, where the concentration of high-mass objects increases. Population synthesis predictions also suggests that the fraction of BHs and NSs present in these regions is enhanced with respect to the field. In particular, using the simple formalism presented in Rasskazov & Kocsis (2019), it can be shown that the fractions of BHs in the entire Milky Way and nuclear star cluster are $\sim 0.13\%$ and $\sim 0.23\%$, respectively (Licquia & Newman, 2013). In addition, it is expected that dynamical friction will drive BHs formed in the outer regions towards the centre, further increasing their number (Löckmann et al., 2010; Petrovich & Antonini, 2017). Recent numerical studies have shown that this effect can increase their number by up to a factor of several (Rasskazov & Kocsis, 2019). These results are supported by recent observations of quiescent X-ray binaries in the Milky Way galactic centre, indicative of a large population of BHs and BH binaries in the galactic centre (Hailey et al., 2018). Hence the tidal encounter rate of compact binaries to be smaller than that inferred from HVS observations for stellar binaries by a factor of $\sim 10^2$.

In the early Universe, the number density of galaxies was higher, but most of these galaxies were relatively small and faint, with masses similar to those of the satellite galaxies surrounding the Milky Way (e.g. Conselice et al. 2016). Assuming the galaxy number density $n_g \sim 0.02$ Mpc^{-3} (Conselice et al., 2005; Hoang et al., 2018), then

$$\mathcal{R} \approx 0.6 \text{ Gpc}^{-3}\text{yr}^{-1}. \tag{4.6}$$

This is much smaller than the BH merger rates inferred by GW observations $15.3 - 38.8$ Gpc^{-3}yr^{-1} (Abbott et al., 2020b). The tidal encounter mechanism is unlikely to be the dominant formation channel of BH mergers. However, the current and near-future

GW observatories are expected to detect an enormous number of BH mergers. A small fraction of them might have experienced the tidal encounter with a massive BH. The merger times of hard binaries (originally $\tau_{gw} \ll 10^{10}$ years) can be further shortened by this mechanism. If binaries merge in the vicinity of massive BHs, GW lensing echoes might be produced (Kocsis, 2013).

4.6 Discussion and conclusions

In this chapter the first systematic study of how the tidal encounter with a massive BH affects the properties of BH-BH binaries (e.g. GW merger times and effective spins) is presented. Since the binary members were treated as point particles, the new formation mechanism of GW mergers also can be discussed with other compact stellar mergers such as NS-BH and NS-NS mergers.

BH binaries can survive the tidal encounter even in the deep limit $D \ll 1$. Although deep encounter survivors are counter-intuitive, binaries are actually disrupted, and the binary members separate when they deeply penetrate the tidal sphere of the massive BH. However, they approach each other after the periastron passage and a small fraction of them (12% for $D \ll 1$) can form binaries again even in the deep penetration cases (Sari et al., 2010; Brown et al., 2018).

Assuming simple D distribution models (i.e. an uniform or linear distribution for $0 < D < 2.1$), it was shown that about 50% of injected binaries can survive the tidal encounter, and the GW merger times of the survivors can be shorter by many order of magnitudes than that of pre-encounter binaries. About 10% (1%) of the survivors have GW merger times shorter by a factor of > 100 ($> 10^5$) than that of the pre-encounter binaries. Assuming that BH spins are aligned with the binary angular momentum before the tidal encounter, it is also shown that survivors can have large negative effective spins. This is because the tidal force rotates the orientation of the binaries, and the orientation flips to the opposite direction in some cases. In particular, the $\chi_{\rm eff}$ distribution of survivors with large reduction factors of the merger time is asymmetric,

but rather flat, and a significant fraction has negative effective spin.

Since BH spins are only weakly constrained by observations (and observations are generally consistent with equal-mass mergers), for the effective spin calculation equal binary member masses $m_1 = m_2$ and intrinsic spins $S = |\mathbf{S}_1| = |\mathbf{S}_2|$ were assumed. As the BH spins are constant in the tidal encounter model, it is straightforward to examine other possibilities. For example, in another equal-mass case with $|S_1| = S,\ |S_2| = 0$ (e.g.), the effective spins $\chi_{\rm eff}$ of the survivors are maximally $S/2$ instead of S. Since the directions of the BH spins are assumed to be independent and random when the effective spins are evaluated for the uniform and normal distributions of BH spins, the effective spin distribution should be identical to those shown in figure 4.7 if the x-axis is rescaled (i.e. $\chi_{\rm eff}$ should take a value between -0.5 and 0.5, and all the distributions peak around $\chi_{\rm eff}/S \sim 0.5$).

While the discussion is centred on the tidal encounter survivors, a large fraction of BH binaries should break up at the encounter. In such cases, one of the binary members should be ejected as a hyper-velocity BH and the other is captured in a highly eccentric orbit around the massive BH. This is one of possible channels to produce extreme mass ratio inspirals (Miller et al., 2005; Chen & Han, 2018), which are promising GW sources for the LISA mission (Babak et al., 2017).

Simulations presented in this chapter show that the GW merger time can be reduced even in shallow encounters with $D > 2.1$. However, the reduction effect becomes insignificant quickly for larger values of D (e.g. for $D = 2.5$, GW merger times are reduced by a factor of > 10 (> 50) for only 10% (1%) of cases, while for $D = 3$ more than 99% of the post-encounter binaries have $\tau_{gw,out}/\tau_{gw,in} \geq 0.8$). For the range $0 < D < 3$, the survivor fraction is found to be $\sim 66\%$. The main result of section 4.3.2 is modified by a factor of 2: $\sim 5\%$ ($\sim 0.5\%$) of the survivors have the merger times reduced by a factor of > 100 ($> 10^5$). Although this may modify the merger rate estimated above, the uncertainty in the tidal encounter rate is much larger.

Extreme-mass-ratio bursts (EMRBs) are a prime source of GWs for the future space-based interferometer LISA, and could possibly provide constraints for the very uncertain

tidal encounter rate (Turner 1977; Rubbo et al. 2006; Berry & Gair 2013). They are produced when a binary, which can be treated as a point particle at the lowest order of approximation, passes by a massive BH. The GW signal will have a burst-like behaviour, roughly characterized by an amplitude $h_b \sim GMm/c^4 r_p d$ and a duration $\Delta T \sim 1/f_b \sim \sqrt{r_p^3/GM}$ (e.g. Kobayashi et al. 2004). Expressing the periastron distance r_p in terms of the GW frequency f_B, then

$$h_B \sim 10^{-21} \left(\frac{M}{4\times 10^6 M_\odot}\right)^{2/3} \left(\frac{m}{30 M_\odot}\right) \left(\frac{f_B}{10^{-3}\text{Hz}}\right)^{2/3} \left(\frac{d}{10^2\text{Mpc}}\right)^{-1}. \quad (4.7)$$

LISA is expected to be able to detect EMRBs from MBHs out to ~ 100 Mpc (Berry & Gair, 2012; Moore et al., 2015).

If the periastron distance and tidal separation are comparable ($r_p \sim r_t$),the pre-encounter circular binary emits GWs at frequency f_b similar to the EMRB frequency f_B, but with an amplitude smaller by a factor of $\sim (M/m)^{2/3}$. Since the signal-to-noise ratio can be enhanced by integrating the periodic signal, the effective amplitude of the GWs from the binary would be $\sim \sqrt{N}(M/m)^{-2/3} h_B$, where $N_c = f_b \Delta T_{obs}$ is the number of cycles radiated during an observation period ΔT_{obs}. In order to make the effective amplitude comparable to that of the EMRB, a very long observational run is needed with $\Delta T_{obs} \sim f_b^{-1}(M/m)^{4/3} \sim 200$ yr for $M = 4\times 10^6 M_\odot$, $m = 30 M_\odot$ and $f_b = 10^{-3}$ Hz. For a more realistic observational period $\Delta T = 1 - 5$ yr, the effective amplitude would be smaller by one order of magnitude than the EMRB's amplitude. Therefore, EMRBs would be the dominant GW signal in the tidal encounter event, and they could indicate how frequently compact objects pass by MBHs. However, it would be difficult to distinguish binary encounters from single object encounter events.

The Newtonian formulation breaks down if the periastron is close to the event horizon scale R_g of the central massive BH or equivalently if $D \lesssim (m/M)^{1/3} R_g/a \sim 2\times 10^{-3}(a/1au)^{-1}(m/60M_\odot)^{1/3}(M/4\times 10^6 M_\odot)^{2/3}$. Relativistic corrections might become important if the encounter is very deep or if the initial binary separation is much smaller than $1\ au$. However, in the latter case, binaries have short GW merger times even before the tidal encounter, and binary hardening processes might not be required to

produce BH mergers.

Chapter 5

The tidal encounter and eccentric binary populations

The LIGO/VIRGO observations have shed light on the previously unknown population of BH binaries (e.g. Abbott et al. 2020b). However, the overall statistical properties of these systems are still unknown. As was discussed in previous chapters, more observations are necessary to characterize their properties.

While there is a great deal of uncertainty with regard to the properties of BH binaries, it is a reasonable assumption that these systems will preserve some of the properties of their progenitor stars. In particular, it can be expected that their dynamical properties are determined by their environment. Knowledge obtained from electromagnetic observations of stars can therefore be used to characterize the properties of different BH merger formation channels. One of such properties is the distribution of eccentricities of black hole binaries. There are examples in the literature of theoretical models which attempt to shed light on the BH binary eccentricity distribution (e.g Kowalska et al. 2011). However, there is still insufficient observational data to determine the validity of these models. In contrast, this distribution has been characterized for different populations of stellar binaries, including those in the field and in collisional environments (such as globular clusters).

In this chapter the effect of non-zero initial eccentricity on the tidal encounter process is characterized. Following this, three eccentricity distributions are considered, corresponding to different astrophysical origins of the BH binaries. By using Monte Carlo simulations the merger fraction enhancement is computed for a population which, without other intervening processes, would not coalesce within a Hubble time. As in chapter 4, observables of interest such as the post-encounter effective spin and eccentricity distributions are obtained.

5.1 The effect of eccentricity on the dynamics of the tidal encounter

As in chapter 4 compact binaries with component masses $m_1,\ m_2$ such that $m = m_1 + m_2$ are considered. The binary COM approaches a massive black hole (MBH) of mass M on a parabolic trajectory. To study the evolution of these systems the restricted three-body formalism is used (Sari et al., 2010; Brown et al., 2018).

The separation of the members in an eccentric binary depends on time, and is given by (Bate et al., 1971; Landau & Lifshitz, 1980)

$$d(t) = \frac{a(1-e^2)}{1+e\cos\phi(t)}, \tag{5.1}$$

where a is the semi-major axis (sma) and ϕ the binary phase. As follows from eq. 5.1, binary separation varies between $a(1+e)$ at apoapsis and $a(1-e)$ at periapsis during its orbit. In contrast to circular binaries, for which the tidal radius r_t and D are constant, in the eccentric case these parameters are effectively time-dependent. The system will be more susceptible to disruption or deformation at periapsis, where it spends the majority of its orbital time. In this case it has a larger effective tidal radius, hence the parabolic orbit penetrates deeper into it.

5.1.1 Initial conditions

In chapter 4 circular binaries undergoing tidal encounters were characterized by D, the orientation of their orbital plane (specified by two angles $\theta,\ \varphi$), and the binary phase at periastron ϕ. The binary orientations are sampled from uniform distributions, accounting for symmetry considerations, as in chapter 4. For eccentric binaries the orbital velocity is phase-dependent. Therefore, it is sampled from a distribution law proportional to the inverse of the orbital velocity:

$$\frac{dn(\phi)}{d\phi} \propto \frac{1}{(1+e_0\cos\phi)^2}, \tag{5.2}$$

where e_0 is the initial eccentricity, and $\phi \in [0, 2\pi]$. The orientation of the binary semi-major axis in the orbital plane must also be selected, specified by an angle η. It is sampled from a uniform distribution in the range $[0, \pi]$ (Brown et al., 2018).

5.1.2 The effect of eccentricity on the survival rate

In this section we discuss how the statistical properties of tidal encounter survivors change if binaries are injected toward the massive BH with non-zero eccentricity $e_0 \neq 0$. Monte Carlo simulations are performed for different initial eccentricities $e_0 \in \{0, 0.1, 0.5, 0.9\}$, and a uniformly distributed penetration factor D, where D is still defined as $D = r_p/r_t = r_p/[(M/m)^{1/3}a]]$. For each e_0 value, 1.5×10^5 random realizations of the set $\{D,\ \theta,\ \varphi,\ \phi,\ \eta\}$ were sampled.

The probability of an eccentric binary surviving the encounter is shown as a function of D in figure 5.1 (averaged over the other system parameters). No circular binaries are disrupted for $D > 2.1$ (Brown et al., 2018). However, in the eccentric case binaries are disrupted for much shallower encounters. This is due to eccentric binaries spending a large fraction of their orbital time close to periapsis, and hence experiencing an effectively smaller D-parameter. Consequently, the maximum penetration factor D_{max} for which there are tidal disruptions depends on e_0. For moderate eccentricity (in the figure $e_0 \leq 0.5$), it is also found the survival probability curves are insensitive to D

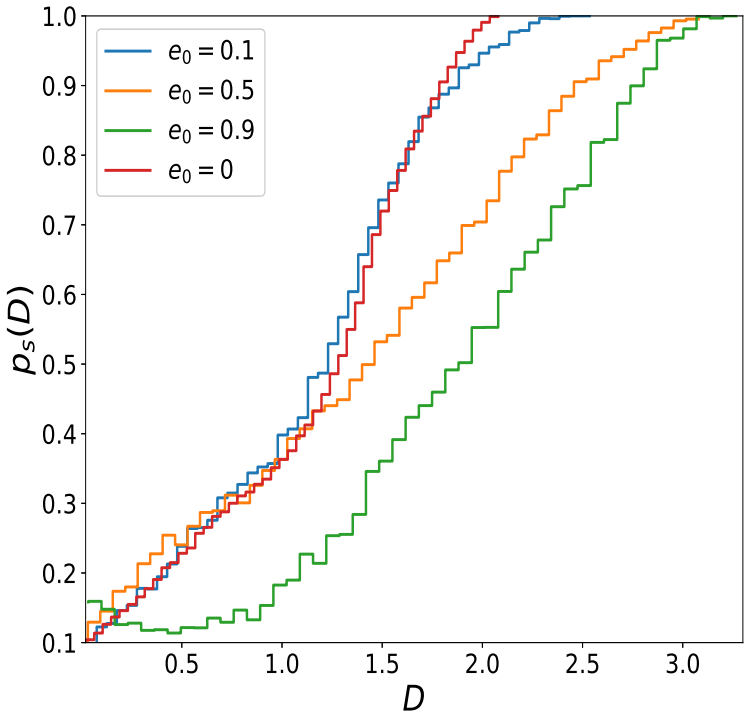

Figure 5.1: Probability of a binary surviving the encounter, as a function of D. The distributions were obtained by Monte Carlo sampling with constant e_0. The solid blue, orange and green lines are for $e_0 = 0.1, 0.5$ and 0.9 respectively. The initially circular case $e_0 = 0$ is shown for comparison (solid red line). The distributions are integrated over all binary parameters $\{\theta,\ \varphi,\ \phi,\ \eta\}$. The binary angular momentum and semi-major axis orientations were sampled from uniform distributions. The binary phase was sampled according to equation 5.2.

(< 1). For large eccentricity, the curves separate. For $e_0 = 0.9$, the effective D of the encounter varies by as much as ~ 0.75. This leads to deep tidal sphere penetrations even for orbits which would be extremely shallow in the circular case. The survival probability plateaus for small D, as in the circular case. This is consistent with results shown in Sari et al. (2010) and Brown et al. (2018), which show that the disruption probability becomes constant for very deep penetrations.

5.1.3 Orbital properties of survivors

Following the discussion above, in this section the maximum penetration factor D is set to $D_{max} = 2.5,\ 3.1$ and 3.3 for $e_0 = 0.1,\ 0.5$ and 0.9 respectively (at these values the survival probability becomes unity, as is illustrated in figure 5.1).

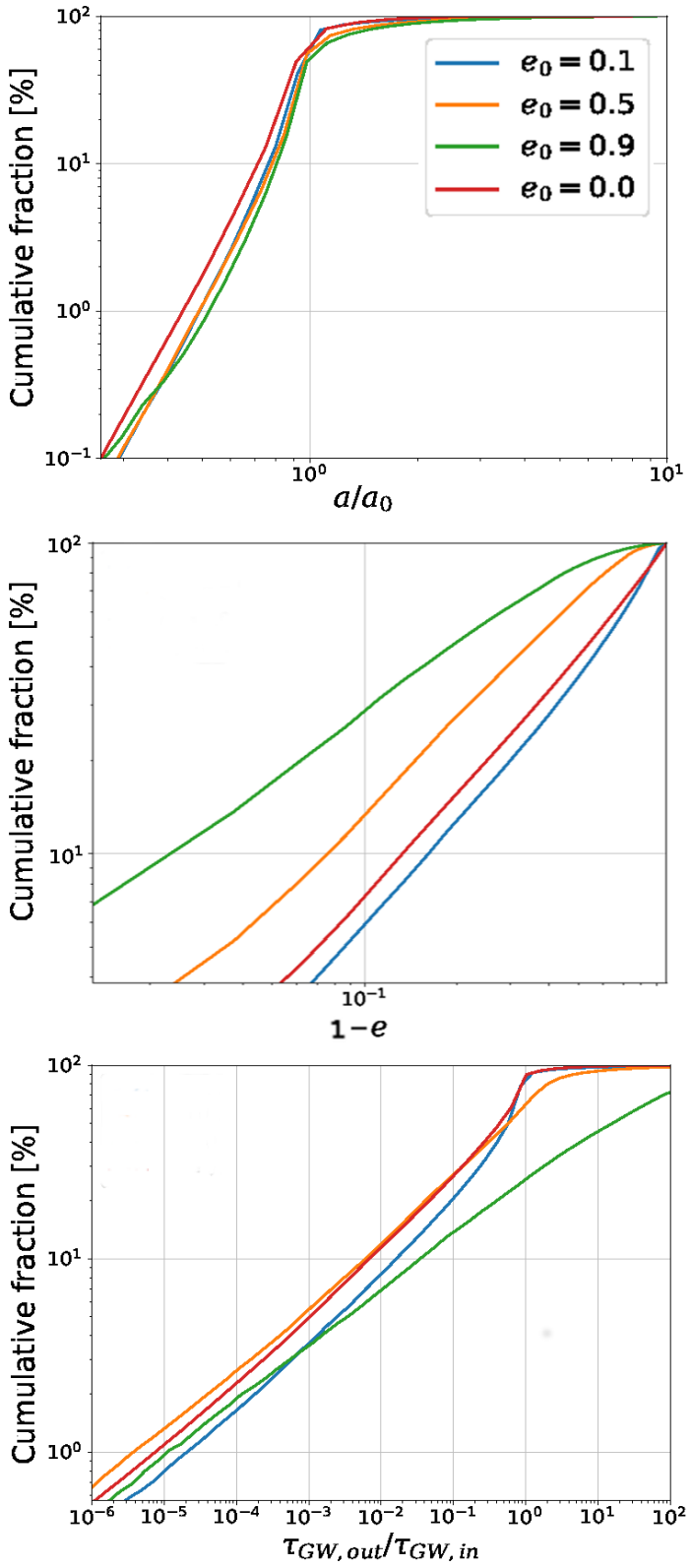

Figure 5.2: Distributions of the semi-major axes a (top panel), eccentricity differences $1 - e$ (middle panel) and GW merger times $\tau_{gw,out}$ (bottom panel) of the survivors. The semi-major axis and GW merger times are given in units of the pre-encounter values a_0 and $\tau_{gw,in}$. The distributions are obtained from the Monte Carlo sampling with fixed $e_0 = 0.1,\ 0.5$ and 0.9 (blue, orange and green lines respectively), and with uniformly distributed penetration factors D, and the binary orientation and semi-major axis orientation as in figure 5.1.

e_0	$e > e_0$	$e > 0.9$	$\langle e \rangle$
0	100%	6%	0.44
0.1	91%	5%	0.42
0.5	65%	12%	0.61
0.9	26%	26%	0.72

Table 5.1: Summary of the main features of the eccentricity distributions shown in the bottom panel of figure 5.2.

Figure 5.2 shows the post-encounter distributions of the survivor semi-major axes (top panel), eccentricities (middle panel) and GW merger time fractional change (bottom panel) for initially eccentric binaries. The fraction of binaries with reduced semi-major axis after the encounter $a < a_0$ slightly decreases, from $\sim 60\%$ for $e_0 = 0$ to $\sim 50\%$ for $e_0 = 0.9$. Similarly, the fraction of binaries for which $a/a_0 \leq 2$ varies between 2.3% in the circular case to around 1% for $e_0 = 0.9$.

We summarize in table 5.1 how the eccentricity changes at the tidal encounter. In contrast with the circular case, for $e_0 \neq 0$ the binaries can become more eccentric or can be circularized after the encounter. For moderate e_0 the binaries generally become more eccentric, and the mean eccentricity of the distribution $\langle e \rangle$ increases. For the highly eccentric case $e_0 = 0.9$ it is found that $\langle e \rangle < e_0$, and in general the tidal encounter reduces the eccentricity of the survivors.

In chapter 4 it is found for circular binaries that in 10% (1%) of cases τ_{GW} is reduced by a factor of 10^2 (10^5) or more. The distributions of reduction factors for the eccentric cases are shown in the bottom panel of figure 5.2. The reduction factors are similar to the circular case. The greatest reduction is found for $e_0 = 0.5$, for which τ_{GW} is a factor of 10^2 (10^5) or more smaller after the encounter in 12% (1.3%) of cases. In contrast to the circular case, we find that for initially eccentric binaries the post-encounter distributions present significant fractions of binaries with extended merger time (for $e_0 = 0.9$, of up to 75%). This is due to the large fraction of systems which become less eccentric and are stretched after the tidal encounter.

It is found that allowing for $e_0 \neq 0$ increases the fraction of binaries with post-encounter $\chi_{\rm eff} < 0$ significantly. For initially circular binaries this is the case in $\sim 7\%$ of cases.

In comparison, this fraction increases to $\sim 12\%$ for $e_0 = 0.5$, and to $\sim 35\%$ for $e_0 = 0.9$. This is shown in figure 5.3. As the eccentric binaries spend larger fractions of their orbital period close to periapsis, when considering the tidal torque described by equation 3.16 they can present extended lever arms, which may facilitate the rotation of the orbital plane by the tidal force of the MBH.

5.2 Full numerical study

5.2.1 Monte Carlo sample

In this section Monte Carlo simulations are used to characterize how different initial eccentricity distributions modify the properties of the surviving population of binaries.

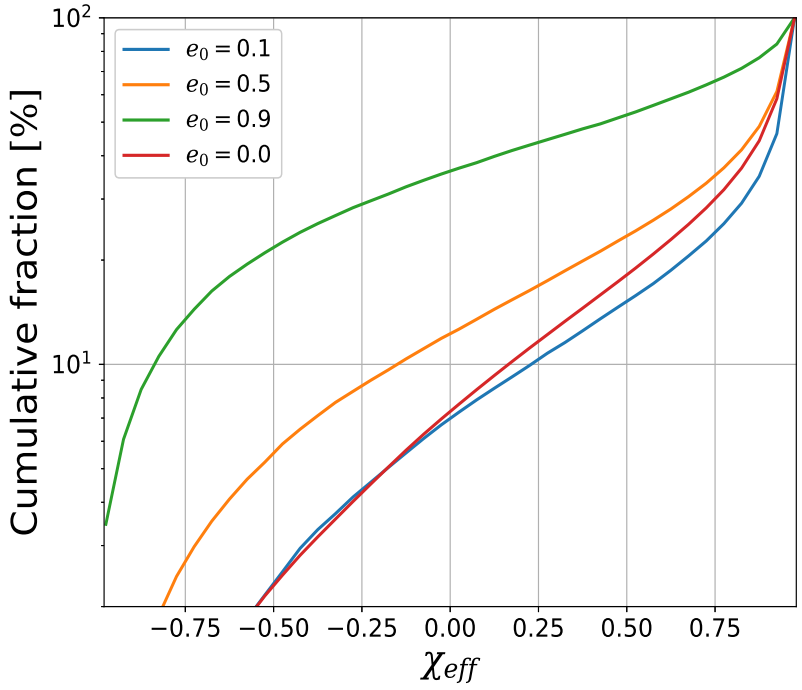

Figure 5.3: Post-encounter $\chi_{\rm eff}$-distributions for initially eccentric binaries. In general, it is found that allowing for $e_0 \neq 0$ increases the fraction of binaries with $\chi_{\rm eff} < 0$ after the encounter, i.e. more binaries have their orbital planes flipped. The solid blue, orange and green curves are for $e_0 = 0.1,\ 0.5$ and 0.9 respectively. The circular case (solid red line) is shown for comparison. The binary parameters were sampled as in figures 5.1 and 5.2

Three pre-encounter, power law eccentricity distributions are considered,

$$dn(e_0) \propto e_0^{\alpha} de_0, \tag{5.3}$$

for $0 < e_0 \leq 0.95$, which are representative of different astrophysical scenarios:

- A uniform distribution or $\alpha = 0$ (distribution 1), compatible with observations of field binaries (Raghavan et al., 2010). These can move towards the galactic centre due to their proper motions or scattered into the region by the stochastic potential of the stellar background. This distribution has a mean eccentricity $\langle e_0 \rangle = 0.475$ and a cumulative distribution function (CDF) such that CDF$(0.5) = 0.55\%$, i.e. $e_0 < 0.5$ for 55% of the sample.

- A thermal eccentricity distribution for which $\alpha = 1$ (distribution 2). Binaries in dense, collisional systems such as globular clusters can undergo sequence of effective two body encounters (the binary with another compact object) which after sufficient time drive the system to thermal equilibrium (Jeans, 1919). Globular clusters can migrate towards the galactic centre due to dynamical friction. They are also speculated to host intermediate mass black holes (Perera et al., 2017; Kızıltan et al., 2017), which could mediate tidal encounters. For this distribution $\langle e_0 \rangle = 0.63$ and CDF$(0.5) = 28\%$.

- A distribution compatible with observations of a limited sample massive O-stars in the field (Sana et al., 2012), for which $\alpha = -0.5$ (distribution 3). In this case $\langle e_0 \rangle = 0.32$ and CDF$(0.5) = 73\%$.

  This distribution was inferred by fitting orbital parameter distributions to observations of a sample of 71 O-type objects, out of which 40 were identified as binary systems. The masses of the sample are in the range $15M_{\odot} - 60M_{\odot}$. It must be noted the exponent in this case has rather large uncertainties (of the order of 50%, ± 0.22).

The initial eccentricity distributions e_0 are shown in the left panel of figure 5.4. The binary orientation, semi-major axis orientation in the orbital plane and phase are sampled

as discussed in the previous section. The penetration factor D is sampled from a uniform distribution in the range $0 < D < 3.3$ (by considering binaries with arbitrary orientations and phase at periastron, and it is found that for $e_0 \leq 0.95$ and $D > 3.3$ no binaries are disrupted). For each eccentricity distribution, over 4.5×10^5 random realizations of the set $\{D,\ \theta,\ \varphi,\ \phi,\ e_0,\ \eta\}$ were sampled. As in chapter 4, the binaries were injected on parabolic orbits at a distance $r_m = 10r_t$, and the equations of motion 3.9, 3.10 were integrated using a fourth-order Runge-Kutta scheme. The total survivor fractions for distributions $1,\ 2$ and 3 were found to be $\sim 58\%$, $\sim 57\%$ and $\sim 62\%$, respectively.

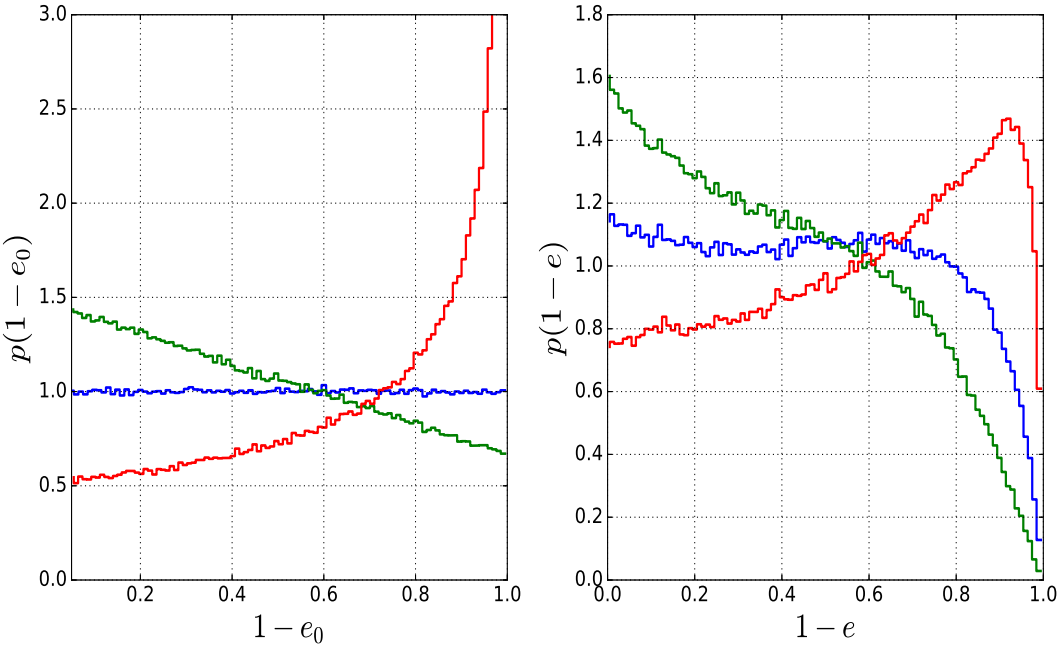

Figure 5.4: Left panel: initial eccentricity e_0-distributions for three different scenarios. Right panel: survivor eccentricity distributions. The eccentricities for field binary, globular cluster binaries eccentricities and field O-star binaries are shown in blue, green and red respectively.

The three sets of surviving binaries were analytically rescaled using the relations 3.8. The MBH mass was chosen to be $4 \times 10^6 M_\odot$ and the binary BH member masses $m_1 = m_2 = 30M_\odot$. The pre-encounter semi-major axes were sampled from uniform distribution in logarithmic space. The lower limit a_{min} of the distribution was set by demanding that pre-encounter merger time of the binaries satisfied $\tau_{gw,in} > 10^{10}$ yr. Using Peter's formula 2.12 and noting that in the sample $e_{0,max} = 0.95$, it was found that $a_{0,min} \approx 1.5$ au. The upper limit a_{max} was found by limiting the sample

to binaries which are narrow enough to survive a dynamical encounter with a typical galactic centre object. Considering the Milky Way galactic centre velocity dispersion $\sigma \sim 75km/s$ (Gebhardt et al., 2000), and considering a collision with a solar mass object, then for a_{max}

$$\frac{Gm_1m_2}{2a_{0,max}} = \frac{1}{2}M_{\odot}\sigma^2, \tag{5.4}$$

i.e. the binding energy of the widest binaries in the sample is equal to the kinetic energy of a typical colliding object in the region. From this relation it is found that $a_{max} \approx 140$ au. To ensure the convergence of the post-encounter distributions after rescaling, for each surviving binary three a_0 values were sampled.

5.2.2 Numerical results

Having fixed the binary member masses and pre-encounter semi-major axes, the GW merger time of the survivors can be obtained using equation 2.12. It is found that 0.98%, 1.34% and 0.65% of the survivors emerge from the encounter with $\tau_{gw} \leq 10^{10}$ yr. The distributions of merger times of these systems are shown in figure 5.5 (non-cumulative and cumulative distributions are shown in the left and right panels respectively). Around $\sim 0.5\%$ of these survivors merge less that 1000 years after the encounter, and $\sim 6\%$ within 10^6 years (a full orbital period around the sphere of influence of the MBH, with sma ~ 10 pc, is around 1.5×10^6 years). The discussion in the rest of this section is limited to the properties of these systems.

The fractions are smaller than those obtained in the case of initially circular binaries, $\sim 3\%$ (see chapter 4, section 4.5). This is in great part due to the selection of D_{max} and a_{max}. The value of D_{max} was set to the maximum value for which binaries with $e_0 = 0.95$ can be disrupted. Similarly, the a_{max} value was set to ensure that none of the sample would merge in less than 10^{10} years. Both D_{max} and a_{max} are larger than necessary for less eccentric binaries. Consequently these parameter choices reduce the number of systems susceptible to tidal deformation and which would merge within a

Hubble time after the tidal encounter. The fractions of systems with $\tau_{gw,out} < 10^{10}$ years obtained here can therefore be taken as lower limits. In principle, this would also reduce the merger rate estimate from chapter 4 by a factor of a few. However, any variation due to these parameter choices is still much smaller than that due to the highly uncertain tidal encounter rate. From these considerations it can be concluded that the merger rate estimate $\mathcal{R} \approx 0.6\,\mathrm{Gpc}^{-3}\mathrm{yr}^{-1}$ obtained for initially circular binaries is not significantly changed by considering families of eccentric binaries.

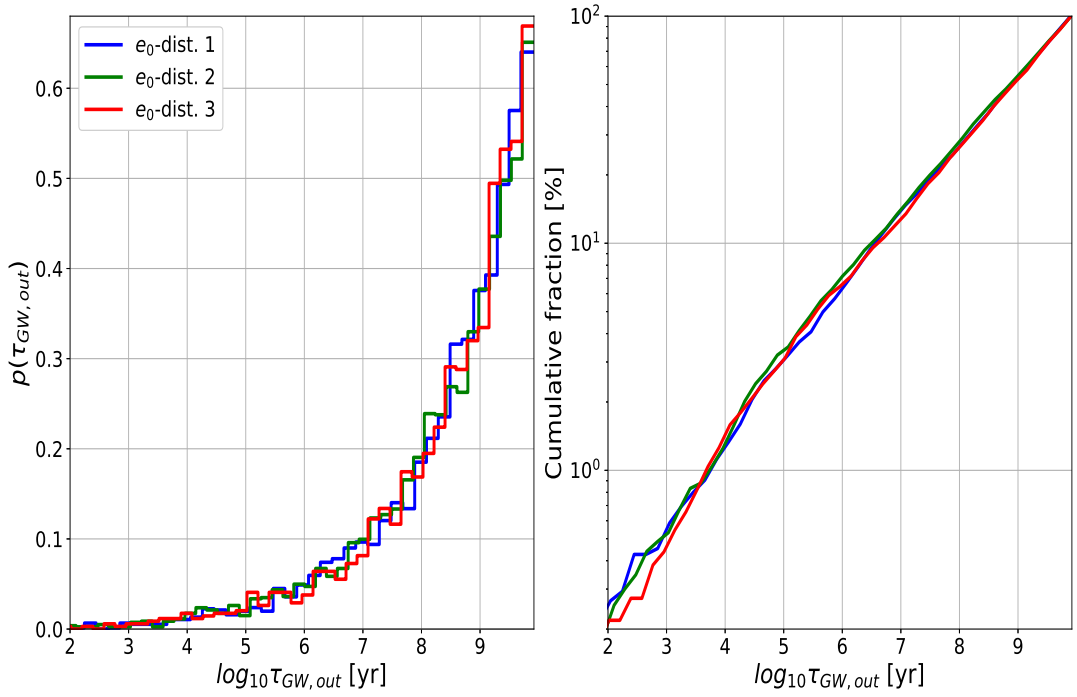

Figure 5.5: GW merger time distributions for surviving binaries with $\tau_{gw} < 10^{10}$ yr (left panel) and cumulative distribution (right panel). The merger times were obtained after analytically rescaling the tidal encounter survivor systems. The results for e_0-distributions 1, 2 and 3 are shown in blue, green and red respectively.

The post-encounter semi-major axis and eccentricity distributions, obtained after selecting binaries with $\tau_{gw,out} < 10^{10}$ yr, are shown in figure 5.6. For all three e_0-distributions, the post-encounter semi-major axis distributions (left panel) are narrow and centered on $a/a_0 \approx 1$, similarly to what was found for the initially circular case in chapter 4. The distributions are also virtually identical for all three sets of binaries. This indicates that typically the survivors are not significantly stretched or compressed by the tidal force of the MBH. However, the eccentricity distribution strongly favours very eccentric binaries with $e > 0.98$, and presents a sharp drop-off to almost 0 for

$e < 0.94$. This is the main factor leading to the short merger times of these systems. These eccentricity distributions can be compared with those for the full population of survivors, shown in the right panel of figure 5.4. In this plot it can be seen that while the eccentricity distributions are modified by the tidal encounter, the main features remain roughly the same (for example, whether more circular or more eccentric binaries are favored and the general trends of the distribution, except in the case of distribution 3 for $1-e > 0.9$ where there is a drop-off). In contrast, when only considering survivors with $\tau_{gw} < 10^{10}$ years, the distributions are essentially identical, independently of the initial conditions distribution. This feature also holds for a/a_0 and, as was shown above, the $\tau_{gw,out}$ distributions.

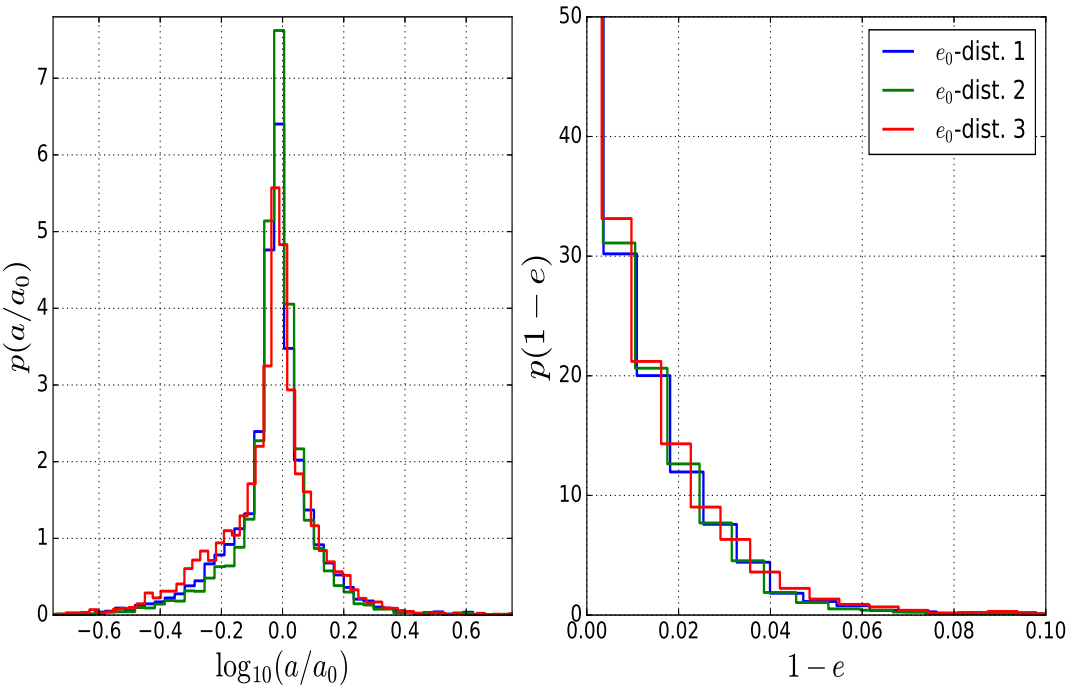

Figure 5.6: Post-encounter orbital properties of surviving binaries with $\tau_{gw} < 10^{10}$ yr. Left panel: semi-major axis distribution in logarithmic space. Right panel: eccentricity distribution. The color scheme is the same as in figure 5.5.

To obtain the effective spin $\chi_{\rm eff}$-distributions the procedure discussed in chapter 4 is followed. The BH spins $\mathbf{S}_{1,2}$ are assumed to be initially parallel to the binary angular momentum $\mathbf{L}_b$. The post-encounter effective spins were then obtained by using equation 4.2. Figure 5.7 shows the post-encounter $\chi_{\rm eff}$-distributions resulting from selecting the survivors with merger times $\tau_{GW,out} < 10^{10}$ years. As before, it is

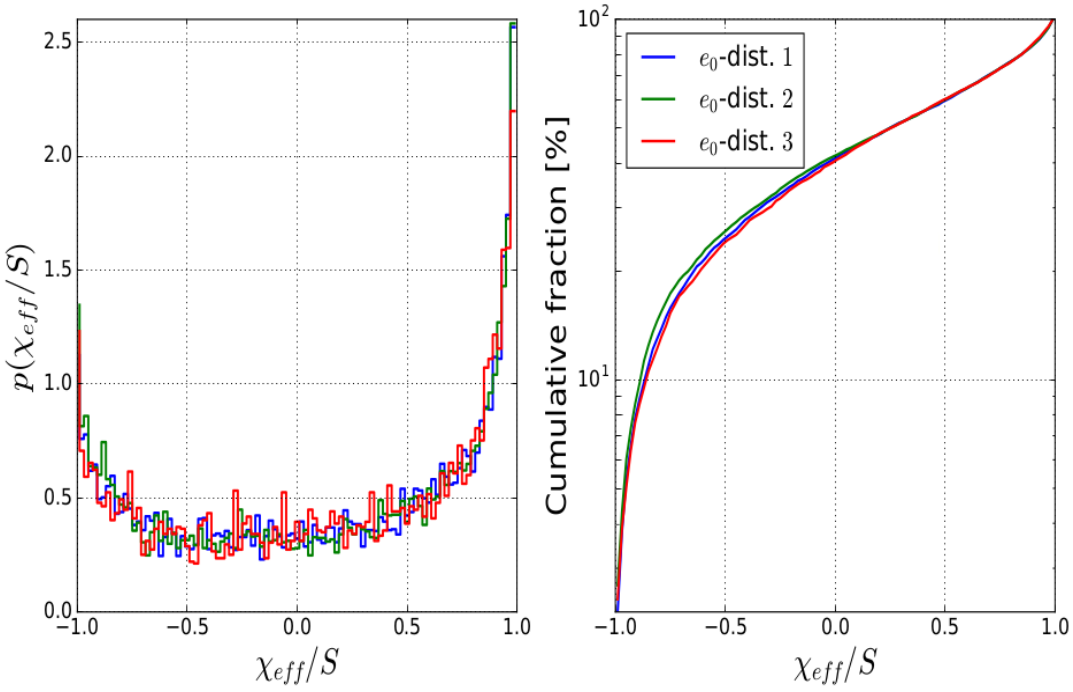

Figure 5.7: Post-encounter $\chi_{\rm eff}$ distribution obtained after selecting systems with $\tau_{gw} < 10^{10}$ yr. The effective spin is given in units of the initial BH spin S. The color scheme is the same as in figure 5.5.

found that these distributions are broadly independent of the e_0-distributions. In all three cases, the distribution is rather flat, presenting a slight preference for $\chi_{\rm eff} > 0.5$, peaking at $\chi_{\rm eff} = \pm 1$ and around 40% of the survivors emerging with negative effective spins. This result is similar to that for the circular case, discussed in chapter 4, where a similar distribution was obtained for survivors with $\tau_{gw,out}/\tau_{gw,in} \leq 10^{-5}$.

5.3 Discussion and conclusions

In spite of there being multiple physically plausible mechanisms for the formation of eccentric BH binaries, most LIGO/VIRGO detections reported to date are consistent with circular binaries, although recently GW190521 has been speculated to originate from an eccentric binary (Abbott et al., 2020a; Gayathri et al., 2020). This could be due to binary circularization by GW radiation before reaching the LIGO/VIRGO band, but also due to selection bias in favor of circular binaries (Huerta & Brown,

2013). The search algorithms currently used to find signals in LIGO/VIRGO data are ill-equipped for the detection of eccentric signals, while they are very well tuned for quasi-circular inspirals. GW coalescence signals are identified in the LIGO/VIRGO data by match-filtering with pre-calculated templates. These do not include eccentric inspirals, and the current library can only detect binaries with small eccentricities $e < 0.1$ (Abbott et al., 2019) Several approaches are being taken in order to detect eccentric BH binaries. Using the GW signal bursts associated with eccentric inspirals (Tiwari et al., 2016), power stacking of signals (Tai et al., 2014), or the application of deep learning techniques (George & Huerta, 2018) for real time detection are among the proposed methods to detect eccentric BH binaries. With the expanded ground-based detector network made up of LIGO's two detectors at design sensitivity (advLIGO), VIRGO and the up and coming Japanese detector KAGRA, it is expected that binary eccentricities will be detectable with uncertainty as low as $\Delta e \sim 10^{-3}$ (Gondán et al., 2018).

With the current library of BH coalescence observations constraints have been placed on properties such as the universal merger rate, or the mass distribution of BH binaries (e.g. Abbott et al. 2019). Other properties, such as the binary eccentricity distribution, remain unknown. GW radiation circularizes compact binaries. However, it is reasonable to assume that the BH binary population of the Universe will conserve and trace the properties of its progenitor stellar binary population. The eccentricity distribution of merging BH binaries should therefore be determined by the pre-inspiral evolution of the system and interactions with other objects in its environment. For example, if field binary scenarios dominate the merger rate then circular binaries will make the largest contribution to the set of observed mergers. In contrast, if dynamical formation channels dominate then binaries with different degrees of eccentricity at different frequency bands will be observed (i.e. very eccentric binaries in the LIGO and VIRGO band originating from fly-by captures (O'Leary et al., 2009), or very eccentric binaries in LISA band which have circularized by the time they reach the sensitivity range of ground-based facilities (Gondán et al., 2018)).

In this chapter the effect of non-zero initial eccentricity e_0 on the tidal encounter

process is characterized. As the binary member distance depends on the orbital phase for eccentric binaries, the depth of the encounter also depends on this parameter. This modifies the dynamics of the encounter, in particular the survival probability. Survivors can become more or less eccentric in this case, and a larger fraction of them are stretched by the tidal encounter. It is also found that a larger fraction of eccentric binaries can be flipped by the tidal encounter, resulting in $\chi_{\rm eff} < 0$.

The tidal encounter channel is then placed in astrophysical context by considering different origins for the BH binaries. Three eccentricity distributions were considered, obtained with electromagnetic observations of stellar binaries (for general field binaries and field O-star binaries) or theoretical predictions (i.e. for collisional environments such as globular clusters). The dimensionless tidal encounters were rescaled by considering binary member masses compatible with aLIGO/VIRGO observations and a physically plausible binary semi-major axis distribution, corresponding to binaries wide enough to have long pre-encounter GW merger times, but tight enough to be able to survive typical encounters in the NSC.

In all three cases it is found that a small, but non-negligible fraction of the survivors emerge from the encounter with $\tau_{gw} < 10^{10}$ years. These systems are very eccentric, with most having $e > 0.94$, and present a rather flat post-encounter effective spin distribution, with $\chi_{\rm eff} < 0$ in around 40% of cases. An interesting result is that the distributions of post-encounter properties of these systems are independent of the initial e_0-distribution. This indicates that the main factor determining the post-encounter population is the tidal interaction itself, not the initial conditions distribution (in chapter 4 it was found that the outcome was very weakly dependent on the initial D-distribution).

The fractions of binaries with post-encounter $\tau_{gw} < 10^{10}$ yr are very sensitive to the a_0-distribution. The limits were selected so that no binaries with $e \leq 0.95$ would merge within 10^{10} years before the encounter. This distribution significantly suppress the mergers of modestly eccentric binaries. Therefore, the results discussed in this chapter, and in particular the merger fractions, establish a lower-limit on the merger fraction enhancement due to the tidal encounter. The results of this chapter also indicate that the merger rate density is not significantly affected by considering initial eccentricity

distributions compatible with astrophysics scenarios such as populations field binaries or collisional systems. This result also applies to the fraction of survivors with negative effective spins $\chi_{\rm eff}$.

Part II

Electromagnetic counterparts to neutron star mergers

Chapter 6

Neutron star mergers and gamma ray bursts

The detection of a short gamma ray burst around 2 seconds after that of the neutron star merger GW170817 was a revolutionary moment in astronomy. For the first time gravitational waves and electromagnetic waves were to be combined to study a single event. This was an important step forward for multimessenger astronomy. The kilonova and afterglow of GW170817 was observed extensively across the EM spectrum by means of a unprecedented observational effort.

In this chapter[1]. a brief introduction to observational aspects of short gamma ray bursts and their afterglows is given in sections 6.1 and 6.2 respectively. After this the kilonova emission is discussed in section 6.3. In 6.4 the focus is then shifted to GW170817. The material in this chapter is in great part a summary of the extensive reviews of Piran (2005), Berger (2014), Kumar & Zhang (2015) and Metzger (2019); and references therein.

[1]The results in this chapter have been published as Fernández et al. (2021)

6.1 Short Gamma Ray Bursts

Gamma ray bursts (GRBs) are short and highly luminous pulses of gamma radiation which appear up to several times a night at random locations in the sky (Kumar & Zhang, 2015). They can be broadly classified into two groups, according to the distribution of T_{90}, defined as the interval during with 90% of the GRB energy is released. The two groups are short GRBs (sGRB), with a duration $T_{90} < 2s$, and long GRBs (lGRBs) with $T_{90} > 2s$. The former tend to have harder spectra. While this classification is widespread, it can also be misleading. The apparent duration of the burst can be detector-dependent. Different, more thorough criteria have been proposed which take into account the duration, luminosity, association with other transients such as supernovae (SNe) and host galaxy characteristics (Berger, 2014).

For as long as they last, GRBs rival the most luminous transients in the Universe, with an energy output similar to the combined emission of all other EM sources. The explosion giving rise to a GRB releases an isotropic equivalent energy of $\sim 10^{48} - 10^{54}$ ergs. However, as is discussed below, GRBs are almost certainly generated by a narrow, collimated jet, which reduces the required energy by several orders of magnitude.

There is ample evidence to support that lGRBs originate from the collapse of the core of a massive star. Evidence pointing to this includes their association with type Ic SNe, precise localization revealing that they are hosted by late-type galaxies, and their location within the hosts, which indicates their distribution traces star formation (Levan et al., 2016).

Several lines of evidence indicate that sGRBs can originate from compact mergers such as NS-NS or NS-BH mergers. The detection of the coincident NS-NS merger event GW170817 and sGRB170817 confirmed that at least a subgroup of sGRBs originate from these kind of compact mergers. Rapid accretion onto magnetars has also been proposed as a potential precursor of sGRBs (Piran, 2005; Lee & Ramirez-Ruiz, 2007; Kumar & Zhang, 2015).

In contrast to lGRBs, sGRBs have not been successfully associated with type Ic SNe. This discards the collapse of massive stars as a possible origin. sGRBs are found to happen in spiral and elliptical galaxies. As was discussed in chapter 2 and shown in equation 2.12, the GW coalescence time of a compact binary depends on the initial separation and masses of its members as $\tau_{gw} \sim a^4/m_1 m_2 m$ (Peters, 1964). Given a large enough separation, the delay between the formation and merger of a binary can vary by many orders of magnitude. Therefore, the coalescence which triggers the sGRB may occur while the galaxy still forms stars or long after it has consumed all its gas. In addition, afterglow observations (described in section 6.2 below) have allowed for the location of sGRBs to be obtained with enough precision to determine that these events often take place far from the star-forming regions of their host galaxies. This can be attributed to the natal kick a binary receives when one of its members collapses to a compact object. Some sGRBs (around 10%) are likely to originate in globular clusters from dynamically induced compact mergers (Berger, 2014).

In the compact merger picture, the central remnant can be surrounded by debris left behind from the event. In the case of a NS-NS binary, tidal forces can rip material from the surfaces of the binary components. In addition, the collision itself will also release a significant amount of debris. Similarly, in the case of a NS-BH merger the BH member can tidally disrupt the NS. Fast accretion onto the compact remnant acts as a central engine, powering a relativistic jet of particles which is launched into the debris. Mechanisms which could power this engine include neutrino-antineutrino annihilation (Rosswog et al., 2003; Lee & Ramirez-Ruiz, 2007) (however simulations indicate this process may not be sufficient to account for inferred GRB energies, e.g. Berger 2014), electromagnetic processes such as the Blandford-Znajek mechanism (Blandford & Znajek, 1977) or a magnetized accretion disk (Berger, 2014).

Once launched, the jet drills through the surrounding material (Granot et al., 2018; Gottlieb et al., 2020). The prompt GRB emission is generated by the dissipation of kinetic energy in this jet. The question of how the GRB emission is produced is still open. Internal shocks due to variability in the jet have been proposed as the underlying mechanism, e.g. Kobayashi et al. 1997; Daigne & Mochkovitch 1998).

Magnetic dissipation has also been proposed as an alternative mechanism (Zhang & Yan, 2010). The specific radiative process (or processes) responsible for the emission is also uncertain (suggested processes include synchrotron radiation or inverse-Compton) (Kumar & Zhang, 2015).

6.2 GRB afterglows

After the jet emerges from the debris, it collides with the circumburst medium (CBM), launching a forward and reverse shock[2]. The forward shock (blast wave) compresses, thermalizes and accelerates the initially cold CBM particles. Magnetic fields are believed to be generated via shock instabilities, which in turn leads to the production of synchrotron radiation as shock heated electrons girate around the field lines. This process persists on a scale of weeks to years, giving rise to a broadband, long-lasting emission known as the *GRB afterglow* (Meszaros & Rees, 1997; Sari et al., 1998). Similarly, the reverse shock propagates into and shocks the jet ejecta, giving rise to the *reverse shock emission* (Sari & Piran, 1995; Sari & Piran, 1999; Kobayashi, 2000; Sari & Piran, 1999; Lamb & Kobayashi, 2019). This emission is relevant very early on and peaks in the optical wavebands, giving rise to an *optical flash* (Sari & Piran, 1999; Sari et al., 1999; Kobayashi, 2000). Its polarization can be used to study the magnetic properties of the jet ejecta (for example, see Kobayashi 2017, 2019).

GRB afterglows were described, before their first detection, as a consequence of GRB shock propagation into the circumburst medium or CBM (e.g. Meszaros & Rees 1997), and have proven to be a key tool for GRB astrophysics. The launch of the space mission Swift (Gehrels & et al., 2004; Barthelmy et al., 2005) in 2004 made it possible for rapid follow-up to start, around 1 minute after the GRB trigger, in the X-ray (Burrows et al., 2005), optical and ultraviolet (UV) wavebands (Roming et al., 2005). Because of the relativistic beaming effect (see section 7.3 in the next chapter), if the jet axis is inclined with respect to the observer line of sight the observed emission is significantly

[2]In the simplest picture the jet propagates essentially unimpeded until it has swept up a CBM mass m such that $mc^2 = E/\Gamma_0^2$, where E is the explosion energy. At this point it begins to decelerate.

weakened. In some cases, if the jet is pointing away from the observer, the afterglow is detected without a GRB trigger. In this case it is known as an *orphan afterglow* (Huang et al., 2002; Levinson et al., 2002; Roming et al., 2005; Cenko et al., 2013).

6.2.1 Anatomy of a GRB afterglow

The details of afterglow lightcurves depend on the frequency ν, observing time T and inclination θ_{obs}, for a given jet. In terms of the inclination, if θ_J is the jet half-opening angle, then the lightcurve depends on whether the jet is observed on-axis ($\theta_{obs} < \theta_J$) or off-axis ($\theta_{obs} > \theta_J$). The flux density depends on the time-evolving synchrotron spectrum. This spectrum is well described by a broken power-law with segments connected by what are known as the break frequencies.

In the on-axis case the flux typically grows as $F_\nu \propto T^{1/2}$ until $\nu_m = \nu$ and then decays as $F_\nu \propto T^{3(p-1)/4}$ (Sari et al., 1998). Here ν_m is the critical frequency associated with the minimum electron energy, p the index of the electron Lorentz factor power-law distribution and Γ the bulk Lorentz factor of the shock (see the next chapter for details). The early rise is often observed for bright enough events in the optical and radio bands. However in X-ray the afterglow lightcurve is generally seen at a times when $\nu_X > \nu_m$ and this change in slope is not observed. Another change in slope in the lightcurves is expected when $\Gamma \approx 1/\theta_J$. Due to the relativistic beaming effect (e.g. Rybicki & Lightman 1985 and chapter 7, section 7.3) only a limited area of the jet is visible, with angular scale $\theta \sim 1/\Gamma$, and the observed flux is the same as in the case of a spherical explosion. This region grows as the jet decelerates until the entire system is visible to the observer. At this point the collimated nature of the jet becomes apparent, leading to a steeper decay than that expected in the spherical case. This change in slope is known as the *jet break*. The break is expected to be achromatic and to be observed at the same time across different wavebands. After this, analytic estimates indicate that the flux decays as $F_\nu \propto t^{-p}$ (Rhoads, 1999; Sari et al., 1999). In practice the decay index may vary and is steeper due to deviations from the simple analytic models.

For a jet observed off-axis much of the frequency dependence is lost, except for the

normalization of the light curve. The flux F_ν initially rises, and as the jet decelerates, the relativistic beaming effect becomes less important and the jet core eventually becomes visible. After this the flux decreases and asymptotically approaches the decay expected in the collimated case $F_\nu \propto t^{-p}$ (Rhoads, 1999; Lamb & Kobayashi, 2017).

The data available for sGRB afterglows is significantly sparser than in the case of long GRBs due to the lower energetics of the jets and ambient densities, which leads to weaker emissions. Consequently the rate of observable on-axis sGRBs is expected to be low (Berger, 2014).

However, the features described here have been observed for several events, including among others GRB 160812B (Troja et al., 2019; Lamb et al., 2019), GRB111020A (Fong et al. (2012) and references therein) or GRB130603B (Fong et al., 2013).

GRB 111020A was detected on 20th October 2011 by the *Burst Alert Telescope* (*BAT*) on board of *Swift*, and consisted of an sGRB with duration $T_{90} = 0.40 \pm 0.09$ seconds. The Swift X-ray telescope, *Swift-XRT* began observations at $T = 72.6$ seconds after the trigger. *XMM-Newton* joined the observation effort at $T = 0.65$ days, and additional *Chandra* data was obtained at 2.9 and 10.1 days after the burst. In total, the X-ray afterglow was well sampled from around $T = 100$ s to $T = 10$ days. They key finding from the lightcurve was evidence of the jet break at $T \approx 2$ days, which implies a jet opening angle of $\theta_J \approx 3^\circ - 8^\circ$. No optical or UV sources were detected for this event (Fong et al., 2012).

Follow-up of sGRB 130603B led to the detection of optical and radio afterglows, in addition to the X-ray signal (Fong et al., 2013). The γ-ray pulse was detected by *BAT* on 3rd June 2013 and had $T_{90} = 0.18 \pm 0.02$ s. The X-ray afterglow was detected at $T = 59$ s by *XRT* and decayed below the observational threshold after 2 days. Optical observations began 2.7 hours after the trigger with ground-based facilities, and two *Hubble Space Telescope* (HST) epochs were also obtained. The radio follow-up with the *Jansky Very Large Array* (VLA) began at $T = 8.8$ hr and also detected a source with a consistent location with the X-ray and optical data. The jet break was detected at $T = 0.47$ days, and was clearest in the radio data as an inflection point

in the lightcurve (the observations were obtained at frequency $\nu = 6.7$ GHz $> \nu_m$ and therefore the radio lightcurve initially rises). It can also be observed as a change in decay index in the optical and X-ray data (see figure 2 in Fong et al. 2013). An opening angle of $4^\circ - 8^\circ$ was inferred from the break.

sGRB 160821B was discovered by *BAT* and *Fermi/GBM* independently on 21st August 2016. These facilities reported a γ-ray pulse duration of $\tau = 0.48 \pm 0.07$ s and $\tau \approx 1$ s respectively (both compatible with the standard sGRB classification). The afterglow of this event was detected in X-ray, optical, near infrared (NIR) and radio. The observations of this event revealed a more complicated behaviour which includes reverse shock emission, excess in the optical band due to kilonova emission (see section 6.3 below). The data found was compatible with a structured jet viewed slightly off-axis. A jet-break at $T = 3.5$ days, implying a jet core size of $\theta_c \approx 0.2$ rad (in a structured jet the energy depends on the angle with respect to the jet axis and the core contains most of the energy) (Troja et al., 2019; Lamb et al., 2019).

6.2.2 Radio imaging of afterglows

Since GRBs generally happen at cosmological distances, observations with conventional telescopes in the X-ray, optical/NIR and radio wavebands, while providing detailed lightcurves, are unable to provide detailed information about the spatial structure of the emitting region. By combining multiple telescopes or antennae (Jennison, 1958), Very Long Baseline Interferometry (VLBI) is capable of reconstructing this structure to produce spatially resolved images of the source (Cohen, 1973), in contrast to the effective point source which conventional telescopes observe.

This technique has been used most notably in the extreme case of the *Event Horizon Telescope (EHT)*, which used a global radio telescope network to image to central massive black hole in the local group galaxy M87 (Akiyama et al., 2019). Radio imaging has also been employed to study gas kinematics in AGN host galaxies (Molyneux et al., 2019) or star formation (Zhang et al., 2019). In the context of GRB astrophysics, VLBI imaging was most notably used to obtain radio images of the sGRB170817

afterglow in Mooley et al. (2018) and Ghirlanda et al. (2019) (see section 6.4 below).

As mentioned above, radio imaging can provide insight to the spatial structure of the emitting region of an afterglow. A direct application of this is determining whether an expanding radio source is due to isotropic or jet-like ejecta (e.g. Gill & Granot 2018). In general, if the source is a spherical shock the brightness-weighted centroid of the image is expected to remain at the explosion location. This also holds for a jet-like ejecta viewed on axis. However, if it is observed off-axis the centroid should move away from the origin in the imaging plane. As is shown in chapter 8, this can be used to constrain the viewing angle of the jet. The evolution of the image size can also be used to constrain the CBM density profile (e.g. Pihlstrom et al. 2007).

GRB 030329 was a lGRB detected in the pre-*Swift* era by the *High Energy Transient Explorer*-2 (*HETE-2*) on 29th March 2003. A peculiarity of this event was that it produced first radio afterglow bright enough for VLBI imaging to be successfully obtained (Taylor et al., 2004). In Pihlstrom et al. (2007) constraints were placed on the growth of the source size and the proper motion of the image centroid. These were found to present superluminal phases, i.e. with apparent velocity in the sky $\beta_{app} > 1$. The possibility of apparent superluminal motion was suggested by Rees (1966) for radio sources moving at suitable angles with respect to the observer's line of sight. The afterglow image was found to have grown in size of 0.176 mas at 217 days to 0.347 mas at 806 days, which for this system implies an expansion of 1.6 light years and a mean velocity of $\beta_{app} \approx 1$. Taking into account that the system is decelerating, this in turn implies $\beta_{app} > 1$ at earlier times (Taylor et al., 2005).

6.3 Neutron star mergers and the kilonova emission

When a NS-NS binary merges significant quantities of neutron-rich material is ejected from the system. There are two sources of this ejecta, known as *disk ejecta* and *dynamical ejecta* (Metzger, 2019).

Disk ejecta is made up of tidally disrupted material. When the binary members inspiral

tidal forces can disrupt the surface of the neutron stars. This material builds up on the equatorial plane of the binary, and forms an accretion disk around the central remnant of $\sim 0.01 - 0.3\ M_{\odot}$ (this estimate is sensitive to the neutron star equation of state and the binary member masses and spins). Winds in this disk lead to an isotropic expansion of the disk material (Metzger, 2019; Ascenzi et al., 2021) .

Dynamical ejecta is launched by two processes. When the neutron stars collide, on the contact interface between the members matter is compressed. Shocks generated in this process expel material along and around the polar axis of the binary. In addition, the material in spiral arms formed by tidal forces during the inspiral also results in dynamical ejecta which spreads outwards from the equatorial plane. Simulations indicate that this ejecta has mass in the range $\sim 10^{-4} - 10^{-2}\ M_{\odot}$ in the case of NS-NS mergers, and is launched at speeds of $\sim 0.1 - 0.3\ c$ (Fernández & Metzger, 2016).

As the different ejecta expand, heavy nuclei present in the progenitor objects, such as ^{56}Fe, are bombarded with neutrons. The resulting nuclei, which reside on the neutron-rich side of the nuclear stability valley, are unstable and subject to β-decay. If the characteristic time for neutron capture is shorter than that for decay this results in the synthesis of elements heavier than iron. This process is known as *rapid neutron capture* and its products as *r-process* elements (Burbidge et al., 1957; Lippuner & Roberts, 2015; Ascenzi et al., 2021).

The elements formed in the ejecta depend on the electron fraction Y_e. Assuming the neutron star material is uncharged, this is given by $Y_e = n_p/(n_p + n_n)$, where n_p and n_n are the number of protons and neutrons respectively (Burbidge et al., 1957). Dynamical ejecta is heated by shocks, which leads to pair production. Hence this component is relatively rich in electrons and have $Y_e \sim 0.05 - 0.4$. The disk ejecta has lower Y_e (Ascenzi et al., 2021). It must be noted that simulations show that the electron fractions are sensitive to the collapse time of the merger remnant and the NS equation of state (Metzger, 2019).

The dynamical ejecta, which has high Y_e, and consequently relatively small neutron fraction, forms elements with atomic masses A in the range $90 \geq A \geq 130$. In

particular, this ejecta does not produce lanthanides. The ejecta launched from the equatorial plane, with lower Y_e, can in principle form the entire range of r-process elements, including the lanthanides (Ascenzi et al., 2021) (these determine the opacity and hence colour of the emission, see below).

The radioactive decay heats the ejecta, powering an EM transient known as a *kilonova* or *macronova* (Metzger, 2019). The kilonova signal peaks at IR/optical wavelengths. The detailed properties of this emission, such as the peak time and colour depend on the elements formed in the ejecta (which determine the opacity) and the observing angle. If the observer is aligned with, or close to, the binary rotation axis, the kilonova emission is dominated by the dynamical ejecta. Simple models (e.g Metzger (2019)) predict the emission will peak around $T \sim 1$ day in the R and I bands. This is known as the blue kilonova. If the observer LOS is aligned close to the equatorial plane the emission is dominated by disk material, which is rich in lanthanides. The abundance of transition lines in the UV and optical suppresses the emission, delays the peak time and moves the peak frequency towards redder wavelengths. Hence this component is known as the red kilonova. In practice a mix of these components will be observed, depending on their relative velocities and the viewing angle (Ascenzi et al., 2021; Fernández & Metzger, 2016).

Kilonovae can be detected as a flux excess in the optical or near IR bands. The first detected kilonovae was associated with sGRB130603B. This event presented excess NIR flux, when compared to expectations from afterglow-only models, around 7 days (Tanvir et al., 2013) and 9 days (Berger et al., 2013). Therefore an additional source was needed to explain these observations. Modelling for this event showed the observations were compatible with an ejecta of $M_{ej} \sim 10^{-2} - 10^{-1}\ M_\odot$ with velocity $v_{ej} \sim 0.1 - 0.3c$. Similarly, an optical and IR excess was detected in the follow-up of sGRB160821 between 1 and 5 days. Modelling in this case showed that the excess is well explained by a wind-driven ejecta with mass $M_w = 10^{-2} M_\odot$ and a dynamical ejecta $M_{dyn} = 10^{-3} M_\odot$ with velocity $v_{ej} \sim 0.1 - 0.15c$ (Lamb et al., 2019).

6.4 The neutron star merger GW170817

On 17th August 2017, during their second operational run the aLIGO-aVirgo interferometer network detected a signal which was found to originate from a neutron star-neutron star merger. The total mass of the binary was found to be $M = 2.74^{+0.04}_{-0.01} M_{\odot}$ (Abbott et al., 2017c). This merger was the most precisely localized GW signal to date, constrained to originate from an area of 28 deg^2 in the sky, due to two factors. The first was the proximity of the event (the distance inferred from the GW signal was 40^{+8}_{-14} Mpc). The second was that aVIRGO did not detect the signal, which significantly limits the region of the sky where it could originate from.

The precise localization allowed for a rapid search for associated electromagnetic counterparts. A sGRB was detected by the space telescope *Fermi*, taking place 1.7 seconds after the binary coalescence (Abbott et al., 2017c). This event originated from the galaxy NGC4993 at a distance of $\sim$ 40 Mpc, compatible with the localization constraints of GW170817 (Valenti et al., 2017). The sGRB was uncharacteristically weak. This particular feature was explained by considering the GRB was seen off-axis at a large angle, and that the jet had to penetrate through a cocoon of ejecta surrounding the merging site (Kasliwal et al., 2017; Gottlieb et al., 2018). It must be noted that the sGRB was detected independently of the GW detection.

An EM transient, dubbed AT2017gfo, was detected around 11 hours after the merger in the optical, NIR and UV (Soares-Santos et al., 2017). This transient faded rapidly, peaking in the UV on the order of days and IR of a few hours (Abbott et al., 2017e; Troja et al., 2018). This emission was found to be compatible with a kilonova produced by an ejecta with mass $M_{ej} \sim 0.05 M_{\odot}$ moving at subrelativistic velocities $v_{ej} \sim 0.1c$ (Kasliwal et al., 2017; Cowperthwaite et al., 2017; Nicholl et al., 2017). The fast evolution of this transient and its spectral features were key to link AT2017gfo to a sGRB and discard the possibility of a long GRB originating from stellar collapse.

An extensive follow-up campaign ensued to obtain detailed observations of the event. The GRB afterglow was detected ~ 9 days later by in X-ray wavelengths by *Chandra* (Troja et al., 2017). A radio counterpart was detected 16 days post-merger by *VLA*

(Hallinan et al., 2017) and 110 days post-merger the optical component was found by *HST* (Lyman et al., 2018), among other facilities. The afterglow presented an initial rise roughly described by the power law $F_\nu(t) \propto t^{0.8}$ and after peaking at $T \sim 150$ days began to decay as $F_\nu \propto t^{-\omega}$, where $\omega \sim 2$ (Troja et al., 2019; Makhathini & et. al, 2020). The afterglow was still detectable in X-rays at $T \sim 1000$ days (Troja et al., 2020). The rise of the light curve is attributed to the afterglow having been observed off-axis and the jet structure (e.g Lyman et al. 2018; Troja et al. 2019; Lamb et al. 2019; Fong et al. 2019; Salafia et al. 2019; Lamb et al. 2019)

The extensive data set available for GW170817/AT2017gfo is unprecedented for a single event (Makhathini & et. al, 2020). However, in principle the afterglow lightcurve observations are compatible with several different physical origins, including different structured jet models and choked jet scenarios in which the jet is not successfully launched but instead heats up a (close to) isotropic cocoon of slow-moving ejecta (Mooley et al., 2018). VLBI images of the afterglow obtained at $T \approx 75$ days and $T \approx 230$ days were presented in Mooley et al. (2018), and an additional image at $T \approx 207$ days in Ghirlanda et al. (2019). The centroid of these images was found to present apparent superluminal motion, which is expected for anisotropic, jet-like ejecta (Gill & Granot, 2018; Mooley et al., 2018; Ghirlanda et al., 2019).

The combination of sGRB, kilonova, afterglow lightcurves and radio images allows for a complete picture of the event to be constructed: after the GW inspiral, material is ejected away from the central object. Rapid accretion onto the remnant powers a relativistic jet which is launched through this material, heating and inflating it, and forming a cocoon. The jet manages to drill through the cocoon, emerging and releasing a sGRB. The synthesis and subsequent radioactive decay of r-process elements gives rise to the kilonova emission, and the deceleration of the relativistic jet as it shocks the CBM gives rise to the afterglow, visible from radio to X-ray wavelengths.

Chapter 7

GRB afterglow physics

Simple semi-analytic models have been useful to explain the main features of GRB afterglows. In the simplest cases the dynamics is obtained by considering energy conservation, and the jet evolution is described by a broken power law. More sophisticated treatments can be used to better describe the transition between the relativistic and Newtonian phases of the evolution.

In this chapter the physics of GRB afterglows is reviewed. Details of the dynamics of jet expansion and radiation processes are discussed. Relativistic effects which also significantly affect the observational properties of the afterglows are discussed.

7.1 Dynamics of GRB jets

Relativistic explosion in a cold ISM

Consider a spherical shell, with energy E, mass $M = E/\Gamma_0 c^2$ expanding with an initial Lorentz factor Γ_0 into a cold and uniform circumburst medium (CBM) of particle density n. The shell decelerates when a significant fraction of the kinetic energy is given to the ambient material. If the shell expands up to a radius R, the CBM mass swept-up by the shell is $\sim 4\pi n R^3/3$. Since it is shock heated and expanding with Γ_0,

the shocked material carries an energy of $\sim 4\pi n R^3 \Gamma_0^2/3$.

Equalizing the shock energy with the shell energy, the deceleration radius R_d is given by

$$R_d \equiv \left(\frac{3E}{4\pi n m_p \Gamma_0^2 c^2}\right)^{1/3}, \quad \Gamma(R \leq R_{d)} = \Gamma_0. \tag{7.1}$$

The shocked ambient material forms a blast wave and approaches the Blandford-Mckee self-similar solution (Blandford & McKee, 1976). Conservation of energy leads to

$$E = \frac{4}{3}\pi m_p n \Gamma^2 c^2 R^3 \implies \Gamma(R > R_d) = \Gamma_0 \left(\frac{R}{R_d}\right)^{-3/2}, \tag{7.2}$$

Equation 7.2 holds while the shock is ultra-relativistic. As it decelerates, it leaves this regime to become trans-relativistic and at late times Newtonian (e.g Kobayashi et al. 1999), where the dynamics is described by the Sedov-Taylor solution (Taylor, 1950a,b).

To appropriately describe the evolution of the shock, and capture the transitions between the different regimes, conservation of the full stress-energy tensor must be considered. This approach was taken in Pe'er (2012), and for an adiabatic expansion leads to

$$\frac{d\Gamma}{dm} = -\frac{\hat{\gamma}(\Gamma^2 - 1) - (\hat{\gamma} - 1)\Gamma\beta^2}{M + m[2\hat{\gamma}\Gamma - (\hat{\gamma} - 1)(1 + \Gamma^{-2})]}, \tag{7.3}$$

where $\beta = \sqrt{1 - \Gamma^2}$ is the velocity of the shock in units of c and $\hat{\gamma}$ is the adiabatic index of the fluid. In the relativistic and Newtonian limits the adiabatic index of an ideal fluid is $\hat{\gamma} = 4/3$ and $\hat{\gamma} = 5/3$. When solving numerically solving equation 7.3 γ is obtained using the procedure detailed in Pe'er (2012).

Lateral spreading of GRB jets

Because of the relativistic beaming effect, the radiation from a jet can be described by a spherical model with an isotropic explosion energy E. The actual energy in the jet with a solid angle Ω is given by $(\Omega/4\pi)E$. This spherical model holds while

$\Gamma \gg 1/\theta_J$, where θ_J is the half opening angle of the jet, as the bulk of the system is causally disconnected from its edge. As the jet decelerates, information about pressure gradients, transported by sound waves, can reach the edges, forcing them to spread laterally. This is expected to occur around the *jet break*, when roughly $\Gamma \sim 1/\theta_j$ and the initially anisotropic jet evolves towards being isotropic (Granot, 2007; Granot & Piran, 2012).

The timescale on which the system approaches a spherical flow depends on the exact details of the spreading, which are still uncertain. In particular, it has been difficult to reconcile simple (semi-) analytic considerations (Panaitescu & Meszaros, 1999; Panaitescu & Kumar, 2000) with the results of numerical simulations (e.g. van Eerten & MacFadyen (2012)). The former predict in many cases very fast lateral spreading, with an exponential growth in the jet opening angle after deceleration (Granot, 2007). In contrast, hydrodynamics simulations indicate that the expansion is much slower, not becoming significant until the blastwave has become mildly relativistic (Lyutikov, 2012).

Consider a uniform jet (i.e. with constant energy per unit solid angle ϵ and initial Lorentz factor Γ_0 throughout) with sharp-edges at θ_j. This is known as a top-hat jet model. The simplest model of lateral expansion considers that the edges of the jet spread at the local sound speed c_s in the co-moving frame of the jet, so that the lateral size of the jet $R_\perp \approx R\theta_j$ $(\theta_j \ll 1)$ evolves with radius as

$$\frac{dR_\perp}{dR} \approx \theta_j + R\frac{d\theta_j}{dR} = \theta_j + c_s\frac{dt'}{dR}, \tag{7.4}$$

$$\frac{dR_\perp}{dR} \approx \theta_j + \frac{c_s}{c\Gamma}. \tag{7.5}$$

Combining 7.4 and 7.5 yields a simple expression for the evolution of θ_j,

$$\frac{d\theta_j}{dR} = \frac{c_s}{c\Gamma R} \implies \frac{d\theta_j}{dln\ R} \approx \frac{c_s}{c\Gamma} \sim \frac{1}{\Gamma}, \tag{7.6}$$

where the last step approximately holds when the fluid is relativistic and $c_s \sim c$. It

can be shown that this description leads to exponential growth of θ_j after $\Gamma > 1/\theta_j$ (Granot, 2007; Kumar & Granot, 2003a; Granot & Piran, 2012).

As was discussed in Granot & Piran (2012) a more sophisticated, relativistic model can be obtained by considering the shock jump conditions. In particular, the conditions imply that the local velocity of the material behind the shock is perpendicular at any point to the shock front (Landau & Lifshitz, 1987; Blandford & McKee, 1976; Granot & Piran, 2012).

The shape of the shock front can be parametrized by a smooth curve $\mathbf{r}(\xi)$, where ξ is an arbitrary parameter. Then a small change in position along $\mathbf{r}(\xi)$ can be expressed as

$$\Delta\mathbf{r} = \Delta r\hat{\mathbf{r}} + r\Delta\theta\hat{\boldsymbol{\theta}}, \tag{7.7}$$

where $\hat{\mathbf{r}},\ \hat{\theta}$ are unit vectors indicating the radial and polar angle directions. The tangent vector to this curve is defined as

$$\mathbf{T} \equiv \frac{dr}{d\xi}\hat{\mathbf{r}} + r\frac{d\theta}{d\xi}\hat{\boldsymbol{\theta}} = \frac{dr}{d\theta}\hat{\mathbf{r}} + r\hat{\boldsymbol{\theta}},$$

where in the last step $\xi = \theta$ is set. In general, the shape of the shock front also depends on time, hence $\mathbf{r} = \mathbf{r}(\theta, t)$. Therefore in the previous equation $dr/d\theta \to \partial r/\partial\theta$. The instantaneous shock velocity is given by

$$\mathbf{v} = v_r\hat{\mathbf{r}} + v_\theta\hat{\boldsymbol{\theta}}.$$

By definition the velocity and tangent vector of the shock front are perpendicular, $\mathbf{v} \cdot \mathbf{T} = 0$, from where it follows that

$$\frac{\beta_\theta}{\beta_r} = -\frac{1}{r}\frac{\partial r}{\partial\theta}. \tag{7.8}$$

As was mentioned above, for any shock front the velocity of the material just behind it $\boldsymbol{\beta}$, as measured by the upstream (unshocked) observer, is normal to the shock front. If $\hat{\mathbf{n}}$ is the unit vector normal to the front, then $\hat{\boldsymbol{\beta}} = \boldsymbol{\beta}/|\boldsymbol{\beta}| = \hat{\mathbf{n}}$. The angle α between $\hat{\mathbf{n}}$

and $\hat{\mathbf{r}}$ is given by $\cos\alpha = \hat{\mathbf{n}} \cdot \hat{\mathbf{r}} = \hat{\boldsymbol{\beta}} \cdot \hat{\mathbf{r}}$. It follows that

$$\tan\alpha = \frac{\beta_\theta}{\beta r} = -\frac{1}{r}\frac{\partial r}{\partial \theta} = -\frac{\partial \ln r}{\partial \theta}, \tag{7.9}$$

where equation 7.8 was used in the second equality. Until equation 7.9 the analysis is exact. The expression can be further simplified by considering that, as long as $\Gamma \gg 1$, $R \sim \beta ct$. Therefore,

$$\frac{\partial \ln r}{\partial \theta} \sim \frac{\partial \ln \beta}{\partial \theta}.$$

Now consider $u \equiv \beta\Gamma$. By definition, it follows that $\beta = u/\sqrt{1+u^2}$ and the right hand side of the previous equation can be rewritten as

$$\frac{\partial \ln \beta}{\partial \theta} = \frac{\partial}{\partial \theta}\left[\ln u - \frac{1}{2}\ln\left(1+u^2\right)\right] = \frac{1}{1+u^2}\frac{\partial \ln u}{\partial \theta}.$$

Therefore, from the definition of u it follows that

$$\frac{\partial \ln \beta}{\partial \theta} = \frac{1}{\Gamma^2}\frac{\partial \ln u}{\partial \theta}. \tag{7.10}$$

Now, the u changes by a factor of $\sim u$ from the centre to the edges of the jet (assuming slow moving edges),

$$\frac{\partial \ln u}{\partial \theta} = \frac{1}{u}\frac{\partial u}{\partial \theta} \sim -\frac{1}{\Delta\theta}.$$

Inserting this result in equation 7.10, and combining with 7.8 then

$$\frac{\beta_\theta}{\beta_r} \sim -\frac{1}{\Gamma^2 \Delta\theta}. \tag{7.11}$$

In the relativistic regime, $\Gamma \gg 1$, $\alpha \ll 1$ and $\beta_r \sim 1$. Collecting these considerations,

$$\beta_\theta \sim \frac{1}{\Gamma^2\Delta\theta} \approx \frac{1}{\Gamma^2\theta_J}, \tag{7.12}$$

where in the last equality a top hat jet with half-opening angle θ_J is considered. Now,

considering that the lateral size of the jet is $R_\perp \approx R\theta_J$, then

$$\frac{dR_\perp}{dR} = \frac{d\theta_J}{dR} + \theta_J \approx (\theta_J + \beta_\theta) \tag{7.13}$$

and therefore

$$\frac{d\theta_j}{dR} = \frac{1}{\Gamma^2 \theta_j R} \implies \frac{d\theta_j}{dln\ R} = \frac{1}{\Gamma^2 \theta_j}, \tag{7.14}$$

where in comparison with the previous case eq. 7.6 there is an extra factor of $1/\Gamma\theta_j$ (Shapiro, 1979; Kumar & Granot, 2003b; Granot & Piran, 2012). Initially, while $\Gamma\theta_j \gg 1$, this significantly suppresses lateral spreading, but after the jet break when $\Gamma \sim 1/\theta_j$ grows quickly (e.g. Granot & Piran 2012 and the next section).

For compactness, following Granot & Piran (2012), eqs. 7.6 and 7.14 can be summarized as

$$\frac{d\theta_j}{dln\ R} = \frac{1}{\Gamma^{a+1}\theta_j^a}, \quad a = 0, 1. \tag{7.15}$$

For a uniform, isotropic CBM with particle density n the swept-up mass m by a laterally spreading shell with half-opening angle θ_j at a radius R is given by

$$\frac{dm}{dR} = 2\pi n m_p \left[(1 - \cos\theta_j) R^2 + \frac{1}{3} \sin\theta_j R^3 \frac{d\theta_j}{dR} \right]. \tag{7.16}$$

The previous equation assumes that the jet is at all times a conical section of a sphere.

Dynamical evolution

Equations 7.3, 7.15 and 7.16 govern the evolution of Γ, θ_j and m respectively as a function of the radius of the blast wave R. The time since the explosion as measured in the progenitor's rest frame is given by

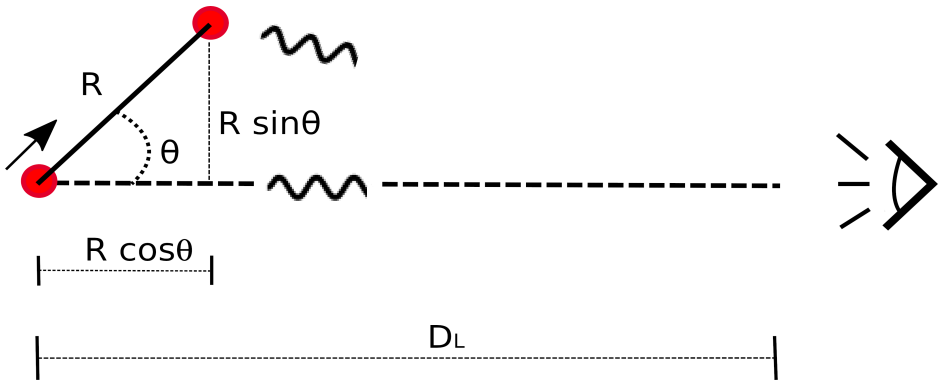

Figure 7.1: Diagram of the system set-up. A moving, synchrotron emitting source is moving at a direction forming an angle θ with respect to the line of sight of a observer. The source and observer are separated by a large distance D_L. During the duration of the experiment, the source moves a distance $R \ll D_L$.

E_{iso} (ergs)	Γ_0	$n\ (cm^{-3})$	$\theta_{j,0}$ (deg)
5×10^{51}	100	10^{-3}	10

Table 7.1: Simulation parameters for the example system discussed in section 7.1

$$t_{lab}(R) = \int_0^R \frac{dR}{\beta c}, \tag{7.17}$$

The arrival time of photons emitted from a fluid element (emitter) at time t_{lab} and radius R is given by

$$T(R,\theta) = t_{lab}(R) - \frac{R}{c}\cos\theta, \tag{7.18}$$

where θ is the angle between the direction of motion of the emitter and the observer LOS. $T = 0$ was chosen so that photons arrive at the observer at $T = 0$ if they were emited at the moment of the explosion ($t_{lab} = 0$, $R = 0$, see diagram 7.1).

To illustrate the typical jet evolution, the system with parameter set given listen in the in table 7.1 is considered. In this section the on-axis case is assumed ($\theta = 0$). The dynamical equations 7.3, 7.15 and 7.16 are solved using a fourth-order Runge-Kutta scheme. The radius R was discretized by uniformly sampling this variable in logarithmic space. To ensure the dynamics were captured correctly the minimum value R_{min} was set to $10^{-2}R_d$. In what follows an on-axis observer ($\theta = 0$) is considered. The

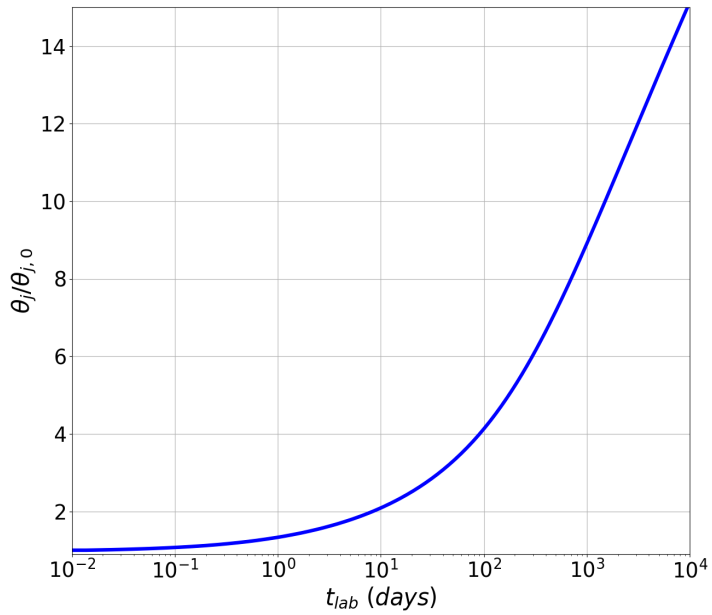

Figure 7.2: Evolution of the opening angle θ_j in units of its initial value $\theta_{j,0}$ for a top hat jet model with parameters give by 7.1, and $a = 1$.

deceleration radius for these parameters is $R_d = 4.3 \times 10^{17}\ cm$, which corresponds to $T_d \approx 717s \sim 10^{-2}$ days. Figure 7.2 shows the evolution of the opening angle θ_j in units of its initial value $\theta_{j,0}$. The opening angle initially grows slowly. By jet break, when $\Gamma \sim 1/\theta_j$ at $T \approx 10$ days the opening angle has grown a factor of two. As the swept-up mass $m \propto (1 - \cos\theta)R^3$, the spreading jet will accumulate slightly more particles at smaller radii, which hastens its deceleration.

This is illustrated in figure 7.3, which shows the evolution of the R (left panel) and Γ as a function of T. The solid blue line corresponds to a laterally spreading jet. The red dashed line corresponds to the collimated case (constant $\theta_j = \theta_0$) for comparison. The collimated jet begins to overtake the spreading jet after $t_{lab} \sim 0.1$ days, and by $t_{lab} = 100$ days has a radius which is a factor of 2 larger than the spreading jet. The evolution of the Lorentz factor in both cases is similar. After the initial coasting phase it decreases as $\Gamma \propto T^{-3/8}$, as is expected for the relativistic Blandford-Mckee blastwave. As the systems become mildly relativistic they move away from this scaling. After $T \approx 10$ days the evolution of the two systems separate. The spreading jet presents a steeper decay until $T \approx 185$ days, when its Lorentz factor begins to flatten as the system approaches the Newtonian regime.

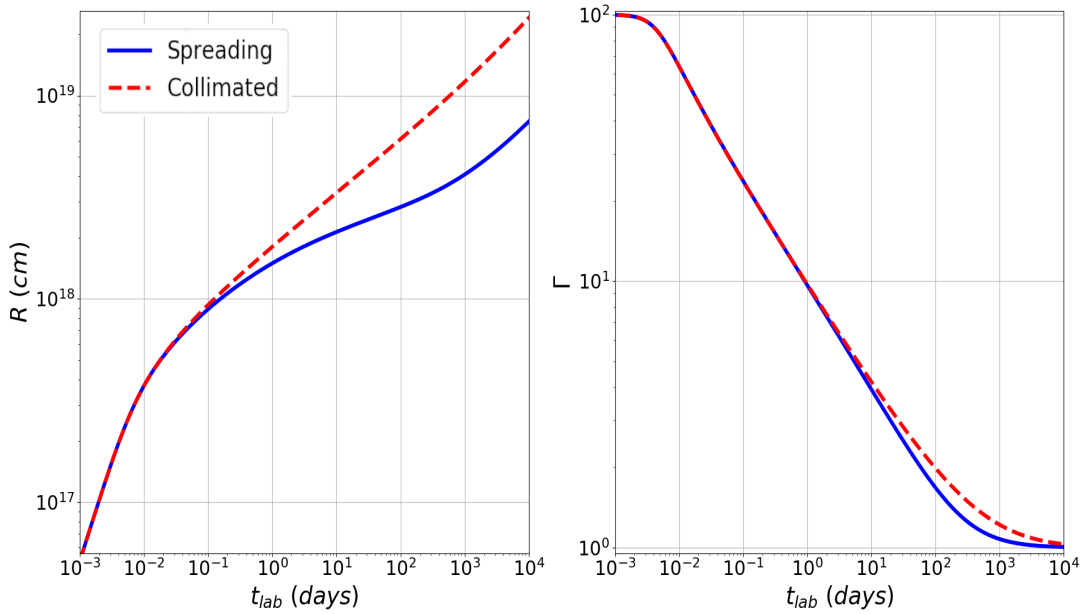

Figure 7.3: Left panel: the shell radius R as a function of t_{lab}. Right panel: evolution of the Lorentz factor as a function of t_{lab}. In both cases $\theta = 0$. The dashed red curve corresponds to a collimated jet, and the solid blue curves to a laterally spreading jet with $a = 1$.

7.2 Afterglow radiation physics

As was discussed in the previous section, as the shock expands it sweeps up and heats-up the CBM particles. It is typically assumed that the CBM are accelerated by a Fermi process in the shock to a power law distribution in the Lorentz factor such that $N(\gamma_e)d\gamma_e \propto \gamma_e^{-p}$. It is also assumed that $\gamma_e \geq \gamma_m$, where γ_m is the minimum Lorentz factor, and $p > 2$ (Sari et al., 1998).

The microphysics of the electrons is summarized in two equipartition parameters. The first of these is the fraction of shock energy transferred to the electrons ϵ_e. The shocked material has a particle density $4\Gamma n$ and energy density $4\Gamma^2 n m_p c^2$ (Blandford & McKee, 1976; Sari et al., 1998). With this, the total energy contained in the electrons and the number density of electrons behind the shock can be written as

$$\begin{aligned} 4\Gamma^2 n m_p c^2 \epsilon_e &= \int_{\gamma_m}^{\infty} \gamma_e m_e c^2 N_e d\gamma_e \propto \int_{\gamma_m}^{\infty} m_e c^2 \gamma_e^{-p+1} d\gamma_e, \\ 4\Gamma n &= \int_{\gamma_m}^{\infty} N_e d\gamma_e \propto \int_{\gamma_m}^{\infty} \gamma_e^{-p} d\gamma_e \end{aligned}$$

where m_e is the electron mass and the proportionality constant in the second step is the same for both equations. Combining them and evaluating the integrals it is found that

$$\gamma_m = \epsilon_e \frac{p-2}{p-1} \frac{m_p}{me} \Gamma. \tag{7.19}$$

The second equipartition parameter is the fraction of the shock energy in magnetic field energy density ϵ_B. The magnetic field intensity B behind the shock is (Sari et al., 1998)

$$\frac{B^2}{8\pi} = \epsilon_B e, \tag{7.20}$$

where e is the thermal energy density, given by the jump conditions,

$$e = \frac{\hat{\gamma}\Gamma + 1}{\hat{\gamma} - 1}(\Gamma - 1) n m_p c^2 \approx 4\Gamma^2 n m_p c^2, \tag{7.21}$$

where the last step holds for $\Gamma \gg 1$, as for a relativistic fluid $\hat{\gamma} = 4/3$. Therefore,

$$B = \left[8\pi \epsilon_B \frac{\hat{\gamma}\Gamma + 1}{\hat{\gamma} - 1}(\Gamma - 1) n m_p c^2 \right]^{1/2} \approx \left(32\pi n m_p \epsilon_b\right)^{1/2} c\Gamma. \tag{7.22}$$

For the purpose of the numerical calculations presented in chapter 8 the full expressions (after the first equality) where used for B and e.

Synchrotron power and spectrum

Synchrotron radiation is generated by the gyration of relativistic electrons around magnetic field lines. The synchrotron power of a single electron received by an observer at an angle θ is given by

$$P(\gamma_e) = \frac{\sigma_T c B^2 \gamma_e^2 \beta_e^2}{6\pi} \delta^2, \tag{7.23}$$

where $\beta_e = (1 - \gamma_e^{-2})^{1/2}$, σ_T the Thompson scattering cross-section (Rybicki & Lightman, 1985) and $\delta = [\Gamma(1 - \beta \cos\theta)]^{-1}$ is the Doppler factor, which transforms the

power from the fluid co-moving frame to that received by the observer. The spectrum of a single electron is given $P(\nu) \propto \nu^{1/3}$ for $\nu < \nu_{sync}$ and an exponential decay for $\nu > \nu_{sync}$. The spectrum peaks at ν_{sync}, given by

$$\nu_{sync}(\gamma_e) = \frac{eB\gamma_e^2}{2\pi m_e c}\delta, \tag{7.24}$$

The peak spectral power $P_{\nu,max}$ is given by

$$P_{\nu,max} \approx \frac{P(\nu_{sync})}{\nu_{sync}} = \frac{\sigma_T m_e c^2 \beta_e^2 B}{3e}\delta. \tag{7.25}$$

The previous formulae is often simplified by setting $\beta_e \approx 1$ (e.g. (Sari et al., 1998), Kumar & Zhang (2015)), which holds in the relativistic regime. In this limit and for $\theta = 0$ the Doppler factor becomes $\delta \approx \Gamma$.

The single-electron spectrum described above is modified if a significant fraction of the particle's energy can be lost via synchrotron radiation. This can be the case if $\gamma_e > \gamma_c$, where γ_c is the Lorentz factor of electrons such that

$$\Gamma\gamma_c m_e c^2 = \Gamma^2 P(\gamma_c) T \implies \gamma_c = \frac{6\pi m_e c}{\sigma_T \Gamma B^2 T}, \tag{7.26}$$

where T is the observer time given by eq. 7.18 for $\theta = 0$. The associated synchrotron frequency $\nu_c \equiv \nu_{sync}(\gamma_c)$. Cooling adds a new arm to the synchrotron spectrum. If an electron has $\gamma_e > \gamma_c$, it cools via the synchrotron process. The frequency will decrease as $\nu \propto \gamma_e^2$ and its energy as ν_e. Therefore, the spectral power varies as $P \propto \nu^{1/2}$ in this regime.

Similarly, the frequency associated with γ_m is $\nu_m \equiv \nu_{sync}(\gamma_m)$. ν_c and ν_m are known as break frequencies, as they separate branches of the spectrum. The total spectrum is obtained by integrating over the electron Lorentz factor distribution. If $\gamma_m > \gamma_c$, case

know as *fast cooling*, the flux is given by

$$\frac{F_\nu}{F_{\nu,max}} = \begin{cases} (\nu/\nu_c)^{1/3}, & \nu_c > \nu, \\ (\nu/\nu_c)^{-1/2}, & \nu_m > \nu > \nu_c, \\ (\nu_m/\nu_c)^{-1/2}(\nu/\nu_m)^{-p/2}, & \nu > \nu_m. \end{cases} \tag{7.27}$$

In the case $\gamma_c > \gamma_m$, known as *slow cooling*, the spectrum reads

$$\frac{F_\nu}{F_{\nu,max}} = \begin{cases} (\nu/\nu_m)^{1/3}, & \nu_m > \nu, \\ (\nu/\nu_m)^{-(p-1)/2}, & \nu_c > \nu > \nu_m, \\ (\nu_c/\nu_m)^{-(p-1f)/2}(\nu/\nu_c)^{-p/2}, & \nu > \nu_c. \end{cases} \tag{7.28}$$

Here $F_{\nu,max}$ is the maximum synchrotron flux, given by

$$F_{\nu,max} = \frac{N_e P_{\nu,max}}{4\pi D_L^2}\delta^2, \tag{7.29}$$

where N_e is the number of emitting electrons and D_L is the luminosity distance to the source. The factor δ^2 in due to the relativistic beaming effect: the isotropic emission in the electron co-moving frame is beamed into a cone of solid solid angle $\Omega = 4\pi/\delta^2$ in the lab frame (see section 7.3). Therefore with this it holds that $F_\nu = \delta^3 F'_{\nu'}$, which is consistent with the transformation of the Lorentz invariant specific intensity, for which $I_\nu/\nu^3 = I'_{\nu'}/\nu'^3$ (e.g. Rybicki & Lightman 1985).

7.3 Special relativistic effects

In the previous section the break frequencies and peak synchrotron spectral power were obtained as measured by a stationary observer. In this section the relativistic transformations used to obtain these formulae are justified.

Additionally, the apparent superluminal motion of relativistic sources is discussed. This effect is especially important for the analysis of afterglow images (see chapter

8).

Time dilation and the relativistic Doppler effect

Consider the situation illustrated in figure 7.1, which shows a stationary reference frame K and and a frame K' moving towards it with velocity $\beta = v/c$ and Lorentz factor Γ. Elementary special relativity shows that a time interval Δt measured in K between two events is related to the interval $\Delta t'$ in K' by $\Delta t = \Gamma \Delta t'$. Consequently, photons radiated by an emitter which moves with K' of frequency ν'_s will have frequency $\nu_s = \nu'_s/\Gamma$ in K', where s indicates the *source* frequency (Landau & Lifshitz, 1980; Rybicki & Lightman, 1985).

Therefore, as $\Gamma \geq 1$, time dilation will redshift the photons. An additional effect which must be accounted for is the change in photon arrival time due to the motion of the source.

In the frame K the photon travels a distance equal to its wavelength $\lambda_s = c/\nu_s$ in a time $\Delta t = 1/\nu_s$ (one period of radiation). During this time the source will have moved a distance $d = v\Delta t cos\theta$ towards the observer. The difference in arrival time Δt_A of photons emitted from the source before/after the displacement is $\Delta t_A = \Delta t - d/c = \Delta t(1 - \beta \cos\theta)$. It follows that the frequency measured by the observer is

$$\nu_r = \Delta t_A^{-1} = \frac{\nu_s}{1 - \beta \cos\theta} = \frac{\nu'_s}{\Gamma(1 - \beta \cos\theta)} = \delta \nu'_s, \tag{7.30}$$

where, as was discussed about, $\delta \equiv [\Gamma(1 - \beta \cos\theta)]^{-1}$ is known as the Doppler factor (Rybicki & Lightman, 1985). For simplicity, the subindex is dropped on the received frequency, $\nu \equiv \nu_r$.

Relativistic beaming and the spectral flux

Relativistic beaming is a consequence of the relativistic velocity addition formula when applied to photons (Einstein, 1905; Landau & Lifshitz, 1980; Rybicki & Lightman,

1985). If the emission from the source in the previous discussion is isotropic in K', in the K-frame it is beamed in the direction of motion of the source. In particular, if photons are emitted at an angle θ' with with respect to the x'-axis in K', then the angle θ in K obeys

$$\tan\theta = \frac{\sin\theta'}{\Gamma(\cos\theta' + \beta)}, \quad \cos\theta = \frac{\cos\theta' + \beta}{1 + \beta\cos\theta'}. \tag{7.31}$$

For photons emitted in the perpendicular direction to β, that is, $\theta' = \pi/2$, it follows that $\sin\theta = 1/\Gamma$. Therefore, the isotropic emission in K' is *beamed* into a narrow cone of opening angle $\theta \sim 1/\Gamma$ if $\Gamma \gg 1$.

This result is relevant for the spectral flux calculation, which is defined as

$$F'_\nu = \frac{1}{D_L^2}\frac{dE'}{dt' d\Omega' d\nu'_s}, \tag{7.32}$$

where D_L is the luminosity distance between the source and the receiver. Hence the previous formula gives the flux received by the observer as measured from K'.

The energy is the time-like component of a four-vector. Therefore, it transforms to the observer frame as $dE' = dE/\Gamma(1 - \beta\cos\theta) = \delta dE'$ (Landau & Lifshitz, 1980). As was discussed in the previous section, time and frequency have transform as $dt' = \delta dt$ and $d\nu'_s = d\nu/\delta$, hence $dt' d\nu'_s = dt d\nu$. The solid angle element is given by $d\Omega' = d(1 - \cos\theta')d\phi' = \sin\theta' d\theta' d\phi'$. From eq. 7.31 it can be shown that $\sin\theta d\theta = \delta^2 \sin\theta' d\theta'$, and as the azimuth angle $\phi = \phi'$ is Lorentz invariant, $d\Omega = d\Omega'/\delta^2$. Therefore, the spectral flux in the observer frame is (Rybicki & Lightman, 1985)

$$F_\nu = \delta^3 F'_\nu, \tag{7.33}$$

This result can be compared to 7.29

Apparent superluminal motion

Consider the setup in 7.1. A stationary observer is required to measure the apparent velocity of a mobile emitter. The true velocity β of the particle forms an angle θ with respect to the observer line of sight LOS. If the distance D between them is much larger than the displacement of the emitter in the duration of the experiment, the stationary observer will only measure motion in the plane perpendicular to its line of sight.

The emitter moves a distance $\Delta R = R_2 - R_1 = \beta c \Delta t_{lab}$ in the stationary lab frame in its proximity. The distant observer will measure a displacement $\Delta R \sin\theta$. As the source moves towards the observer, photons emitted at R_2 have a shorter travel time than those emitted at R_2. Due to this, the distant observer measures a compressed time interval $\Delta t = \Delta t_{lab}(1 - \beta\cos\theta)$. Therefore, the apparent velocity of the source is

$$\beta_{app} = \frac{\Delta R \sin\theta}{c\Delta t} = \frac{\Delta R \sin\theta}{c\Delta t_{lab}} = \frac{\beta \sin\theta}{1 - \beta\cos\theta}, \tag{7.34}$$

where $\beta = \Delta R / \Delta t_{lab}$ by definition. If $\theta = 0$ all of the motion is along the LOS of the observer and no motion is observed. If $\theta = \pi/2$, $\beta_{app} = \beta$, as all of the particles motion is perpendicular to the LOS. It can be shown that the maximum apparent velocity is achieved when $\cos\theta = \beta$, and $\beta_{app,max} = \Gamma\beta$. As $\Gamma \geq 1$, β_{app} can be larger than 1, that is, the observer can measure apparent superluminal motion. If the emitter is relativistic $\beta \sim 1$, then $\beta_{app} \approx \Gamma$ (Rybicki & Lightman, 1985) .

Chapter 8

Synthetic images of laterally spreading GRB jets

Shortly after the detection of the binary neutron star merger GW170817 its EM counterpart was discovered in the S0 galaxy NGC4993. This transient was subject to an unprecedented follow-up campaign across the EM spectrum. The counterpart was found to be made up of several components: a prompt sGRB detected $1.7s$ after the merger, a kilonova and a broad synchrotron afterglow, first detected 9 days post-merger at X-ray wavelengths.

In addition to light curves, ubiquitously obtained for GRB afterglows, VLBI radio images were also obtained. Mooley et al. (2018) presented radio images obtained 75 and 230 days post-merger. They found an image centroid displacement of $\sim 2.67 \pm 0.2$ mas in the sky, implying a mean apparent velocity of $\beta_{app} = 4.1 \pm 0.5$. This broke the degeneracy between a wide, quasi-isotropic ejecta and an isotropic narrowly non-spreading jet, confirming the emission was dominated by the latter. This result was further confirmed by further a radio imaged obtained at 207 days post merger, reported in Ghirlanda et al. (2019).

VLBI images are also important for breaking degeneracies in parameter estimation from light curves. As Nakar & Piran (2021) discussed, afterglow light curves observed around their peak time T_p cannot constrain the observing angle θ_{obs} well. The width of

the light curve peak can determine only the ratio of the observing angle θ_{obs} to the jet opening angle (or core size for a structured jet dominated by the central elements) θ_c. This leads to degeneracy among the parameters $\{\theta_{obs},\ \theta_c, l, \epsilon_B\}$, where $l = (E/nm_pc^2)^{1/3}$ is the Sedov length. It is known that the degeneracy can be broken by the observation of afterglow images (the centroid shift around the peak time) or the decay index of the late time afterglow light curve (the transition to the Newtonian phase) (Nakar & Piran, 2021).

In this chapter we discuss the properties of synthetic radio images of merger jets. The images are obtained using the semi-analytic formalism presented in chapter 7. We consider laterally spreading/non-spreading jets to evaluate the afterglow images. The results are applied to a GW170817-like system. We explicitly show how the combination of afterglow light curve and image observations can break the degeneracy. Implications for determination of the Hubble constant H_0 are also discussed.

8.1 Description of the numerical model

8.1.1 Discretization of the system

We consider an axis-symmetric jet and assume that all jet and shocked ambient material is confined to an infinitely thin surface (this is known as the *thin-shell* approximation). The jet is initially a polar region of a sphere with half opening angle θ_J. In general the jet will deviate from this shape at late times as different regions can have different initial velocities.

Figure 8.1 shows the coordinate system used to describe the jet. It is chosen so that the z-axis coincides with the jet symmetry axis. Without loss of generality we can assume that the observer's LOS is contained in the yz-plane.

For numerical purposes the jet is divided into a single central spherical cap and $n-1$ rings centered on the jet axis. The central spherical cap is labelled with k=0, and the concentric rings by $k = 1,\ 2, ...,\ n-1$. The spherical cap has a polar angle $\theta_{b,1}$, and

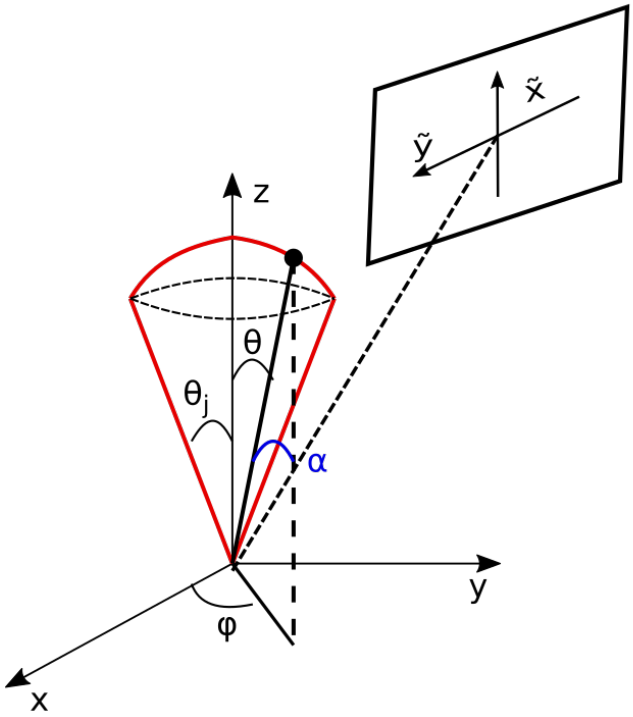

Figure 8.1: Reference frame used for the numerical calculations. The origin of the reference frame is taken to be the explosion locus. The jet symmetry axis coincides with the z-axis. Coordinates in the imagine plane are denoted by $\tilde{x}$ and $\tilde{y}$

the k-th ring is bounded by two concentric circles on the sphere with $\theta_{b,k}$ and $\theta_{b,k+1}$ given by

$$\theta_{b,k} = 2\sin^{-1}\left(\frac{k}{n}\sin\frac{\theta_j}{2}\right). \tag{8.1}$$

The spherical cap is regarded as a single region, and the k-th ring is divided in the azimuth direction ϕ into $2k+1$ equal size regions (see figure 8.2. for the case of $n = 3$) with boundaries $\phi_{kl} = 2\pi l/(2k+1)$, where $l = 0,\ 1, \ldots\ k$. This division yields a total of $\sum_{k=0}^{n-1}(2k+1) = n^2$ regions each subtending a solid angle of $2\pi(1-\cos\theta_j)/n^2$. Having divided the jet, the positions of the regions are defined by the radius R and the angles (θ_k, ϕ_{kl}), where $\theta_k = (\theta_{b,k} + \theta_{b,k-1})/2$, $\phi_{kl} = (\phi_{kl} + \phi_{kl-1})/2$. The coordinate

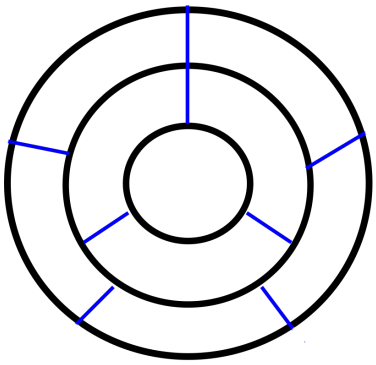

Figure 8.2: Illustration of the jet partition, projected onto the xy-plane, for the simple case of $n = 3$.

vector $\mathbf{r}_{kl}$ (x_{kl}, y_{kl}, z_{kl}) of the fluid elements kl has components

$$\begin{cases} x_{kl} = R \sin\theta_k \cos\phi_{kl}, \\ y_{kl} = R \sin\theta_k \sin\phi_{kl}, \\ z_{kl} = R \cos\theta_k. \end{cases} \tag{8.2}$$

Given a set of initial conditions, these components only evolve radially in the case of a non-spreading jet. For a laterally spreading jet the angles θ_k also evolve as we will discuss in section 8.2.

8.1.2 Construction of light curves and synthetic images

To obtain light curves we use the procedure outlined in Lamb & Kobayashi (2017) and Lamb et al. (2018). Consider an observer located in the yz-plane with the LOS forming and angle α with respect to the jet-axis. The direction along the LOS is defined by the unit vector $\hat{\mathbf{n}}_{obs} = \sin\alpha\hat{\mathbf{y}} + \cos\alpha\hat{\mathbf{z}}$. The angle between the observer and the direction of motion of the fluid element $\mathbf{r}_{kl}$, for a non-spreading jet, is given by $\alpha_{kl} = \cos^{-1}(\mathbf{r}_{kl} \cdot \hat{\mathbf{n}}_{obs})$. The contribution of this cell to the light curve at time T is obtained by inverting equation 7.18 to obtain the observed radius $R_{kl}(T)$, which determines the emission with the formalism detailed in chapter 7. For a laterally spreading jet the fluid element also has sideways expansion velocity. However, the lateral velocity is much

smaller than the radial velocity. The Doppler factor is evaluated by using the radial motion. The light curve is obtained by adding up the contribution of each individual fluid element, i.e. $F_\nu(T) = \sum_{k,l} F_{\nu,kl}(T)$.

The imaging plane is perpendicular to the LOS of the distant observer, and is defined by $\hat{\mathbf{n}}_{obs}$. Two mutually perpendicular directions in this plane are given by the basis vectors $\hat{\tilde{\mathbf{x}}} = \sin\alpha\hat{\mathbf{z}} - \cos\alpha\hat{\mathbf{x}}$, $\hat{\tilde{\mathbf{y}}} = \hat{\mathbf{x}}$, where the tildes indicate vectors in the imaging plane, as seen by an observer off-axis. This basis chosen so that the principal jet moves moves in the positive $\tilde{x}$-direction in the imaging plane. Having defined the unit vectors in the imaging plane, the coordinates of the fluid elements in the image are given by $\tilde{x}_{kl} = \mathbf{r}_{kl}\cdot\hat{\tilde{\mathbf{x}}}$, $\tilde{y}_{kl} = \mathbf{r}_{kl}\cdot\hat{\tilde{\mathbf{y}}}$. This geometry is detailed in figure 8.1. The specific intensity or brightness of a given fluid element is obtained from the spectral flux as

$$I_{\nu,kl}(T) = \left[\frac{D}{R_{kl}(T)}\right]^2 F_{\nu,kl}(T), \tag{8.3}$$

where D is the luminosity distance to the source.

8.1.3 Jet structures

Full hydrodynamics simulations show that when a merger jet needs to drill through surrounding ejecta, the emerging jet has a specific structure in energy and Lorentz factor distributions (De Colle et al., 2012; Xie et al., 2018; Gottlieb et al., 2020). These structures affect the time evolution and shape of afterglow light curves (e.g. Granot et al. 2002; Wei & Jin 2003; Zhang & Meszaros 2002; Rossi et al. 2004; Granot & Kumar 2003; Salafia et al. 2015; Lamb & Kobayashi 2017; Beniamini et al. 2020).

Here we consider the Gaussian jet model. This is characterized by a core with semi-opening angle θ_c, within which most of the energy is contained. The energy per unit solid angle and initial Lorentz factor distributions are

$$\begin{cases} \epsilon(\theta) & = \epsilon_c e^{-\theta^2/\alpha_1\theta_c^2} \\ \Gamma_0(\theta) = 1 + (\Gamma_c - 1)e^{-\theta^2/\alpha_2\theta_c^2}, \end{cases} \tag{8.4}$$

where the values $\alpha_1 = 1$, $\alpha_2 = 2$ are assumed (Resmi et. al 2018, Lamb et. al 2018). For these coefficients the deceleration radius R_d does not depend on θ. The structure is imposed as initial conditions for the dynamics.

8.1.4 Implementation of lateral spreading for structured jets

From equation 7.5 it can be seen that the degree of lateral spreading depends on the Lorentz factor of the jet and that spreading becomes significant when $\Gamma \sim 1/\theta_J$. To include this effect in the dynamics of a top-hat jet equation 7.5 is simply applied for the edges and the spreading is applied to each fluid element, as was shown in chapter 7.

For structured jets the implementation is slightly more complex. The initial conditions are given as a function of θ by equations 8.4, and the discretization described above divides the jet into rings of constant $\epsilon(\theta_k),\ \Gamma_0(\theta_k)$. Each of these rings has slightly different dynamical evolution. Each ring is assumed to be part of a top hat with initial opening angle $\theta_{b,k+1}$. Neglecting the interaction between rings, the dynamical evolution of each ring, including the spreading effect, is approximated by using the top-hat jet model. Similar approaches have been considered in previous studies including Lamb et al. (2018) and Ryan et al. (2020).

8.2 Synthetic radio images of GRB afterglows

Recently 2D (Granot et al., 2018) and 3D hydrodynamics models (Zrake et al., 2018) have been used to obtain synthetic images in the context of the NS merger event GW170817. Semi-analytic models have been used extensively for light curve calculation,

both for simple top-hat jets and diverse structured jets. Lateral spreading is generally introduced in semi-analytic models by assuming a simplified model, such as the formalism presented in Granot & Piran (2012). Ryan et al. (2020) and Lamb et al. (2018) take similar approaches, modelling this feature as sound-speed expansion of the jet edges. However, the application of semi-analytic models to imaging in the literature is generally limited to non-spreading jets. Semi-analytic imaging was presented in Gill & Granot (2018) for Gaussian and power law structured, non-spreading jets. In Lu et al. (2020) a semi-analytic effective 1-D formalism is presented for which lateral spreading is derived by considering momentum conservation and pressure gradients. In this paper the authors show the evolution of the numerical grid points, but explicit imaging is not provided.

Following Granot & Piran (2012), lateral spreading begins after the jet expands to a radius $R = R_d$. Once the solid angle of the jet increases, the jet decelerates faster. The effect of lateral spreading is not significant in the rising part of the light curves. However, the light curve peaks earlier for laterally spreading jets. The decay index after the peak depends on the lateral spreading.

In this chapter the synthetic radio images of laterally spreading GRB jets are obtained using the semi-analytic model which is described in the previous chapter. The deceleration of the jet is caused by mass build-up on the shock shell and is governed by equation 7.3. The swept-up mass is given by 7.16. The evolution of the opening angle is given by 7.15, with $a = 1$.

Radio imaging has been proposed as a tool to break the degeneracy between radial and angular structured jets (Gill & Granot, 2018) or between isotropic and jet-like ejecta (Mooley et al., 2018). In particular, obtaining the image centroid, defined as the surface brightness-weighed centre of the image,

$$\tilde{x}_c = \frac{1}{\int I_\nu d\tilde{x}' d\tilde{y}'} \int \tilde{x}' I_\nu d\tilde{x}' d\tilde{y}', \tag{8.5}$$

was key for this purpose. For spherical blast waves the centroid does not move $\tilde{x}_c = 0$. This is also the case for jets observed exactly on axis (when the LOS runs exactly

E (ergs)	Γ_0	n (cm^{-3})	$\theta_{c,0}$ (deg)	$\theta_{j,0}$ (deg)	ϵ_e	ϵ_b	p
5×10^{51}	100	0.01	3	20	0.1	0.01	2.16

Table 8.1: Jet parameters used to illustrate the properties of synthetic radio images.

along the jet axis). For jets observed off-axis, at early times $\tilde{x}_c$ moves in the principal jet direction. For relativistic jets we could observe the superluminal motion of the jet in the sky.

To illustrate this, consider a typical jet with parameters given in table 8.1 (e.g. Lamb & Kobayashi 2017; Zrake et al. 2018). Figure 8.3 shows the light curves obtained for $\alpha = 0^\circ,\ 20^\circ\ , 30^\circ$ and 45°. The on-axis light curves are very similar for the non-spreading (left panel) and spreading cases (right panel), with the latter presenting a slightly dimmer peak. For the off-axis cases, the light curves obtained for the laterally spreading jet show a slightly faster at early times, an earlier peak time and a faster asymptotic decay. The early brightening is due energy spreading to the wings of the jet, which are closer to the observer LOS. The steeper decay after peak time is again due to lateral spreading transporting energy away from the core (Lu et al., 2020). The peak times for the non-spreading case are $T_p \approx 1.4,\ 33,\ 97$ and 284 days, and for the spreading-jet $T_p \approx 0.8,\ 20,\ 51$ and 122 days (for $\alpha = 0^\circ,\ 20^\circ\ , 30^\circ$ and 45° respectively).

Figure 8.4 shows synthetic radio images of the afterglows for $\alpha = 20^\circ$ from the jet axis, at times $T = 44,\ 75$ and 230 days after the initial explosion. The surface brightness in each image is normalized to the mean brightness $I_{\nu,mean}$, with the colour map covering the range $0.01 I_{\nu,mean} - I_{\nu,mean}$. The red crosses indicate the position of the centroid in each image. Note that distances in the imaging plane scale with distance as 41.3 Mpc/D. The counter-jet does not appear in the images as its brightness falls below the brightness threshold.

In the non-spreading case (left column) the principal jet always moves in the positive $\tilde{x}$-direction (the counter-jet moves in the opposite direction but is not shown in the figure), leaving the explosion origin behind ($\tilde{x} = 0$) in the imaging plane. The images resemble a sliced ellipsoid, and present a gradual decrease in brightness from front

(right-most edge) to back (left-most edge). The extension along the $\tilde{x}$-direction is around $2-4$ times that along $\tilde{y}$. In contrast, the morphology of the laterally spreading jet images is much closer to circular, as they present excess (reduced) growth along $\tilde{y}$ ($\tilde{x}$). In both cases the counter jet can be seen at $T = 230$ days. In the non-spreading case as a small, round feature close to the explosion origin. In the spreading case as an excess brightness, as lateral spreading leads the principal jet to overlap the counter jet in the imaging pane.

Figures 8.5 shows images for the same times corresponding to $\alpha = 30^{\circ}$. In this case the morphological and structural properties are similar to those found for $\alpha = 20^{\circ}$. The images for $\alpha = 45^{\circ}$ are presented in figure 8.6. The non-spreading jet images (left column) are initially rounder, with the asymmetry developing later on, as can be seen for $T = 230$ days. The laterally spreading images (right column) are flatter, and a structure similar to the previous cases develops by $T = 230$ days, when a dim ring encircles a central bright section. In contrast to the previous two laterally spreading cases, the principal and counter jets do not overlap at $T = 230$ days for $\alpha = 45^{\circ}$.

In addition, lateral spreading also causes the fluid elements to rotate around the origin of the imaging plane. When the jet-opening angle has matched the observing angle, $\theta_j = \alpha$, the apparent motion of the outermost components is in the negative $\tilde{x}$- direction. This gives rise to the features described in following sections, such as the centroid motion reversal.

8.2.1 Evolution of the centroid of jet images

The difference in the dynamical evolution of the two cases (non-spreading and spreading) results in significantly different evolution for the centroid shifts. This is illustrated in figures 8.7-8.9. In figure 8.7 the evolution of the image centroid is shown for jets observed at angles $\alpha = 20^{\circ},\ 30^{\circ}$ and 45°. For the non-spreading jet the centroid quickly moves away from the explosion point in the sky. As the jet decelerates so does the apparent motion of the centroid. At very late times ($T \sim 1000$ days in all three cases), the centroid reverses its motion. The evolution in the case of the laterally

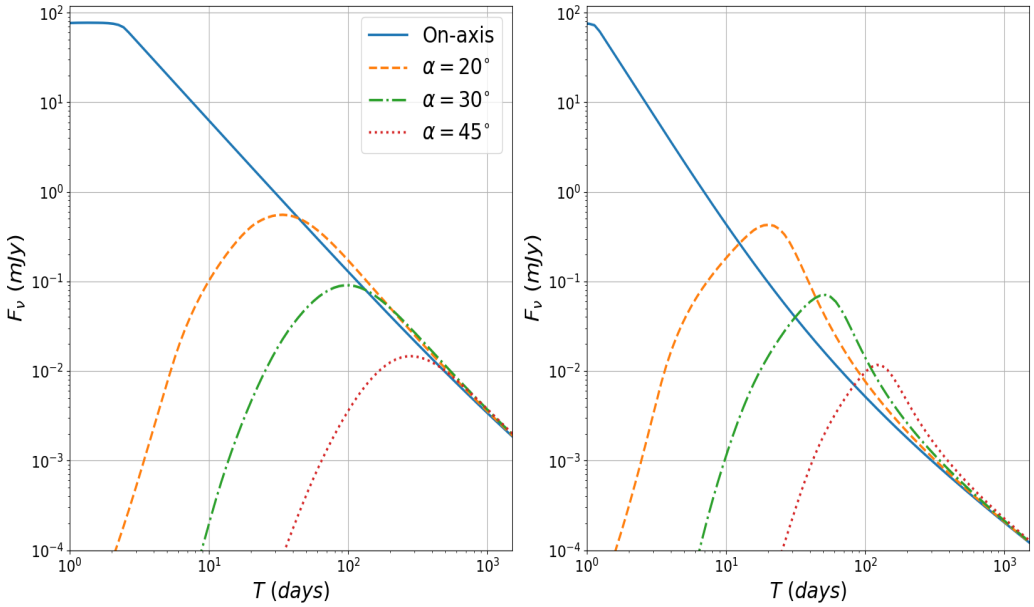

Figure 8.3: Light curves for a Gaussian jet obtained at frequency $\nu = 5\ GHz$ for a non-spreading jet case (left panel) and a case which includes lateral spreading (right panel). The light curves correspond to an on-axis observer (solid blue lines), and observers at $\alpha = 20°$ (orange dashed lines), $\alpha = 30°$ (green dashed-dotted lines) and $\alpha = 45°$ (red dotted lines).

spreading jet is similar, but the maximum displacement of the centroid is reached much earlier, at $T \sim 340,\ 335$ and 330 days for $\alpha = 20°,\ 30°$ and $45°$ respectively. By these times, the light curve fluxes decrease by a factors of $\sim 180,\ 45$ and 7 for the spreading jet. The centroid position continues to move backwards and crosses $\tilde{x} = 0$. The centroid motion reverses once more and asymptotically approaches $\tilde{x} = 0$ after several thousand days.

The centroid behaviour here described for the non-spreading case can be compared to other semi-analytic calculations. In Gill & Granot (2018) semi-analytic simulations of non-spreading jets are presented for several structures, including Gaussian jets, power-law jets and quasi-sperhical ejecta. In this work the authors use the fluxes of the individual fluid elements, instead of the surface brightness, as weights in the centroid calculations. The two approaches were compared using the model described this chapter and the parameters reported in Gill & Granot (2018) for the Gaussian jet. The flux-weighted and brightness-weighted calculations agree until the centroid displacement of the latter approaches peak displacement. The flux-weighted centroid displacement peaks later (at $T \approx 4700$ days post-merger for the flux-weighted calculation

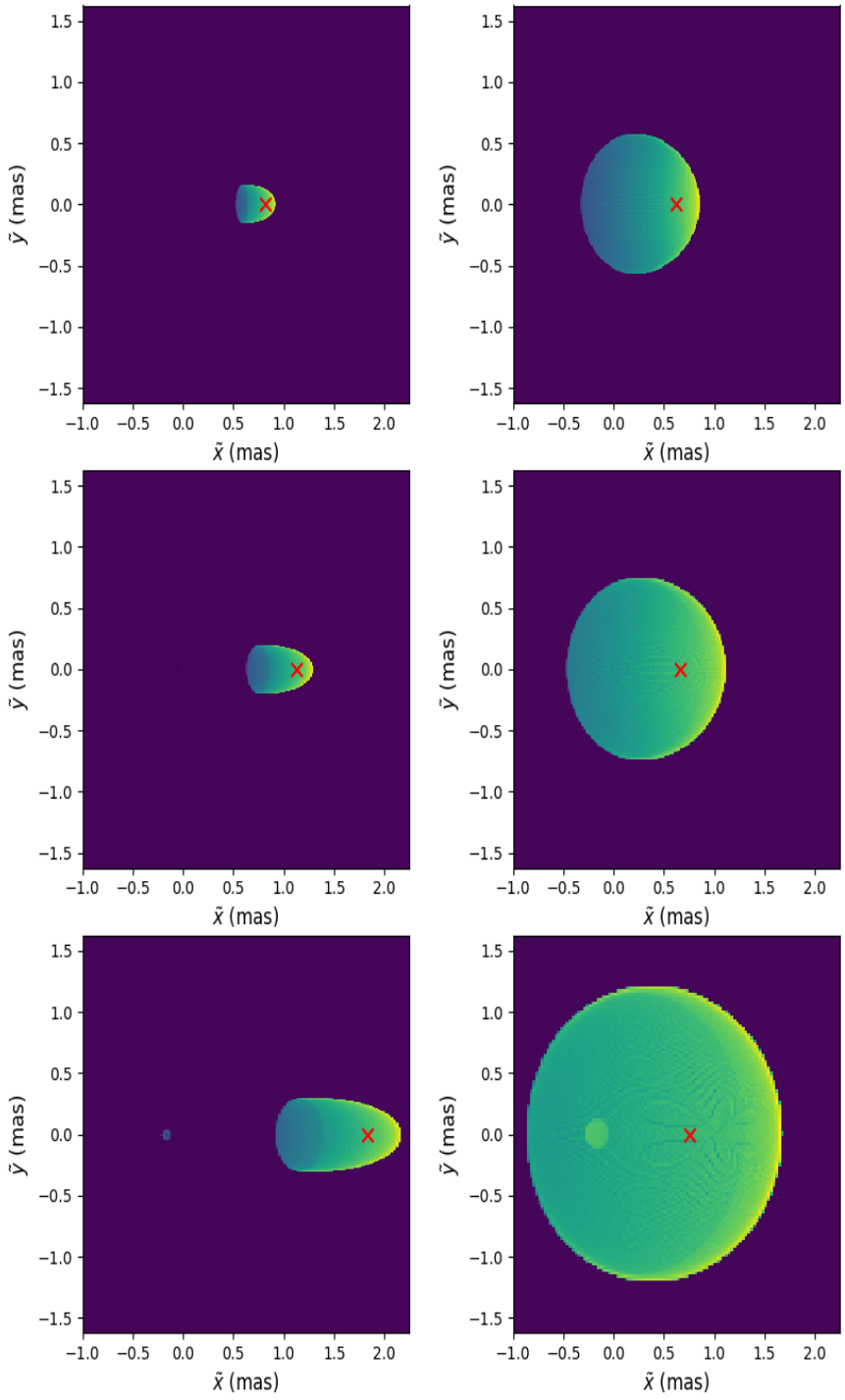

Figure 8.4: Radio images ($\nu = 5\ GHz$) at times 44, 75 and 230 days after explosion for an observer with line of sight at $\alpha = 20^{\circ}$ from the jet axis and a distance of $D = 41.3$ Mpc from the source. The left and right columns are for non-spreading and spreading jets respectively. The images are normalized to the mean brightness $I_{\nu,\mathrm{mean}}$ in each frame, with a background threshold set at $0.01 I_{\nu,\mathrm{mean}}$. The red crosses mark the position of the image centroid.

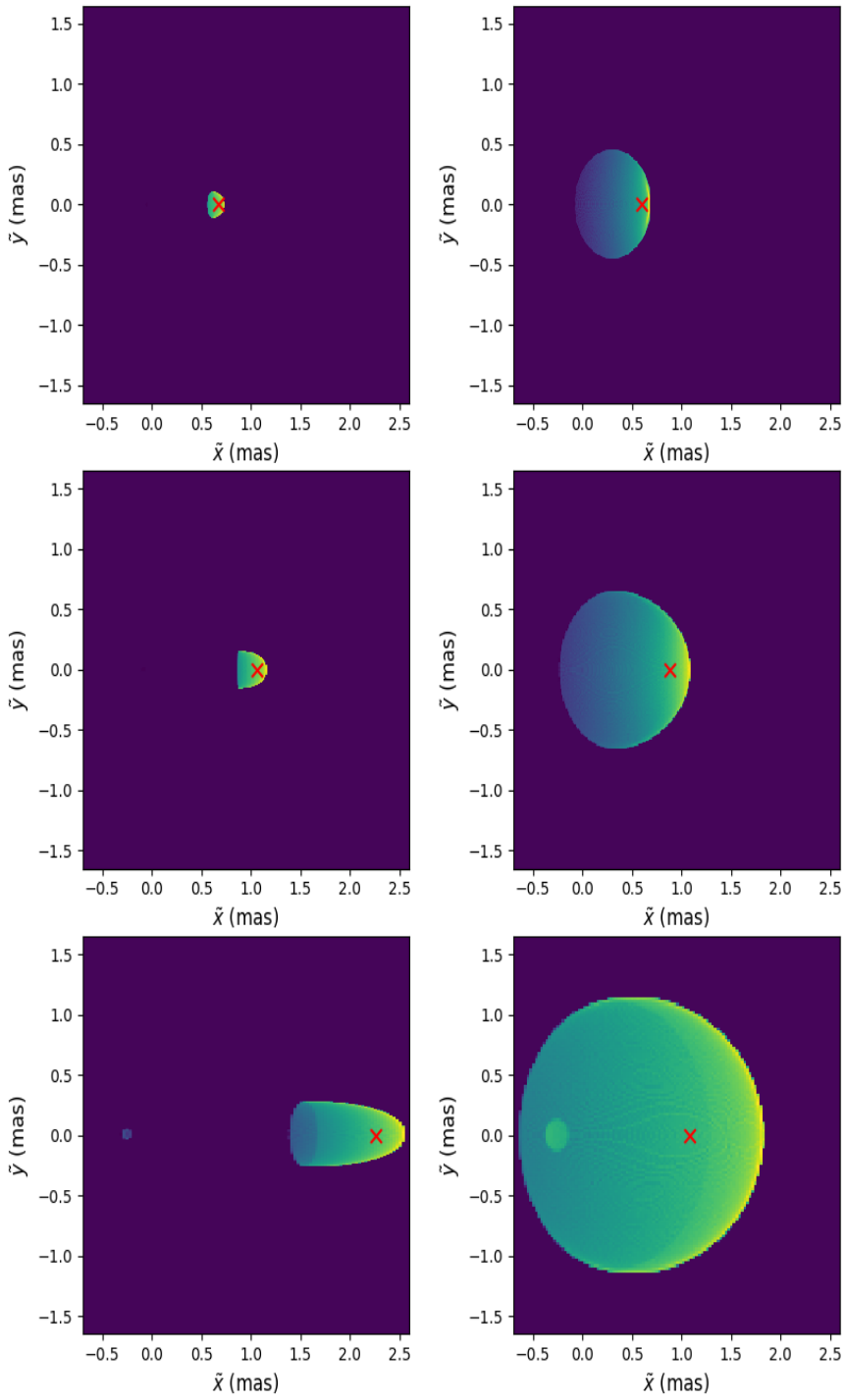

Figure 8.5: The same as figure 8.4 for $\alpha = 30°$.

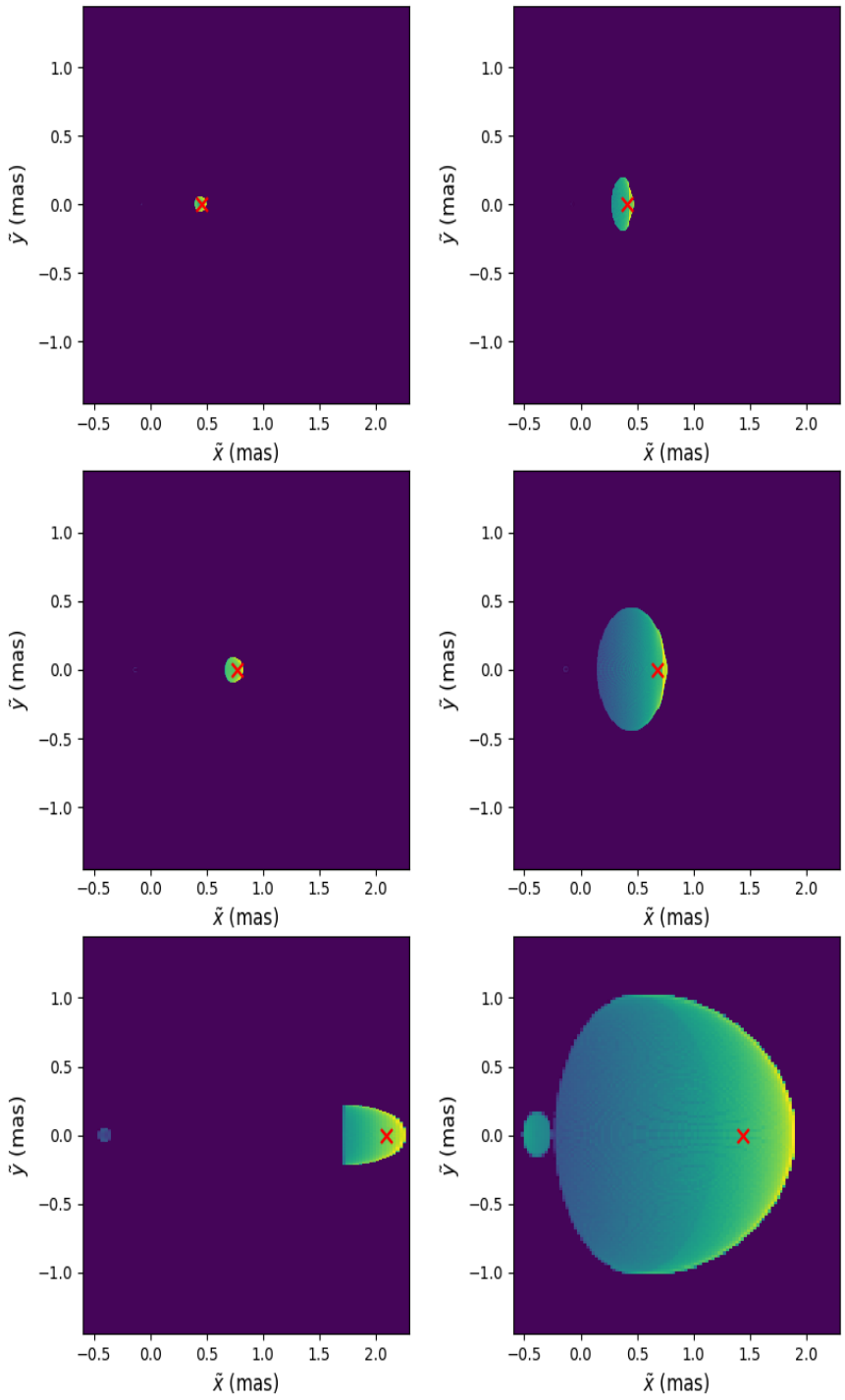

Figure 8.6: The same as figure 8.4 for $\alpha = 45°$.

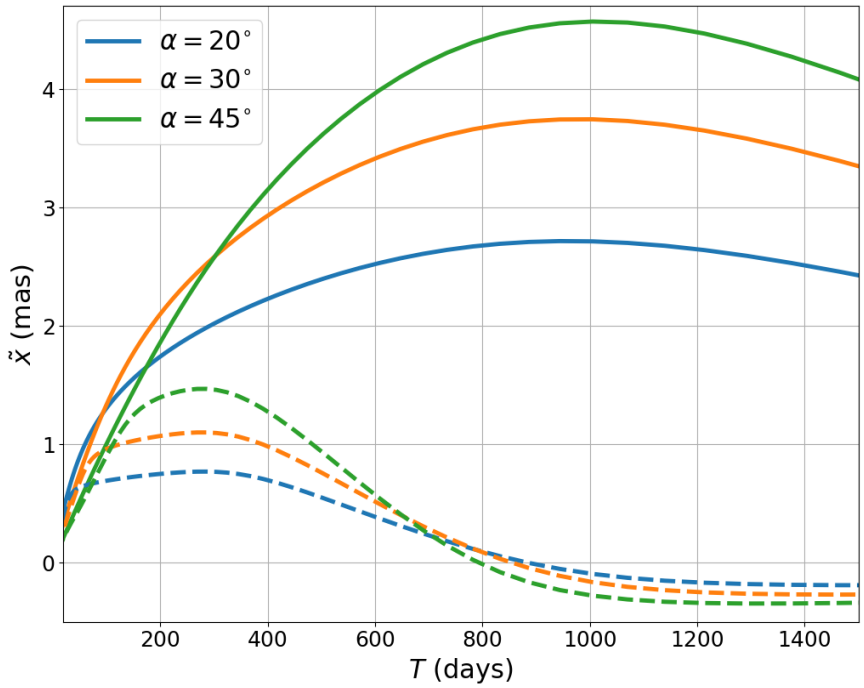

Figure 8.7: Evolution of the image centroid position $\tilde{x}_c$ as a function of observer time T and observing angle α (blue: $\alpha = 20°$, orange: $\alpha = 30°$, green: $\alpha = 45°$). The solid lines are for a non-spreading jet and the dashed lines for a laterally spreading jet.

in contrast to ≈ 2500 days when surface brightness is used).

The results presented for $\alpha = 20°$ were also compared with the model in Ghirlanda et al. (2019) (private communication with Ohm Salafia, January 2021). While the surface brightness distributions are rather different, the centroid displacements in this case are $\sim 10\%$ smaller than those reported in this chapter. The differences are due to the model in Ghirlanda et al. (2019) using a Blandford-Mckee profile for each fluid element, resulting in an extended shell, in contrast to the thin-shell approximation used here.

To explain the origin of this behaviour the contributions to $\tilde{x}_c$ of the principal and counter jets to the centroid are separated in figure 8.8 (orange and green dashed lines respectively). The solid, blue line shows the overall centroid evolution for comparison. Initially, the contribution of the principal jet dominates. The counter-jet is beamed away from the observer, resulting in a comparatively weak flux and negligible contribution to the calculation at early times. In the non-spreading case (bottom panel), when the

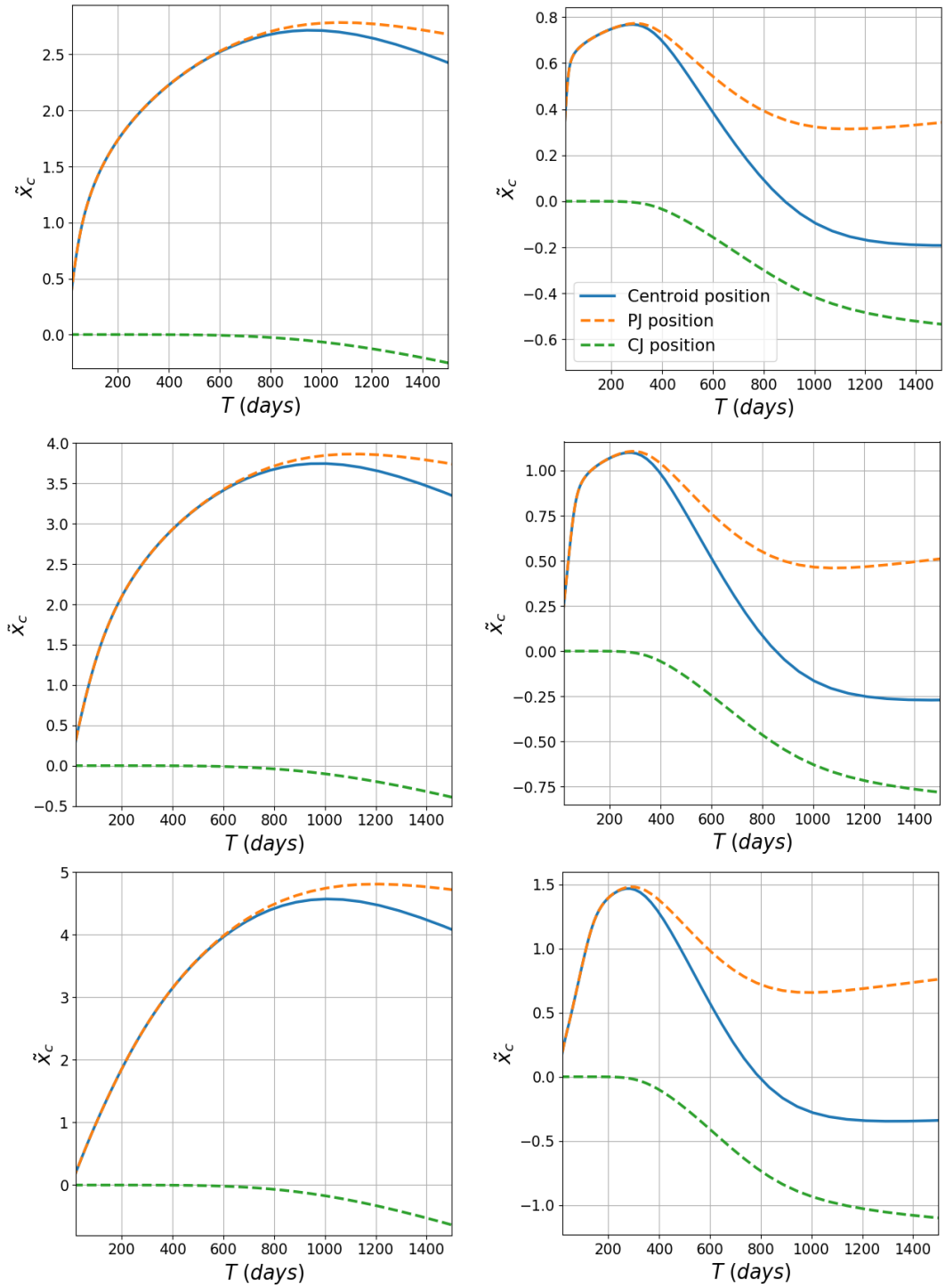

Figure 8.8: Position of the image centroid $\tilde{x}_c$ (solid blue curve) as a function of time T for a non-laterally spreading jet (left column) and laterally spreading jet (right column). The top, middle and bottom rows are obtained for observers at $\alpha = 20°,\ 30°$ and $45°$ respectively. The brightness-weighted contribution of the principal jet (dashed orange curves) and counter jet (dashed green curves) are also shown.

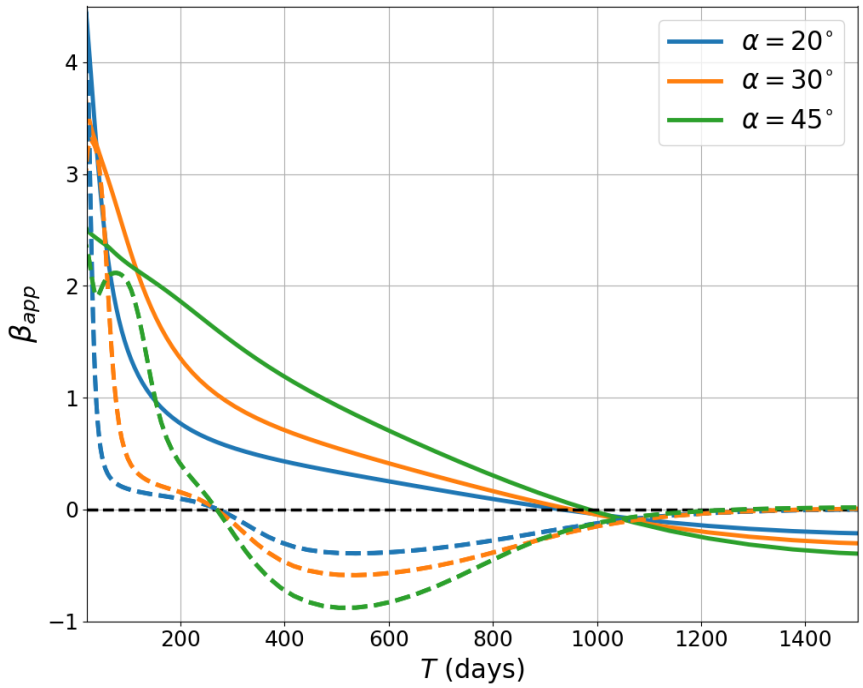

Figure 8.9: Apparent velocity of the centroid in units of c. Solid lines correspond to non-spreading jets, dashed lines to laterally spreading jets.

principal-jet decelerates sufficiently the counter-jet contribution becomes relevant and the centroid motion reverses. At very late times $T \sim 1200$ days the principal jet centroid also reverses its motion as the jet decelerates, the emission region becomes closer to homogeneous and the centroid approaches the geometric centre.

Two factors contribute to the earlier onset of centroid motion reversal for laterally spreading jets. As in the previous case, the motion of the counter jet contributes to the reversal, but this happens at much earlier times. In addition, when the edges of the jet expand to $\theta_J > \alpha$, the emission approaches that of an on-axis system. For images of on-axis jets, $\tilde{x}_c = 0$, as the emission is isotropic in the imaging plane. When $\theta_J > \alpha$, part of the shell begins to move backwards in the imaging plane. Consequently, the expansion becomes less anisotropic, which slows down the principal jet centroid displacement and eventually also contributes to the reversal.

In figure 8.9 apparent velocity of the centroid in units of c, β_{app}, is shown as a function of T. For all cases considered the centroid displacement is initially superluminal, $\beta_{app,c} > 1$. The apparent velocity presents a much steeper decrease in the case of

θ_{obs}	β_{app} (coll./spread.)	Inferred $\Delta\theta$ (coll./spread.)	% error
20°	$3.5/4.2$	$16^\circ/14^\circ$	6% / 15%
30°	$2.4/2.7$	$22^\circ/21^\circ$	15% / 22%
45°	$1.5/1.6$	$3^\circ/32^\circ$	21% / 24%

Table 8.2: Angles $\Delta\theta = \theta_{obs} - \theta_c$ inferred from the apparent velocity of the radio image centroid at light curve peak time.

laterally spreading jets. The threshold $\beta_{app} < 0$ corresponds to the reversal of the centroid motion, which in all cases peaks at subluminal velocities. After becoming negative, the velocity asymptotically approaches $\beta_{app} \to 0$ as both the principal and the counter jet decelerate (this is not shown in the figure for the non-spreading jets).

The apparent velocity of the centroid at the peak time of the light curve has been used to estimate $\Delta\theta \equiv \theta_{obs} - \theta_c$ (e.g. Mooley et al. 2018; Nakar & Piran 2021). A relativistic point-particle moving at at angle $\Delta\theta$ with respect to the LOS of a distant observer has maximum apparent velocity for $\beta = cos\Delta\theta$, when $\beta_{app} = \beta\Gamma \approx \Gamma$. The light curve peaks when for the core $\Gamma \sim 1/\Delta\theta$, i.e. when the beaming cone of the core fluid elements has expanded to the LOS. Therefore, if the apparent core velocity is taken to be the centroid velocity, at peak time $\beta_{app} \sim \Gamma$. The apparent velocity can still be used when the system is only mildly relativistic as the previous result can be written as $\beta_{app} = \Gamma\beta = \beta/(1-\beta^2)^{1/2}$, from where it follows that $\beta = \cos\Delta\theta = \beta_{app}/(1+\beta_{app}^2)^{1/2}$ (note that here Γ and β refer to the core values).

According to these analytic estimates, at the peak time of the light curve T_p, $\beta_{app} \approx 3.3, 2.0$ and 1.1 for the jets viewed at $\theta_{obs} = 20^\circ,\ 30^\circ$ and 45° respectively. The values of β_{app} found from the images and the inferred θ_{obs} are shown in table 8.2. The values of β_{app} found are larger than those expected from the analytic estimates. This implies that $\Delta\theta$ is underestimated by this calculation. The percentage errors are also provided in 8.2. The error incurred increases with the inclination θ_{obs}. This is to be expected as for larger inclinations the extended wings of the jet contribute more to the calculation, and the motion will differ more than that of a true point emitter.

8.2.2 Image structure

The centroid is a robust characteristic of a jet image which can be relatively easily obtained from observations. For brighter jets it might be possible to carry out more detailed analysis to obtain other properties, such as the lateral extension or a measure of the anisotropy of the jet, and better characterize the jet properties.

To illustrate this figure 8.10 shows the vertical mean surface brightness distributions for the principal jet (which dominates at early times), defined as

$$I_{\nu,mean}(\tilde{x}) = \frac{\int I_\nu(\tilde{x},\tilde{y})d\tilde{y}}{\Delta\tilde{y}}, \tag{8.6}$$

at times $T = 44,\ 75$ and 230 days after the explosion. The top, middle and bottom rows correspond to $\alpha = 20^\circ,\ 30^\circ$ and 45° respectively. A brightness threshold $I_\nu/I_{\nu,mean} \geq 0.01$ was set in each image.

The distributions trace the morphology of the full images in figure 8.4. For $\alpha = 20^\circ$ and the non-spreading jet (left column), the edges of the distribution increase from the rear edge to the front edge and present a small dip. The distributions move to larger $\tilde{x}$, following the motion of the images. The non-spreading jet distributions for $\alpha = 30^\circ,\ \alpha = 45^\circ$ present similar behaviour. In particular, the dip is only present in the $T = 75$ and $T = 230$-day distributions for $\alpha = 30^\circ$, and is not clearly discernible for $\alpha = 45^\circ$. For the laterally spreading jets (left column), in addition to the forwards bulk motion the rear edge can also move in the negative $\tilde{x}$-direction, and the distributions overlap each other.

These results indicate that lateral spreading introduces distinguishable features in the distributions from the non-spreading case. In particular, if an extension of the distribution edge against the forward motion of the jet is observed this would constitute a sign of lateral expansion as it would require $\theta_J > \alpha$. However this would also require the event to be bright enough, as the time at which this feature becomes apparent increases with α.

Figure 8.11 shows the full width at half maximum (FWHM) along the $\tilde{y}$-direction, as

measured at $\tilde{x} = \tilde{x}_c$. The case of the non-spreading jet presents modest growth event at late times as the expansion of the jet is preferably along $\tilde{x}$. As lateral spreading leads to significantly enhanced growth in $\tilde{y}$, the FWHM grows much faster, roughly as the physical size of the image in the sky.

8.3 Breaking degeneracy with VLBI images

GRB afterglow light curves have served as powerful tools to understand the jet physics. However, as we have discussed there is degeneracy among the system parameters. Consequently, a given light curve can be compatible with a wide range of models, with varying micro- and macrophysical parameters, type of structure (radial or angular) or synthetic structures (for example top hat, Gaussian or power law jets).

As was discussed in Nakar & Piran (2021), the main features of the afterglow light curves (i.e. peak time/width) can give constraints only on the angle ratio θ_{obs}/θ_c, but not on these angles individually.

The light curve peaks when the jet decelerates so that the core becomes visible to the observer. This happens when $\Gamma\Delta\theta \sim 1$, where the Lorentz factor of the core depends on the Sedov length $l \sim (E/nm_pc^2)^{1/3}$ of the core (the Sedov length is the radius at which a spherical blast would have swept up a rest-mass energy equal to the isotropic equivalent energy of the explosion, e.g. Piran 2005). The peak time satisfies

$$T_p \propto l\Delta\theta^2. \tag{8.7}$$

Unless there is an additional constraint on l, we can not determine the angle Δ by using the peak time T_p. Since the peak flux depends on additional unknown microphysics parameters,

$$F_\nu \propto \epsilon_e^{p-1}\epsilon_B^{(p+1)/4,} \tag{8.8}$$

the peak flux also does not provide a useful constraint on the angles (Nakar & Piran,

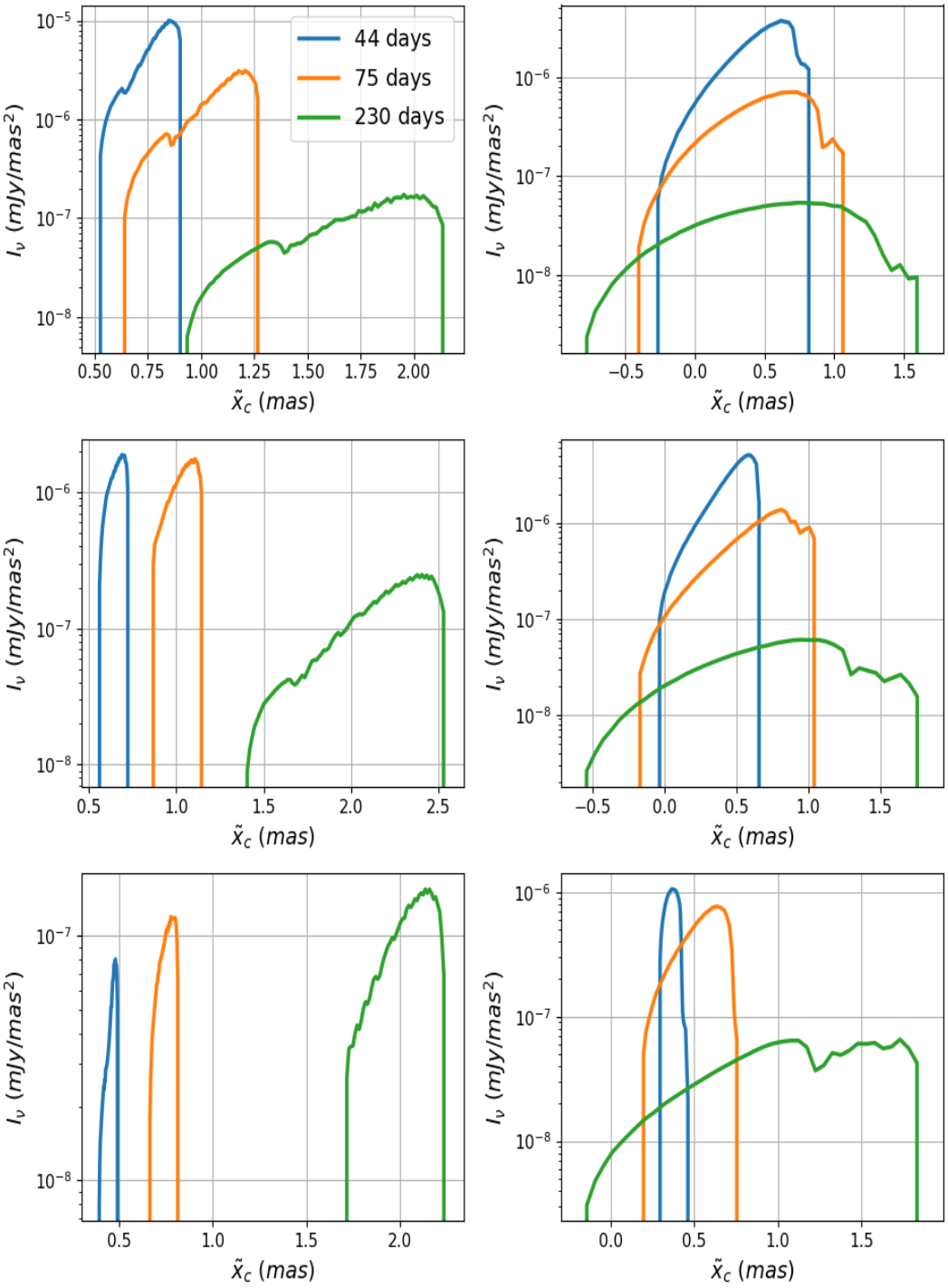

Figure 8.10: Lateral $\tilde{y}$-averaged brightness distributions for $T = 44,\ 75$ and 230 days (blue, orange and green). Left column: non-spreading jet. Right column: laterally spreading jet. The top, middle and bottom rows are for $\alpha = 20°,\ 30°$ and $45°$ respectively.

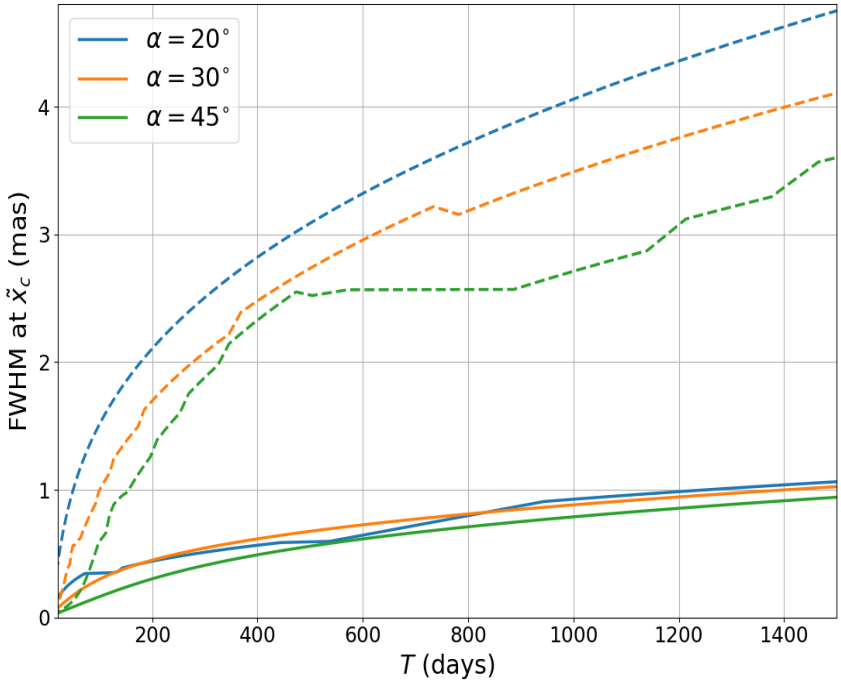

Figure 8.11: Vertical extent of the radio images, defined as the full width at half maximum (FWHM) in the $\tilde{y}$-direction at $\tilde{x} = \tilde{x}_c$. The solid lines are for a non-spreading jet, the dashed lines for a laterally spreading jet.

2021).

The light curve peaks when $\Gamma(T_p)\Delta\theta \sim 1$ is satisfied. The light curve decay becomes similar to the one seen by an observer that is along the jet axis when the whole jet core becomes visible to the observer, when it holds that

$$\Gamma(T_p + \Delta T_p)(\theta_{obs} + \theta_c) \sim 1. \tag{8.9}$$

For an on-axis observer the Lorentz factor of the emitting region decays as a power-law $\Gamma \propto T^{-k}$, where $k \sim 1/2$. The peak width satisfies the following relation:

$$\frac{T_p + \Delta T_p}{T_p} = \left[\frac{\Gamma(T_p + \Delta T_p)}{\Gamma(T_p)}\right]^{-1/k} = \left[\frac{1 + \theta_c/\theta_{obs}}{1 - \theta_c/\theta_{obs}}\right]^{-1/k}. \tag{8.10}$$

For a given jet core, a larger viewing angle results in a narrower peak. Afterglows with different core and viewing angles produce a similar peak width if they have the same angular ratio θ_{obs}/θ_c. This implies very different physical conditions can

E (ergs)	Γ_c	ϵ_e	D (Mpc)	p
$10^{52.4}$	300	$10^{-1.4}$	41.3	2.16

	n (cm^{-3})	ϵ_B	θ_c (rad)	$\theta_{J,0}$ (rad)	θ_{obs} (rad)
Model 1	1.7×10^{-5}	0.04	0.05	0.16	0.23
Model 2	4.8×10^{-5}	0.02	0.06	0.19	0.28
Model 3	1.7×10^{-4}	0.008	0.07	0.23	0.33
Model 4	4.8×10^{-4}	0.004	0.08	0.26	0.37
Model 5	1.2×10^{-3}	0.003	0.09	0.30	0.42

Table 8.3: Simulation parameters. Top table: parameters which are constant in the models. Bottom table: parameter which vary from model to model following the analytic scalings described in section 8.3.

result in almost identical light curves. To illustrate this, five different Gaussian jets are considered, with parameters given in table 8.2. The model spans two orders of magnitude of n and one of ϵ_B, and are chosen to roughly match radio ($\nu = 3\ GHz$) data for the afterglow of the NS merger GW170817. The light curves are shown in figure 8.12. At peak time the light curves are indistinguishable and remain identical until well after T_p.

The properties of radio images depend directly on the geometry and dynamics of the shock, and in particular on the apparent size of the emitting region. As was discussed in the previous section, the apparent velocity of the image centroid can be used to estimate $\Delta\theta$. Therefore these observables provide an avenue to distinguish between models. Figure 8.13 shows radio images obtained for models $1 - 5$ at 75 and 230 days (the days for which VLBI images for GW170818 were reported in Mooely et. al 2018), and around the peak time at 150 days.

In this case the model images also present a brightness distribution which decreases gradually from front to back. Note that the morphology is constant up to scaling of the image size in the sky for the different models. The position of the centroid in each image (red crosses) and the displacement with respect to the position at 75 days (solid red lines) are also shown. At 75 days the centroid calculation is dominated by the leading bright point in the image. As lateral spreading slows the radial expansion of the wings of the shell the centroid falls behind the front of the image, which can be seen in the images for 150 and 230 days post-merger. The values of the centroid displacement

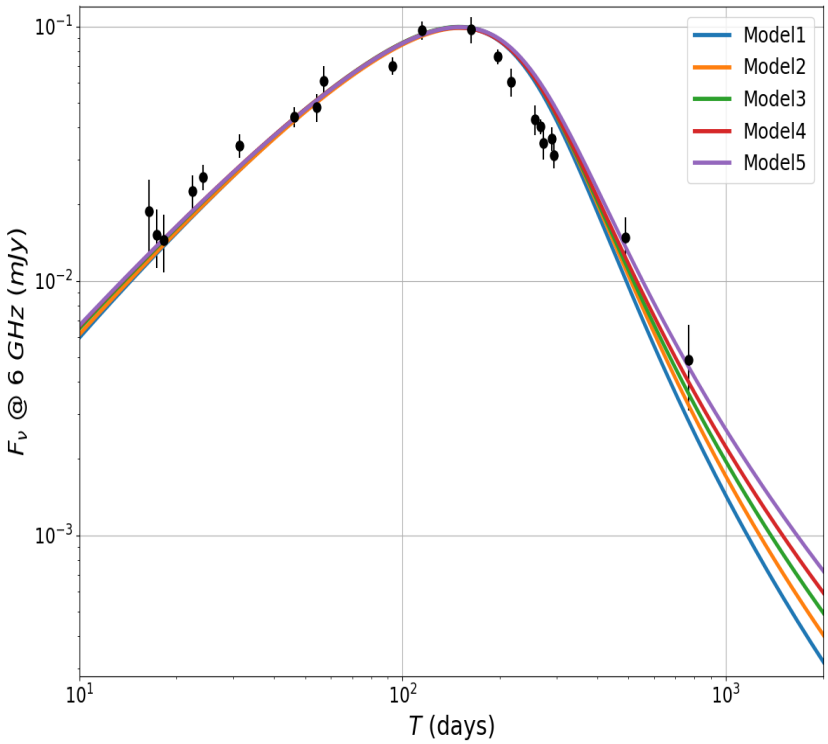

Figure 8.12: Synthetic light curves for GW17017-like systems obtained using the parameters in table 8.3. Data points for 3 GHz VLA observations (from Makhathini & et. al (2020)) are shown as black circles.

between $T = 75$ days and $T = 230$ days, and the apparent velocity computed as $\beta_{app} = \Delta x_c / c\Delta T$ are reported in table 8.4. The angle $\Delta\theta$ is also computed from β_{app} using the point particle approximation as $\theta_{obs} \approx \beta_{app}^{-1} + \theta_c$. In this case the analytical results provide a much better estimate of the inclination, with deviations of the order of a few percent.

The observed centroid displacement obtained from VLBI imaging between 75 and 230 days post-merger, as reported in Mooley et al. (2018), is shown for comparison (green solid lines delimited by crosses). They found a centroid displacement of 2.7 ± 0.3 mas, equivalent to an apparent velocity $\beta_{app} = 4.1 \pm 0.5$. Figure 8.13 quickly shows how radio imaging can be used for parameter inference, even in cases when the point particle approximation cannot related β_{app} and $\Delta theta$ accurately. While the details of the morphology of the images is the same for all models, the evolution of the centroid is determined by growth of the emitting region, which in turn is related to how fast the shock can expand. For example, model 1 (5) encounters the least (the most) resistance

from the surrounding medium as the density is the lowest (highest) in the set. Visual inspection shows that model 1 (5) results in excess (too little) centroid displacement to be compatible with observations. Models $2,\ 3$ and 4 provides a centroid displacement in agreement within error with the observational value. More fine analysis would lead to tighter constraints on θ_{obs} independently of any other approximations or assumptions on the properties of the system except those made to calculate the model (e.g. without the point particle approximation on the centroid motion). As the degeneracy is generated by sets of appropriately scaled parameters, determination of θ_{obs} automatically puts constraints on the full set $\{\theta_c,\ \theta_{obs},\ n,\ \epsilon_b\}$, given a set of fixed parameters like that in table 8.3.

The two methods described above make it possible to break the degeneracy in the light curves using two radio images. Figure 8.14 shows the centroid evolution for each of the five models. The $\tilde{x}_c - T$ curves do not overlap as long as the centroid does not move backwards. Given a well localized explosion locus, in principle a single radio image and the corresponding centroid position can provide enough information to distinguish the model parameters $\{\theta_c,\ \theta_{obs},\ n,\ \epsilon_b\}$ which best agree with observations. In all cases the curves behave as broken power-laws $x_c \propto T^{\alpha}$. It is found that $\alpha \approx 0.85$ provides a good fit until the light curve peak time $T \sim 150$ days (dashed lines in the figure), and to a lesser degree $\alpha \approx 0.4$ from thereon until $T \sim 2000$ days (not shown in the figure).

If the images are obtained around or after the time of the peak centroid displacement it is possible that one of the images may correspond to a time when the centroid has reversed its motion. This could in principle affect the parameters estimated from images. Hence three images could be needed to ensure that the correct phase of the centroid displacement (that is, forward or reverse) is identified. In the case of GW170817 the third image presented by Ghirlanda et al. (2019), obtained at 207 days post-merger confirms that the centroid has not reversed its motion.

For the GW170817-like models discussed in this section we find from figure 8.14 that the centroid continues to move away from the explosion locus until long after the light curve peak time T_p. This also holds for the models considered in section 8.2.1. It can be expected that in similar situations the centroid forward motion will continue until

	Δx_c (mas)	β_{app}	$\Delta\theta$ (rad)	% error
Model 1	3.7	5.6	0.22	4%
Model 2	3.1	4.7	0.27	4%
Model 3	2.6	4.0	0.32	3%
Model 4	2.3	3.5	0.37	0.5%
Model 5	2.0	3.1	0.41	2%

Table 8.4: Observable parameters extracted from the synthetic radio images shown in 8.13.

long after T_p. As the centroid displacement is most interesting for parameter estimation when obtained around peak time, information from two images should be sufficient, in most cases, to break light curve model degeneracies.

8.4 Discussion and conclusions

GRB jets have been studied extensively in the literature with varying degrees of detail. Semi-analytic models have been particularly successful in modelling light curves of GRB afterglows. This type of model often assumes a non-spreading jet, with fixed opening-angle and purely radial expansion. However, different physical or analytic arguments, later confirmed by hydrodynamics simulations, suggest that the opening angle of the jet should also grow. In particular, it is expected that this feature should become especially relevant around the light curve peak time, when the jet has decelerated significantly.

VLBI radio images have recently proven to be important tools to determine whether a successful, narrow jet was launched after the neutron star merger GW170817, or whether some form of wide-angle outflow was responsible for the afterglow. In addition, radio images have be proposed as a complementary observable to afterglow light curves which can break degeneracies in afterglow models.

In this chapter the properties of synthetic images of both non-spreading and laterally spreading jets are studied. The images were calculated using a semi-analytic code built on the dynamics described in Pe'er (2012) and the lateral spreading description from Granot & Piran (2012).

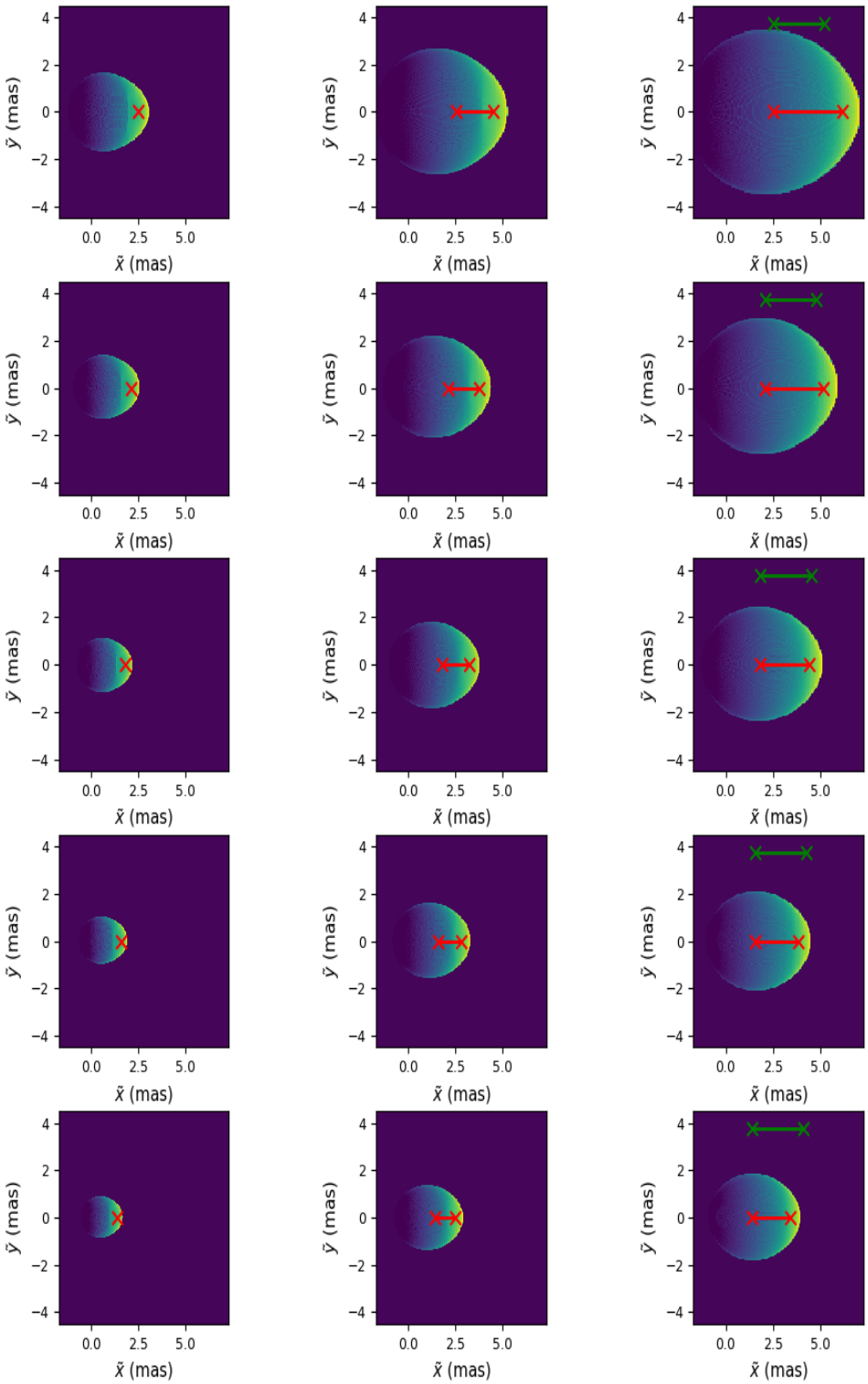

Figure 8.13: Synthetic radio images corresponding to the degenerate light curves in figure 8.12. The rows correspond to models $1-5$ respectively. The left, central and right columns correspond to times $T = 75,\ 150$ and 230 days. The centroid positions are shown with red crosses, and the centroid displacement with respect to $T = 75$ days are shown with red lines. The centroid displacement reported in Mooley et al. (2018) is shown with green lines.

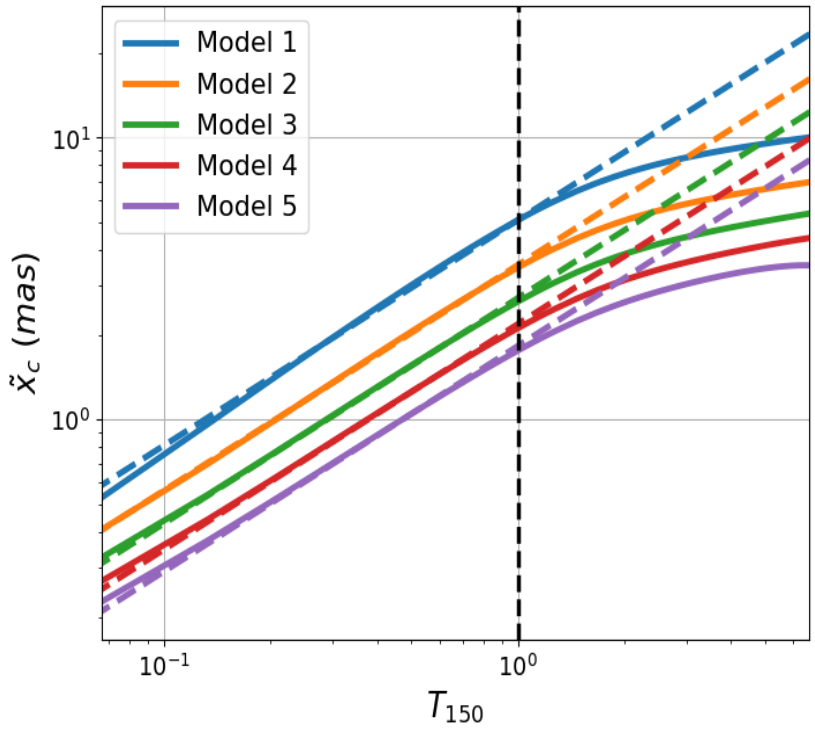

Figure 8.14: Centroids of the images for models $1-5$. The dashed lines are for power-law fits $\tilde{x}_c \propto t^{0.86}$. The color scheme is the same as in figure 8.13.

The most robust quantity which can be obtained from images is the brightness-weighted image centroid. The time evolution of this quantity is characterized in detail. It is found that it initially moves away from the explosion locus reaching a maximum displacement, and then is reversed. This effect happens much earlier in the case of laterally spreading jets than non-spreading jets due to the faster deceleration of the shock. The broad details of the centroid evolution are found to be consistent with that of other semi-analytic (Gill & Granot, 2018) and hydrodynamic simulations (e.g. Zrake et al. 2018; Granot & Piran 2012). The centroid apparent velocity, β_{app}, is also obtained. Simple analytic estimates show that point emitters moving at relativistic velocities can present apparent superluminal velocities in the sky. This is also found for the centroid of radio images. It is found that the β_{app} decreases below 1 much sooner for laterally spreading jets than for non-spreading jets. The centroid reverse motion is found to be subluminal. Other potential observables are characterized, such as the FWHM of the image and the lateral brightness distributions. However, these quantities will depend on the details of the image structure and may be difficult to

obtain except for extremely bright, close or favourably inclined events.

The detectability of the centroid displacement is mainly limited by two factors: the detection threshold of the radio flux and the uncertainty on the centroid position. An upper-bound on the distance at which the centroid displacement can be detected can be found by determining the limiting distance for these two factors and taking the smallest of them. For the models in this chapter the distance between the source and the observer was fixed to $D = 41.3$ Mpc. The centroid displacement at two luminosity distances $D,\ D'$, with corresponding redshifts $z,\ z'$ are related by

$$\begin{aligned} \Delta x_c(D') &= \Delta x_c(D)\frac{D}{D'}\left[\frac{1+z'}{1+z}\right]^2 \\ &\approx \Delta x_c(41.3\text{Mpc})\left(\frac{D'}{41.3\text{Mpc}}\right)^{-1}(1+z')^2, \end{aligned} \tag{8.11}$$

where in the second line we have assumed the distance to GW170817 and taken $z \approx 0$. Setting the minimum detectable centroid displacement to the uncertainty in the VLBI measurements reported in Mooley et al. (2018) then the maximum distance at which the displacement could be detected, given a large enough radio flux, is $D_{\text{max},x_c} \approx 370$ Mpc (for this estimate the approximation $z \approx H_0 D/c$, valid at small redshifts, was assumed for simplicity). The peak radio flux was estimated in Makhathini & et. al (2020) to be $F_{3GHz} \approx 100\mu Jy$, with a reported late-time flux of $4.9\mu Jy$ at $T = 767$ days. Taking this last data point as the detection threshold, the maximum distance at which the peak would be detectable is given by $D_{\text{max},F_\nu} \approx \sqrt{100/4.9} \times 41.3\text{Mpc} \approx 190 Mpc$. As $D_{\text{max},F_\nu} < D_{\text{max},x_c}$, the detection of centroid displacement is flux-limited in distance.

Gravitational waves from compact binary mergers provide a luminosity distance D which is independent of the cosmological distance ladder (Schutz, 1986; Holz & Hughes, 2005). Therefore, well localized GW signals can be used to estimate Hubble's constant H_0. However, this kind of measurement is subject to several uncertainties. Firstly, impossible to determine the redshift z of the event with GWs alone. Equal GW strains at different z can obtained by rescaling the binary member masses. The localization uncertainty of GWs makes it hard to pinpoint the host galaxy of the merger and

indirectly obtain the redshift of the event. In addition the distance D and inclination with respect to the binary plane θ_{obs} are entangled in the GW strain as $h_\times \propto \cos\theta_{obs}/D$ and $h_+ \propto (1+\cos^2\theta_{obs})/D$ for the $\times$ and $+$ polarization states respectively (Misner et al., 1973; Holz & Hughes, 2005). Without accurate polarization measurements to obtain θ_{obs}, which would require at least three interferometers on different baselines (Hayama & Nishizawa, 2013), this degeneracy leads to additional uncertainties in D. Notwithstanding, the GW signal was sufficient to obtain a constraint on the Hubble constant of $H_0 = 70^{+12}_{-8}$km s^{-1}Mpc^{-1} (Abbott et al., 2017c).

These problems can be partially solved if an accompanying EM counterpart is observed, such as in the case of GW170817. The EM counterpart localizes the host galaxy and provides a redshift estimate. In addition, observation of the long-lasting components of the counterpart such as an afterglow provide an avenue to obtain the θ_{obs}. However, as was discussed above, degeneracies in the light curves themselves can make it difficult to disentangle θ_{obs}. The combination of GW and EM information resulted in $H_0 = 74^{+12}_{-8}$km s^{-1}Mpc^{-1} (Guidorzi et al., 2017).

As was illustrated in the previous section, including centroid displacement measurements from images breaks this degeneracy. The combination of GWs, light curves and images should provide the best parameter estimation. Imaging data was used in Mooley et al. (2018) to constrain θ_{obs}. This was subsequently used in Hotokezaka et al. (2019) to constrain the Hubble constant to $H_0 = 68.9^{+4.7}_{-4.6}$km s^{-1}Mpc^{-1}. It must be noted that the theoretical models used in this work were limited to non-spreading models.

The inclination θ_{obs} was constrained in (Mooley et al., 2018) by using the point particle approximation as $\theta_{obs} \approx 1/\beta_{app}$. The results in this chapter suggest that this approximation can be inappropriate for inclined, laterally spreading jets under certain conditions. While this approximation provided good estimates for θ_{obs} in the case of the jets considered in 8.3, for the jets in 8.2 large discrepancies were found, of up to 25% for $\alpha = 45°$.

The θ_{obs} estimates for the light-curve degenerate models in 8.3 al return discrepancies of similar order, in the range $2-4$ % (except in the case of model 4, for which the

discrepancy was 0.5%). These models were obtained by means of analytic scalings for which θ_{obs}/θ_c is constant. In contrast, among other differences, in 8.2 this ratio changes, as θ_c is kept constant while θ_{obs} varies. This raises the question of the relationship between θ_{obs}/θ_c and how well θ_{obs} can be estimated. An additional source of uncertainty can be the observing window. In other words, if the apparent velocity is estimated as $\Delta x_c/\Delta T$, where $\Delta T = T_2 - T_1$ and $T_{1,2}$ are two times before and after T_p, how does the choice of these times affect the estimate of θ_{obs}?

While an in-depth analysis is out of the scope of this work, these points are illustrated in figure 8.15. In this plot the percentage discrepancy between the true value of θ_{obs} and that inferred from synthetic images is shown for model 3 in table 8.3. Note that θ_c is constant. Two different observing windows around the light curve peak T_p are considered: $T_1 = 0.5T_p,\ T_2 = 1.5T_p$, and $T_1 = 0.75T_p,\ T_2 = 1.25T_p$. For both windows the discrepancy increases θ_{obs}, reaching its maximum value at $\theta_{obs}/\theta_c \approx 11.5$, and then decreases. It can also be seen in this figure that the estimate is sensitive to the times around the peak used to obtain β_{app}. However, the results indicate that the extra error incurred by changing the observing window is around an order of magnitude smaller than that due to the point particle approximation. The relationship between θ_{obs} and β_{app} in the context of afterglow parameter estimation will be explored further in future work.

Even if the point-particle approximation cannot provide accurate estimates of θ_{obs}, the centroid motion can still provides an avenue for breaking degeneracies in the set $\Phi = \{\theta_c,\ \theta_{obs},\ n,\ \epsilon_B\}$. With all other parameters fixed by light curves, it is found that the centroid displacement or equivalently β_{app} uniquely determine the parameter Φ for the system by direct comparison (this was illustrated in 8.13). From a computational perspective, obtaining a synthetic image is equivalent to calculating a single time-point of a light curve. Therefore, including imaging information in parameter fitting routines should, in principle, introduce little extra computational overhead.

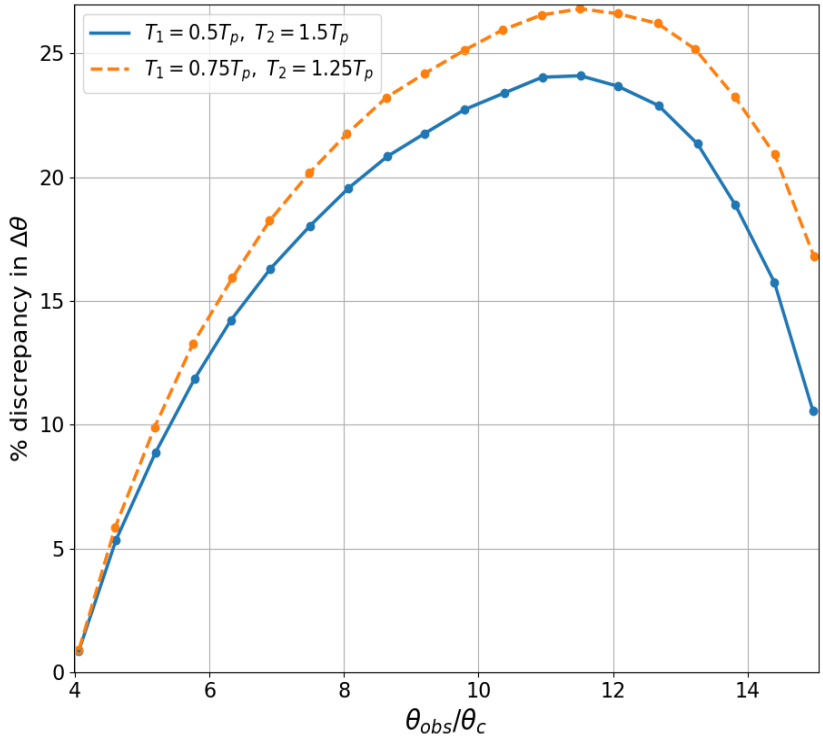

Figure 8.15: Error in the estimation of $\Delta\theta$ from synthetic images as a function of θ_{obs}/θ_c for two different observing windows.

Chapter 9

Conclusions and future work

9.1 Conclusions

The aim of this thesis was to contribute to two important aspects of gravitational wave astronomy: the pre-merger physics of compact stellar binaries and the post-merger physics, in particular the electromagnetic counterpart of NS mergers.

In part I we propose and study a new formation channel of compact binary mergers: the tidal encounter of binaries with a massive BH. Hypervelocity stars indicate that stellar binaries can undergo tidal encounters with galactic centre massive black holes. In these encounters the binary can be disrupted, with one of its components launched away from the nuclear star cluster at a speed larger than the galactic escape velocity, while the other component is captured by the MBH.

However, binary disruption is not the only possible outcome. Sari et al. (2010) and Brown et al. (2018) showed that, under very general conditions, binaries can survive the encounter even for deep penetrations into the tidal sphere of the MBH. Although the HVSs described so far are main-sequence stars, the same mechanism is applicable to BH-BH, BH-NS and NS-NS binaries. The survivors are generally deformed by the tidal encounter, which can hasten their merger due to GW radiation. With this in mind, the properties of the tidal encounter survivors were characterized in detail in chapters

4 and 5.

The merger rate density obtained for initially circular binaries to be $\mathcal{R} \approx 0.6\,\mathrm{Gpc}^{-3}\mathrm{yr}^{-1}$, by using a Drake equation-like approach. The dominating source of uncertainty in this estimate is that of the binary tidal encounter rate inferred from hypervelocity star observations. The obtained $\mathcal{R}$ due to the is ~ 50 times smaller than the current upper-bound on the total merger rate inferred from LIGO/VIRGO Observations (Abbott et al., 2020b). While this will certainly not be the dominating process leading to BH mergers, in upcoming years the order of one to several detected mergers may be due to the tidal encounter channel.

By considering different initial spin set-ups (BH spins aligned with the binary angular momentum, and uniformly or normal distributed BH spin orientations in a cone of opening angle $\pi/4$ around the binary angular momentum), it was found that $\sim 19\%$ ($\sim 39\%$) of binaries with merger times reduced by a factor of $> 10^2$ ($> 10^5$) emerge with $\chi_{\rm eff} < 0$ (in the latter case the distribution is rather flat, with a peak at $\chi_{eff} \approx 1$).

The analysis was subsequently extended to populations of initially eccentric binaries, considering three eccentricity distributions compatible with different stellar populations. When considering survivors with merger times less than the age of the Universe (and hence of interest in the context of GW detections) it was found that their statistical properties were broadly identical in all three cases. The survivor effective spin distributions were also found to not be significantly modified by considering eccentric binaries, and any change in the merger rate density compared to the initially circular case was also found to be unimportant when compared to the other sources of uncertainty.

In part II the focus was shifted to the post-merger physics, in particular to modelling radio images of GRB afterglows. GW170817 confirmed that sGRBs and their afterglows can follow from neutron star mergers (Abbott et al., 2017c,e). In the case of this event, radio imaging provided key insight to determine the jet-like nature of the emission source (Mooley et al., 2018; Ghirlanda et al., 2019).

A systematic study of synthetic radio images of afterglows was presented. The images of collimated and laterally spreading jets were obtained using a semi-analytic code.

While these methods have been used previously to obtain lightcurves of laterally spreading jets, to the knowledge of the author this is the first time semi-analytic calculations have been used to obtain images of these systems.

The analysis was limited to Gaussian structured jets. However the method and code used can be generalized to include different structures, such as power-law or two-component jets (Lamb & Kobayashi, 2017). Quantities of interest, such as the brightness-weighted centroid or the FWHM of the images were obtained. For a jet with typical parameters, the time evolution of the centroid and its apparent velocity were characterized. The image centroid was found to initially move away from the explosion locus at superluminal speeds. Eventually, it reaches a maximum displacement and turns back. For late enough observing times, when the principal-jet has decelerated significantly and the counter-jet dominates the motion, the centroid can move to the opposite side of the explosion origin. This behavior was associated with the evolution of the principal and counter jets. The results found qualitatively agree with hydrodynamic simulations in the literature, showing the same features.

The discussion then moved onto an application of radio imaging: breaking degeneracies in parameter estimation from lightcurves, and in particular determining the viewing angle θ_{obs}. The key result of this section is shown in figures 8.12 and 8.13. In these figures the lightcurves (in rough agreement with 3 GHz VLA data for neutron star merger event afterglow) and corresponding radio images at different times are shown for five jets with differing parameters (ranging for example two orders of magnitude in ambient density and viewing angles between 13° and 24°). While the lightcurves are identical during the rise and around the peak time, their images present different apparent sizes, centroid displacements and hence apparent centroid velocities. Using these images it is explicitly shown how the comparison of two or more radio images can break the degeneracy in lightcurves. With this approach, the viewing angle of the GW170817 afterglow-like light curves is found to be $\sim 18^\circ$.

9.2 Future Work

In chapters 4 and 5 the discussion is limited to the properties of the surviving binaries. However, from the point of view of GWs there are two more systems to consider. First, the survivor plus MBH system. While the restricted parabolic formalism remains valid to describe the trajectory of the survivors, it is possible than enough energy can be exchanged between the system degrees of freedom for the survivor to become bound on a closed orbit to the MBH. For example, if the binary is stretched by the tidal encounter the necessary energy must be removed from the COM orbital energy, which can slightly modify the orbit. Second, in the case of disrupted binaries one of the binary components again also bound to the MBH. Either of these situations could constitute a source of extreme mass ratio inspirals (EMRIs, Berry & Gair 2012), prime GW sources for the future space-based GW interferometer LISA (Babak et al., 2017). A more detailed investigation of the dynamics of these systems is required to determine if they are viable EMRI sources and the event rate which can be expected from them.

As the treatment of the problem was classical, the BH spins were considered constant throughout the dynamical evolution. Nonetheless, for narrow enough binaries relativistic effects can become relevant and the BH spins and binary angular momentum can couple. While a full general relativistic treatment of the problem would be complex, post-Newtonian terms can be included in the dynamics which account for these extra couplings (Blanchet, 2014). This can be used to quantify relativistic effects on the expected $\chi_{\rm eff}$ or eccentricity distributions.

It is expected that extended GW network made up of the aLIGO, aVirgo and Kagra detectors will be sensitive to eccentricities as small as $e \sim 10^{-3}$ (Gondán et al., 2018). As some of the binaries emerge from the tidal encounter with large eccentricities, they may not fully circularize before passing different detector bands. Peter's equations 2.11 can be used to obtain the evolution of the binaries in the $a - e$ plane and the corresponding GW strain due to the binary inspiral (Peters, 1964). This can be used to constrain the detectability of the binaries in different frequency bands, and whether they have enough residual eccentricity to distinguish them from circular inspirals.

The image study presented in chapter 8 can be extended to consider different jet structures. In the case of angular structures in which an energetic core dominates the energy distribution the general, qualitative properties of the images are not expected to change drastically. However, images of jets with radial structure, such as refreshed shocks (e.g. Lamb et al. 2020) could lead to significant qualitative and quantitative changes in the behavior of the images. In addition, with the code used in this work other lateral expansion laws can be tested, as long as they can be encoded in the form $d\theta/dR = f(R, \Gamma, \theta)$, where f is some function of the jet parameters (e.g. the $a = 0$ case from Granot & Piran 2012).

In chapter 8 the point-emitter approximation for obtaining the viewing angle from the superluminal motion is shown to present varying degrees of accuracy, depending on the ratio θ_{obs}/θ_c. Understanding the origin of this dependence is important for the estimation of θ_{obs}, and could potentially be used to inform fitting routines for the range of possible θ_{obs} explored.

Light curves, superluminal motion and gravitational wave data have already been combined to obtain an estimate of the Hubble Constant H_0 (e.g. Hotokezaka et al. 2019). However, the semi-analytic models used in these works and others did not consider lateral spreading in their calculations. This can lead to an underestimate of the ratio of the jet energy to the ambient density or of the viewing angle (as the laterally spreading jet lightcurve peaks earlier than that of a collimated jet with the same energy). This in turn can introduce uncertainties in the Hubble constant estimate. The semi-analytic formalism used here allows for the dynamics of laterally spreading jets to be obtained without the need for costly hydrodynamics simulations. Therefore, the method used in this thesis can be used to obtain constraints on H_0 with the additional dynamical feature of lateral spreading.

Bibliography

Abbott B., Abbott R., Abbott T., Abernathy M., Acernese F., Ackley K., Adams C., Adams T., Addesso P., Adhikari R., et al. 2016, Physical Review X, 6

Abbott B., Abbott R., Abbott T., Acernese F., Ackley K., Adams C., Adams T., Addesso P., Adhikari R., Adya V., et al. 2017b, Physical Review Letters, 118

Abbott B., Abbott R., Abbott T., Acernese F., Ackley K., Adams C., Adams T., Addesso P., Adhikari R., Adya V., et al. 2017a, Physical Review Letters, 119

Abbott B., Abbott R., Abbott T., Acernese F., Ackley K., Adams C., Adams T., Addesso P., Adhikari R., Adya V., et al. 2017c, Physical Review Letters, 119

Abbott B., et al., 2016a, Phys. Rev. Lett., 116, 061102

Abbott B., et al., 2019, Astrophys. J. Lett., 882, L24

Abbott B. P., Abbott R., Abbott T. D., Abraham S., Acernese F., Ackley K., Adams C., Adhikari R. X., Adya V. B., Affeldt C., et al. 2019, The Astrophysical Journal, 883, 149

Abbott B. P., Abbott R., Abbott T. D., Abraham S., Acernese F., Ackley K., Adams C., Adya V. B., Affeldt C., et al. 2020, Living Reviews in Relativity, 23

Abbott B. P., Abbott R., Abbott T. D., Acernese F., Ackley K., Adams C., Adams T., Addesso P., Adhikari R. X., Adya V. B., et al. 2017d, The Astrophysical Journal, 851, L35

Abbott B. P., Abbott R., Abbott T. D., Acernese F., Ackley K., Adams C., Adams T., Addesso P., Adhikari R. X., Adya V. B., et al. 2017e, The Astrophysical Journal, 848, L12

Abbott B. P., Abbott R., Adhikari R., Ajith P., Allen B., Allen G., Amin R. S., Anderson S. B., Anderson W. G., Arain M. A., et al. 2009, Reports on Progress in Physics, 72, 076901

Abbott B. P., et al., 2016b, Phys. Rev. Lett., 116, 241103

Abbott R., et al., 2020a, Phys. Rev. Lett., 125, 101102

Abbott R., et al., 2020b, arXiv e-prints, p. arXiv:2010.14527

Adams F. C., Shu F. H., 1985, ApJ, 296, 655

Addison E., Gracia-Linares M., Laguna P., Larson S. L., 2019, General Relativity and Gravitation, 51, 38

Akiyama K., et al., 2019, Astrophys. J., 875, L1

Alexander T., 2017, ARA&A, 55, 17

Antonini F., Rasio F. A., 2016, ApJ, 831, 187

Arca-Sedda M., Capuzzo-Dolcetta R., 2019, MNRAS, 483, 152

Arca-Sedda M., Gualandris A., 2018, MNRAS, 477, 4423

Arca-Sedda M., Li G., Kocsis B., 2018, arXiv e-prints, p. arXiv:1805.06458

Ascenzi S., Oganesyan G., Branchesi M., Ciolfi R., 2021, Journal of Plasma Physics, 87, 845870102

Aso Y., Michimura Y., Somiya K., Ando M., Miyakawa O., Sekiguchi T., Tatsumi D., Yamamoto H., 2013, Phys. Rev. D, 88, 043007

Bañados E., Venemans B. P., Mazzucchelli C., Farina E. P., Walter F., Wang F., Decarli R., Stern D., Fan X., Davies F. B., Hennawi J. F., Simcoe R. A., Turner M. L., Rix H.-W., Yang J., Kelson D. D., Rudie G. C., Winters J. M., 2018, Nature, 553, 473

Babak S., Gair J., Sesana A., Barausse E., Sopuerta C. F., Berry C. P. L., Berti E., Amaro-Seoane P., Petiteau A., Klein A., 2017, Phys. Rev. D, 95, 103012

Barrett J. W., Gaebel S. M., Neijssel C. J., Vigna-Gómez A., Stevenson S., Berry C. P. L., Farr W. M., Mandel I., 2018, MNRAS, 477, 4685

Barthelmy S. D., Barbier L. M., Cummings J. R., Fenimore E. E., Gehrels N., Hullinger D., Krimm H. A., Markwardt C. B., Palmer D. M., Parsons A., et al. 2005, Space Science Reviews, 120, 143–164

Bate R. R., Mueller D. D., White J. E., 1971, Fundamentals of Astrodynamics. Dover Publications, New York

Belczynski K., Holz D. E., Bulik T., O'Shaughnessy R., 2016, Nature, 534, 512

Belczynski K., Klencki J., Fields C. E., Olejak A., Berti E., Meynet G., Fryer C. L., Holz D. E., O'Shaughnessy R., Brown D. A., et al. 2020, Astronomy Astrophysics, 636, A104

Beniamini P., Granot J., Gill R., 2020, Monthly Notices of the Royal Astronomical Society, 493, 3521–3534

Berger E., 2014, ARA&A, 52, 43

Berger E., Fong W., Chornock R., 2013, The Astrophysical Journal, 774, L23

Berry C. P. L., Gair J. R., 2012, Monthly Notices of the Royal Astronomical Society, 429, 589

Berry C. P. L., Gair J. R., 2013, MNRAS, 435, 3521

Blair D. G., Howell E. J., Ju L., Zhao C., 2012, Advanced Gravitational Wave Detectors

Blanchet L., 2014, Living Reviews in Relativity, 17, 2

Blandford R. D., McKee C. F., 1976, Physics of Fluids, 19, 1130

Blandford R. D., Znajek R. L., 1977, MNRAS, 179, 433

Bradnick B., Mandel I., Levin Y., 2017, MNRAS, 469, 2042

Branchesi M., 2016, Journal of Physics: Conference Series, 718, 022004

Bromley B. C., Kenyon S. J., Geller M. J., Brown W. R., 2012, The Astrophysical Journal Letters, 749, L42

Brown H., Kobayashi S., Rossi E. M., Sari R., 2018, MNRAS, in press

Brown W. R., 2008, arXiv e-prints, p. arXiv:0811.0571

Brown W. R., 2015, Annual Review of Astronomy and Astrophysics, 53, 15

Burbidge E. M., Burbidge G. R., Fowler W. A., Hoyle F., 1957, Rev. Mod. Phys., 29, 547

Burrows D. N., Hill J. E., Nousek J. A., Kennea J. A., Wells A., Osborne J. P., Abbey A. F., Beardmore A., Mukerjee K., Short A. D. T., et al. 2005, Space Science Reviews, 120, 165–195

Cenko S. B., Kulkarni S. R., Horesh A., Corsi A., Fox D. B., Carpenter J., Frail D. A., Nugent P. E., Perley D. A., Gruber D., et al. 2013, The Astrophysical Journal, 769, 130

Chen X., Han W.-B., 2018, Communications Physics, 1, 53

Cohen M. H., 1973, Proceedings of the IEEE, 61, 1192

Colpi M., Sesana A., 2017, Gravitational Wave Sources in the Era of Multi-Band Gravitational Wave Astronomy. World Scientific Publishing Co, pp 43–140

Conselice C. J., Blackburne J. A., Papovich C., 2005, ApJ, 620, 564

Conselice C. J., Wilkinson A., Duncan K., Mortlock A., 2016, ApJ, 830, 83

Cowperthwaite P. S., Berger E., Villar V. A., Metzger B. D., Nicholl M., Chornock R., Blanchard P. K., Fong W., Margutti R., Soares-Santos M., et al. 2017, The Astrophysical Journal, 848, L17

Daigne F., Mochkovitch R., 1998, MNRAS, 296, 275

De Colle F., Ramirez-Ruiz E., Granot J., Lopez-Camara D., 2012, The Astrophysical Journal, 751, 57

Dunham M. M., Stutz A. M., Allen L. E., Evans II N. J., Fischer W. J., Megeath S. T., Myers P. C., Offner S. S. R., Poteet C. A., Tobin J. J., et al. 2014, Protostars and Planets VI

Eggleton P., 2006, Evolutionary Processes in Binary and Multiple Stars

Einstein A., 1905, Annalen Phys., 17, 891

Einstein A., 1916, Sitzungsberichte der Königlich Preußischen Akademie der Wissenschaften (Berlin, pp 688–696

Farr B., Holz D. E., Farr W. M., 2018, ApJL, 854, L9

Farr W. M., Stevenson S., Miller M. C., Mandel I., Farr B., Vecchio A., 2017, Nature, 548, 426

Fernández J. J., Kobayashi S., 2019, Monthly Notices of the Royal Astronomical Society, 487, 1200–1209

Fernández J. J., Kobayashi S., Lamb G. P., 2021

Fernández R., Metzger B. D., 2016, Annual Review of Nuclear and Particle Science, 66, 23–45

Flanagan É. É., Hughes S. A., 2005, New Journal of Physics, 7, 204

Fong W., Berger E., Margutti R., Zauderer B. A., Troja E., Czekala I., Chornock R., Gehrels N., Sakamoto T., Fox D. B., et al. 2012, The Astrophysical Journal, 756, 189

Fong W., Berger E., Metzger B. D., Margutti R., Chornock R., Migliori G., Foley R. J., Zauderer B. A., Lunnan R., Laskar T., et al. 2013, The Astrophysical Journal, 780, 118

Fong W., Blanchard P. K., Alexander K. D., Strader J., Margutti R., Hajela A., Villar V. A., Wu Y., Ye C. S., Berger E., et al. 2019, The Astrophysical Journal, 883, L1

Garcia-Bellido J., Siles J. F. N., Morales E. R., , 2020, Bayesian analysis of the spin distribution of LIGO/Virgo black holes

Gayathri V., Healy J., Lange J., O'Brien B., Szczepanczyk M., Bartos I., Campanelli M., Klimenko S., Lousto C., O'Shaughnessy R., 2020

Gebhardt K., Bender R., Bower G., Dressler A., Faber S. M., Filippenko A. V., Green R., Grillmair C., Ho L. C., Kormendy J., Lauer T. R., Magorrian J., Pinkney J., Richstone D., Tremaine S., 2000, The Astrophysical Journal Letters, 539, L13

Gehrels N., et al. 2004, ApJ, 611, 1005

George D., Huerta E. A., 2018, Physics Letters B, 778, 64

Georgescu I., 2020, Nature Reviews Physics, 2, 222

Gerosa D., 2018, Journal of Physics: Conference Series, 957, 012014

Gerosa D., Berti E., 2017, Phys. Rev. D, 95, 124046

Ghirlanda G., Salafia O. S., Paragi Z., Giroletti M., Yang J., Marcote B., Blanchard J., Agudo I., An T., Bernardini M. G., et al. 2019, Science, 363, 968–971

Gill R., Granot J., 2018, Monthly Notices of the Royal Astronomical Society, 478, 4128–4141

Gondán L., Kocsis B., Raffai P., Frei Z., 2018, Astrophys. J., 860, 5

Gondán L., Kocsis B., Raffai P., Frei Z., 2018, The Astrophysical Journal, 855, 34

Gottlieb O., Nakar E., Bromberg O., 2020, Monthly Notices of the Royal Astronomical Society

Gottlieb O., Nakar E., Piran T., Hotokezaka K., 2018, Mon. Not. Roy. Astron. Soc., 479, 588

Granot J., 2007, in Revista Mexicana de Astronomia y Astrofisica, vol. 27 Vol. 27 of Revista Mexicana de Astronomia y Astrofisica Conference Series, The Structure and Dynamics of GRB Jets. pp 140–165

Granot J., De Colle F., Ramirez-Ruiz E., 2018, MNRAS, 481, 2711

Granot J., Kumar P., 2003, The Astrophysical Journal, 591, 1086–1096

Granot J., Panaitescu A., Kumar P., Woosley S. E., 2002, The Astrophysical Journal, 570, L61–L64

Granot J., Piran T., 2012, MNRAS, 421, 570

Grishin E., Perets H. B., Zenati Y., Michaely E., 2017, MNRAS, 466, 276

Guidorzi C., Margutti R., Brout D., Scolnic D., Fong W., Alexander K. D., Cowperthwaite P. S., Annis J., Berger E., Blanchard P. K., et al. 2017, The Astrophysical Journal, 851, L36

Hailey C., Mori K., Bauer F., Berkowitz M., Hong J., Hord B., 2018, Nature, 556, 70

Hallinan G., Corsi A., Mooley K. P., Hotokezaka K., Nakar E., Kasliwal M. M., Kaplan D. L., Frail D. A., Myers S. T., Murphy T., et al. 2017, Science, 358, 1579–1583

Haugan M. P., Lämmerzahl C., 2001, Lect. Notes Phys., 562, 195

Hayama K., Nishizawa A., 2013, Physical Review D, 87

Hild S., Chelkowski S., Freise A., 2008, arXiv e-prints, p. arXiv:0810.0604

Hills J. G., 1988, Nature, 331, 687

Hoang B.-M., Naoz S., Kocsis B., Rasio F. A., Dosopoulou F., 2018, ApJ, 856, 140

Holz D. E., Hughes S. A., 2005, The Astrophysical Journal, 629, 15–22

Hotokezaka K., Nakar E., Gottlieb O., Nissanke S., Masuda K., Hallinan G., Mooley K. P., Deller A., 2019, Nature Astron., 3, 940

Hotokezaka K., Piran T., 2017, arXiv e-prints, p. arXiv:1707.08978

Hotokezaka K., Piran T., 2017a, ApJ, 842, 111

Hotokezaka K., Piran T., 2017b, ApJL, 842, 111

Huang Y. F., Dai Z. G., Lu T., 2002, Monthly Notices of the Royal Astronomical Society, 332, 735–740

Huerta E. A., Brown D. A., 2013, Phys. Rev. D, 87, 127501

Jeans J. H., 1919, MNRAS, 79, 408

Jennison R. C., 1958, MNRAS, 118, 276

Kasliwal M. M., Nakar E., Singer L. P., Kaplan D. L., Cook D. O., Van Sistine A., Lau R. M., Fremling C., Gottlieb O., Jencson J. E., et al. 2017, Science, 358, 1559–1565

Kimball C., Talbot C., Berry C. P. L., Zevin M., Thrane E., Kalogera V., Buscicchio R., Carney M., Dent T., Middleton H., Payne E., Veitch J., Williams D., 2020, arXiv e-prints, p. arXiv:2011.05332

Kızıltan B., Baumgardt H., Loeb A., 2017, Nature, 542, 203

Kobayashi S., 2000, ApJ, 545, 807

Kobayashi S., 2017, Galaxies, 5, 80

Kobayashi S., 2019, Magnetic Fields in Gamma-Ray Bursts and Their Polarised Emission. p. 337

Kobayashi S., Hainick Y., Sari R., Rossi E. M., 2012, ApJ, 748, 105

Kobayashi S., Laguna P., Phinney E. S., Meszaros P., 2004, The Astrophysical Journal, 615, 855–865

Kobayashi S., Piran T., Sari R., 1997, The Astrophysical Journal, 490, 92–98

Kobayashi S., Piran T., Sari R., 1999, ApJ, 513, 669

Kocsis B., 2013, ApJ, 763, 122

Komossa S., 2015, Journal of High Energy Astrophysics, 7, 148

Kowalska I., Bulik T., Belczynski K., Dominik M., Gondek-Rosinska D., 2011, A&A, 527, A70

Kumar P., Granot J., 2003a, ApJ, 591, 1075

Kumar P., Granot J., 2003b, ApJ, 591, 1075

Kumar P., Zhang B., 2015, Physics Reports, 561, 1–109

Lamb G. P., Kobayashi S., 2017, MNRAS, 472, 4953

Lamb G. P., Kobayashi S., 2019, MNRAS, 489, 1820

Lamb G. P., Levan A. J., Tanvir N. R., 2020, Astrophys. J., 899, 105

Lamb G. P., Lyman J. D., Levan A. J., Tanvir N. R., Kangas T., Fruchter A. S., Gompertz B., Hjorth J., Mandel I., Oates S. R., et al. 2019, The Astrophysical Journal, 870, L15

Lamb G. P., Mandel I., Resmi L., 2018, Monthly Notices of the Royal Astronomical Society, 481, 2581–2589

Lamb G. P., Tanvir N. R., Levan A. J., Postigo A. d. U., Kawaguchi K., Corsi A., Evans P. A., Gompertz B., Malesani D. B., Page K. L., et al. 2019, The Astrophysical Journal, 883, 48

Landau L. D., Lifshitz E. M., 1980, The Classical Theory of Fields, 4 edn. Course of theoretical physics, Vol. 2, Butterworth-Heinemann, Oxford

Landau L. D., Lifshitz E. M., 1987, Fluid Mechanics, Second Edition, 2 edn. Course of theoretical physics, Vol. 6, Butterworth-Heinemann, Oxford

Le Tiec A., Novak J., 2017, Theory of Gravitational Waves. World Scientific Publishing Co, pp 1–41

Lee W. H., Ramirez-Ruiz E., 2007, New Journal of Physics, 9, 17–17

Leigh N. W. C., Geller A. M., McKernan B., Ford K. E. S., Mac Low M.-M., Bellovary J., Haiman Z., Lyra W., Samsing J., O'Dowd M., Kocsis B., Endlich S., 2018, MNRAS, 474, 5672

Levan A., Crowther P., de Grijs R., Langer N., Xu D., Yoon S.-C., 2016, Space Sci. Rev., 202, 33

Levinson A., Ofek E. O., Waxman E., Gal-Yam A., 2002, The Astrophysical Journal, 576, 923–931

Licquia T., Newman J., 2013, in American Astronomical Society Meeting Abstracts #221 Vol. 221 of American Astronomical Society Meeting Abstracts, Improved Constraints on the Total Stellar Mass, Color, and Luminosity of the Milky Way. p. 254.11

Lippuner J., Roberts L. F., 2015, The Astrophysical Journal, 815, 82

Löckmann U., Baumgardt H., Kroupa P., 2010, MNRAS, 402, 519

Lu W., Beniamini P., McDowell A., 2020, arXiv e-prints, p. arXiv:2005.10313

Lyman J., et al., 2018, Nature Astron., 2, 751

Lyutikov M., 2012, MNRAS, 421, 522

Makhathini S., et. al 2020, arXiv e-prints, p. arXiv:2006.02382

Mandel I., de Mink S. E., 2016, MNRAS, 458, 2634

Mandel I., Farmer A., 2018, arXiv e-prints, p. arXiv:1806.05820

Marchant P., Langer N., Podsiadlowski P., Tauris T. M., Moriya T. J., 2016, A&A, 588, A50

Merritt D., 2013, Classical and Quantum Gravity, 30, 244005

Meszaros P., Rees M. J., 1997, The Astrophysical Journal, 476, 232–237

Metzger B. D., 2019, Living Reviews in Relativity, 23, 1

Miller M. C., Freitag M., Hamilton D. P., Lauburg V. M., 2005, ApJL, 631, L117

Miralda-Escudé J., Gould A., 2000, ApJ, 545, 847

Misner C. W., Thorne K. S., Wheeler J. A., 1973, Gravitation. W.H. Freeman, San Francisco

Molyneux S. J., Harrison C. M., Jarvis M. E., 2019, Astronomy Astrophysics, 631, A132

Mooley K. P., Deller A. T., Gottlieb O., Nakar E., Hallinan G., Bourke S., Frail D. A., Horesh A., Corsi A., Hotokezaka K., 2018, Nature, 561, 355

Moore C. J., Cole R. H., Berry C. P. L., 2015, Classical and Quantum Gravity, 32, 015014

Morris M., 1993, ApJ, 408, 496

Nakar E., Piran T., 2021, ApJ, 909, 114

Nicholl M., Berger E., Kasen D., Metzger B. D., Elias J., Briceño C., Alexander K. D., Blanchard P. K., Chornock R., Cowperthwaite P. S., et al. 2017, The Astrophysical Journal, 848, L18

O'Leary R. M., Kocsis B., Loeb A., 2009, Monthly Notices of the Royal Astronomical Society, 395, 2127

Paczynski B., 1976, in Eggleton P., Mitton S., Whelan J., eds, Structure and Evolution of Close Binary Systems Vol. 73, Common Envelope Binaries. p. 75

Panaitescu A., Kumar P., 2000, ApJ, 543, 66

Panaitescu A., Meszaros P., 1999, The Astrophysical Journal, 526, 707

Pe'er A., 2012, ApJl, 752, L8

Perera B. B. P., Stappers B. W., Lyne A. G., Bassa C. G., Cognard I., Guillemot L., Kramer M., Theureau G., Desvignes G., 2017, MNRAS, 468, 2114

Peters P. C., 1964, Phys. Rev., 136, B1224

Peters P. C., Mathews J., 1963, Physical Review, 131, 435

Petrovich C., Antonini F., 2017, ApJ, 846, 146

Pihlstrom Y. M., Taylor G. B., Granot J., Doeleman S., 2007, The Astrophysical Journal, 664, 411–415

Piran T., 2005, Reviews of Modern Physics, 76, 1143–1210

Press W. H., Teukolsky S. A., Vetterling W. T., Flannery B. P., 1992, Numerical recipes in FORTRAN. The art of scientific computing. Cambridge

Raghavan D., McAlister H. A., Henry T. J., Latham D. W., Marcy G. W., Mason B. D., Gies D. R., White R. J., ten Brummelaar T. A., 2010, The Astrophysical Journal Supplement Series, 190, 1

Rasskazov A., Kocsis B., 2019, The Astrophysical Journal, 881, 20

Rasskazov A., Kocsis B., 2019, ApJ, 881, 20

Rees M. J., 1966, Nature, 211, 468

Rhoads J. E., 1999, The Astrophysical Journal, 525, 737–749

Riles K., 2013, Progress in Particle and Nuclear Physics, 68, 1–54

Rodriguez C. L., Chatterjee S., Rasio F. A., 2016, Phys. Rev. D, 93, 084029

Rodriguez C. L., Morscher M., Pattabiraman B., Chatterjee S., Haster C.-J., Rasio F. A., 2015, Phys. Rev. Lett., 115, 051101

Roming P. W. A., Kennedy T. E., Mason K. O., Nousek J. A., Ahr L., Bingham R. E., Broos P. S., Carter M. J., Hancock B. K., Huckle H. E., et al. 2005, Space Science Reviews, 120, 95–142

Rossi E. M., Lazzati D., Salmonson J. D., Ghisellini G., 2004, Monthly Notices of the Royal Astronomical Society, 354, 86–100

Rosswog S., Ramirez-Ruiz E., Davies M. B., 2003, Monthly Notices of the Royal Astronomical Society, 345, 1077–1090

Rubbo L. J., Holley-Bockelmann K., Finn L. S., 2006, The Astrophysical Journal, 649, L25

Ryan G., Eerten H. v., Piro L., Troja E., 2020, The Astrophysical Journal, 896, 166

Rybicki G. B., Lightman A. P., 1985, Radiative Processes in Astrophysics. Wiley, New York, NY

Sabha N., Eckart A., Merritt D., Zamaninasab M., Witzel G., García-Marín M., Jalali B., Valencia-S. M., Yazici S., Buchholz R., Shahzamanian B., Rauch C., Horrobin M., Straubmeier C., 2012, A&A, 545, A70

Salafia O., Ghisellini G., Pescalli A., Ghirlanda G., Nappo F., 2015, Mon. Not. Roy. Astron. Soc., 450, 3549

Salafia O. S., Ghirlanda G., Ascenzi S., Ghisellini G., 2019, Astronomy Astrophysics, 628, A18

Sana H., de Mink S. E., de Koter A., Langer N., Evans C. J., Gieles M., Gosset E., Izzard R. G., Le Bouquin J.-B., Schneider F. R. N., 2012, Science, 337, 444

Sari R., Kobayashi S., Rossi E. M., 2010, ApJ, 708, 605

Sari R., Piran T., 1995, ApJl, 455, L143

Sari R., Piran T., 1999, The Astrophysical Journal, 520, 641–649

Sari R., Piran T., Halpern J. P., 1999, ApJl, 519, L17

Sari R., Piran T., Narayan R., 1998, ApJl, 497, L17

Schutz B. F., 1986, Nature, 323, 310

Shapiro P. R., 1979, ApJ, 233, 831

Soares-Santos M., Holz D. E., Annis J., Chornock R., Herner K., Berger E., Brout D., Chen H.-Y., Kessler R., Sako M., et al. 2017, The Astrophysical Journal, 848, L16

Taam R. E., Sandquist E. L., 2000, ARA&A, 38, 113

Tagawa H., Haiman Z., Kocsis B., 2020, Astrophys. J., 898, 25

Tai K. S., McWilliams S. T., Pretorius F., 2014, Phys. Rev. D, 90, 103001

Tanvir N. R., Levan A. J., Fruchter A. S., Hjorth J., Hounsell R. A., Wiersema K., Tunnicliffe R. L., 2013, Nature, 500, 547–549

Taylor G., 1950a, Proceedings of the Royal Society of London Series A, 201, 159

Taylor G., 1950b, Proceedings of the Royal Society of London Series A, 201, 175

Taylor G. B., Frail D. A., Berger E., Kulkarni S. R., 2004, The Astrophysical Journal, 609, L1–L4

Taylor G. B., Momjian E., Pihlstrom Y., Ghosh T., Salter C., 2005, The Astrophysical Journal, 622, 986–990

Taylor J. H., Weisberg J. M., 1982, ApJ, 253, 908

Tiwari V., Klimenko S., Christensen N., Huerta E. A., Mohapatra S. R. P., Gopakumar A., Haney M., Ajith P., McWilliams S. T., Vedovato G., Drago M., Salemi F., Prodi G. A., Lazzaro C., Tiwari S., Mitselmakher G., Da Silva F., 2016, Phys. Rev. D, 93, 043007

Troja E., Castro-Tirado A. J., González J. B., Hu Y., Ryan G. S., Cenko S. B., Ricci R., Novara G., Sánchez-Rámirez R., Acosta-Pulido J. A., et al. 2019, Monthly Notices of the Royal Astronomical Society

Troja E., Piro L., van Eerten H., Wollaeger R. T., Im M., Fox O. D., Butler N. R., Cenko S. B., Sakamoto T., Fryer C. L., et al. 2017, Nature, 551, 71–74

Troja E., Ryan G., Piro L., van Eerten H., Cenko S. B., Yoon Y., Lee S.-K., Im M., Sakamoto T., Gatkine P., et al. 2018, Nature Communications, 9

Troja E., van Eerten H., Zhang B., Ryan G., Piro L., Ricci R., O'Connor B., Wieringa M. H., Cenko S. B., Sakamoto T., 2020, Monthly Notices of the Royal Astronomical Society, 498, 5643–5651

Turner M., 1977, ApJ, 216, 610

Unnikrishnan C., 2013, International Journal of Modern Physics D, 22, 1341010

Valenti S., David J. S., Yang S., Cappellaro E., Tartaglia L., Corsi A., Jha S. W., Reichart D. E., Haislip J., Kouprianov V., 2017, The Astrophysical Journal, 848, L24

van Eerten H. J., MacFadyen A. I., 2012, ApJ, 751, 155

VanLandingham J. H., Miller M. C., Hamilton D. P., Richardson D. C., 2016, ApJ, 828, 77

Wei D. M., Jin Z. P., 2003, Astronomy Astrophysics, 400, 415–419

Weisberg J. M., Taylor J. H., Fowler L. A., 1981, Scientific American, 245, 74

Weissbein A., Sari R., 2017, MNRAS, 468, 1760

Wysocki D., Gerosa D., O'Shaughnessy R., Belczynski K., Gladysz W., Berti E., Kesden M., Holz D. E., 2018, Phys. Rev. D, 97, 043014

Xie X., Zrake J., MacFadyen A., 2018, The Astrophysical Journal, 863, 58

Yu Q., Tremaine S., 2003, ApJ, 599, 1129

Zevin M., Bavera S. S., Berry C. P. L., Kalogera V., Fragos T., Marchant P., Rodriguez C. L., Antonini F., Holz D. E., Pankow C., , 2020, One Channel to Rule Them All? Constraining the Origins of Binary Black Holes using Multiple Formation Pathways

Zhang B., Meszaros P., 2002, The Astrophysical Journal, 571, 876–879

Zhang B., Yan H., 2010, The Astrophysical Journal, 726, 90

Zhang Y., Tan J. C., Tanaka K. E. I., De Buizer J. M., Liu M., Beltrán M. T., Kratter K., Mardones D., Garay G., 2019, Nature Astronomy, 3, 517–523

Zrake J., Xie X., MacFadyen A., 2018, The Astrophysical Journal, 865, L2